# The Deep–Inelastic Structure of Diffraction

Julian Paul Phillips

March 1995

THE UNIVERSITY
of MANCHESTER

A thesis submitted to the University of Manchester for the degree of Doctor of Philosophy in the Department of Physics in the Faculty of Science.

# Contents

**1 Introduction** **11**

**2 Diffraction in DIS at HERA** **13**

2.1 Introduction . . . . . 13

2.2 Electron–Proton Interactions at HERA . . . . . 13

2.3 Kinematics of Deep–Inelastic Scattering . . . . . 14

2.4 The Structure of the Proton . . . . . 16

2.4.1 The Quark Parton Model . . . . . 16

2.4.2 QCD Evolution and the Violation of Scaling . . . . . 17

2.4.3 Measurement of the $F_2(x, Q^2)$ at HERA . . . . . 21

2.5 From Partons to Hadrons . . . . . 23

2.6 QED Radiative Corrections . . . . . 23

2.7 Diffraction . . . . . 24

2.8 Regge Theory and The Pomerančuk Pole . . . . . 25

2.9 Diffractive Deep–Inelastic Scattering . . . . . 26

2.9.1 Standard and Diffractive DIS . . . . . 26

2.9.2 The Kinematics of Diffraction . . . . . 27

2.9.3 The Diffractive Structure Function $\mathbf{F_2^D}(x, Q^2, x_{I\!P}, t)$ . . . . 29

2.9.4 Factorisation . . . . . 30
2.9.5 The Pomeron–Proton Vertex . . . . . 31
2.9.6 The Structure of the Pomeron . . . . . 32
2.10 Photoproduction . . . . . 35
2.11 Monte Carlo Models . . . . . 36
2.11.1 Models of Standard Deep–Inelastic Scattering . . . . . 36
2.11.2 Models of Diffractive Deep–Inelastic Scattering . . . . . 38
2.11.3 Photoproduction Models . . . . . 38

**3 The H1 Detector** **39**

3.1 The HERA Electron–Proton Collider . . . . . 39
3.2 Overview of the H1 Detector . . . . . 39
3.3 Calorimetry . . . . . 42
3.3.1 The Liquid Argon Calorimeter . . . . . 44
3.3.2 The Backward Electromagnetic Calorimeter . . . . . 45
3.3.3 The Plug Calorimeter . . . . . 47
3.3.4 The Tail Catcher . . . . . 48
3.4 Tracking . . . . . 49
3.4.1 The Forward Track Detector . . . . . 51
3.4.2 The Central Tracking Detector . . . . . 51
3.4.3 The Backward Multi-wire Proportional Chamber . . . . . 54
3.5 Muon Detection . . . . . 54
3.5.1 The Instrumented Iron . . . . . 55
3.5.2 The Forward Muon Detector . . . . . 55

3.6 Scintillation Walls . . . . . 56
3.6.1 The Time of Flight System . . . . . 56
3.6.2 The Veto Walls . . . . . 57
3.7 The Electron and Photon Taggers . . . . . 57
3.8 The Proton Remnant Tagger . . . . . 58
3.9 Triggering and Data Acquisition . . . . . 59
3.10 Simulation of the H1 Detector . . . . . 60

**4 Event Selection** **62**

4.1 The Data Sample . . . . . 62
4.2 H1 Data Collection, Reconstruction and Classification . . . . . 62
4.3 Kinematic Reconstruction . . . . . 63
4.4 The Selection of Deep–Inelastic Scattering Events . . . . . 66
4.4.1 On–line Selection . . . . . 68
4.4.2 POT Selection . . . . . 69
4.4.3 DST Selection . . . . . 71
4.4.4 Mini–DST Selection . . . . . 71
4.4.5 Final Selection . . . . . 71
4.4.6 Summary of DIS Selection Procedure . . . . . 77
4.4.7 Remaining Background . . . . . 79
4.4.8 Efficiency of Selection . . . . . 79
4.5 Summary . . . . . 81

**5 The Observation of Diffractive DIS** **82**

5.1 The Observation of Large Rapidity Gap Events . . . . . 82

5.2 The Selection of Large Rapidity Gap Events Using $\eta_{\max}$ . . . . . 83

5.2.1 Background Studies for the $\eta_{\max}$ Selection . . . . . 85

5.3 Properties of the Large Rapidity Gap Events . . . . . 89

5.3.1 Vector Meson Production in the $\eta_{\max}$ Sample . . . . . 91

5.3.2 Comparison with Deep–Inelastic Electron-Pomeron Scattering . . . . . 92

5.4 Beyond the $\eta_{\max}$ Selection . . . . . 95

5.4.1 The Forward Detectors . . . . . 96

5.4.2 Using of the Forward Detector to Select Diffraction . . . . 99

5.4.3 Alternative Selection Prescriptions . . . . . 100

5.4.4 Performance of the Diffractive Selections . . . . . 102

5.4.5 Kinematic Comparisons . . . . . 105

5.4.6 Energy Flow Comparisons . . . . . 110

5.5 Summary . . . . . 110

**6 The Diffractive Structure Function $F_2^D(x, Q^2)$ for $x_{I\!P} \leq 0.01$ 113**

6.1 Introduction . . . . . 113

6.2 The Definition of $F_2^D(x, Q^2)$ . . . . . 114

6.3 The Determination of $F_2^D(x, Q^2)$ . . . . . 116

6.3.1 Subtraction of Background . . . . . 117

6.3.2 Acceptance and Efficiency Corrections . . . . . 120

6.3.3 Bin Corrections . . . . . 123

6.3.4 Radiative Corrections . . . . . 123

6.3.5 Remaining Factors . . . . . 123

6.4 Systematic Errors . . . . . 123

6.5 The Diffractive Contribution to the Proton Structure Function . . 127

6.6 Discussion . . . . . 130

6.7 Summary . . . . . 133

**7 The Diffractive Structure Function $\mathcal{F}_2^D(\beta, Q^2, x_{I\!P})$ 134**

7.1 Introduction . . . . . 134

7.2 The Determination of $\mathcal{F}_2^D(\beta, Q^2, x_{I\!P})$ . . . . . 135

7.2.1 Data and Bin Selection . . . . . 135

7.2.2 Systematic Uncertainties . . . . . 139

7.3 The Diffractive Structure Function $\mathcal{F}_2^D(\beta, Q^2, x_{I\!P})$ . . . . . 140

7.4 Discussion . . . . . 145

7.5 Summary . . . . . 146

**8 The Pomeron Structure Function 147**

8.1 Introduction . . . . . 147

8.2 The Determination of $\tilde{\mathcal{F}}_2^D(\beta, Q^2)$ . . . . . 147

8.3 The Deep–Inelastic Structure of the Pomeron . . . . . 148

8.4 Summary . . . . . 151

**9 The Total Contribution of Diffraction to the Proton Structure Function 152**

9.1 Introduction . . . . . 152

9.2 The Calculation of $F_2^D(x, Q^2)\Big|_{x_{I\!P} \leq 0.1}$ . . . . . 153

9.3 The Diffractive Contribution to the Proton Structure Function . . 154

9.4 Summary . . . . . 157

**10 Summary and Conclusions** **158**

**A Publication of this Analysis** **161**

## Abstract

A measurement is presented, using data taken with the H1 detector at HERA, of the contribution of diffractive interactions to deep–inelastic $ep$ collisions in the kinematic range $8.5 < Q^2 < 50\,\mathrm{GeV}^2$ and $2.4 \times 10^{-4}$ <Bjorken–$x < 0.0133$. Using a sample of events devoid of hadronic energy in the main calorimeter in an interval of pseudo–rapidity adjacent to the proton beam direction, the contribution of diffraction to the proton structure function is evaluated in the kinematic region $x_{I\!P} \leq 0.01$. Using detectors in the forward region of H1 the analysis is extended to establish that the dependence on $x_{I\!P}$ of the diffractive contribution $\mathcal{F}_2^D(\beta, Q^2, x_{I\!P})$ to the proton structure function is $x_{I\!P}^{-n}$ with $n = 1.18 \pm 0.06(stat.) \pm 0.12(syst.)$, independent of $\beta$ and $Q^2$, consistent with a factorisable diffractive interpretation. A first measurement of the deep–inelastic structure of the pomeron $\tilde{\mathcal{F}}_2^{I\!P}(\beta, Q^2)$ is presented, and found to have a significant component over a wide range in $\beta$, and to be consistent with scale invariance for all $\beta$. This is consistent with a partonic interpretation of the substructure of the pomeron.

No portion of the work referred to in this thesis has been submitted in support of an application for another degree or qualification of this or any other institute of learning.

Copyright in text of this thesis rests with the author. Copies (by any process) either in full, or of extracts, may be made **only** in accordance with instructions given by the author and lodged in the John Rylands University Library of Manchester. Details may be obtained from the librarian. This page must form part of any such copies made. Further copies (by any process) of copies made in accordance with such instructions may not be made without the permission (in writing) of the author.

The ownership of any intellectual property rights which may be described in this thesis is vested in the University of Manchester, subject to any prior agreement to the contrary, and may not be made available for use by third parties without the written permission of the University, which will prescribe the terms and conditions of any such agreement.

Further information on the conditions under which disclosures and exploitation may take place is available from the Head of Department of Physics and Astronomy.

This work was supported financially by the Science and Engineering Research Council (S.E.R.C.), latterly the Particle Physics and Astronomy Research Council (P.P.A.R.C.) between October 1991 and October 1994.

# Chapter 1

# Introduction

Deep–inelastic scattering experiments have played a crucial rôle in the development of our current understanding of the structure of the proton. Measurements at the Stanford Linear Accelerator revealed the point–like nature of the constituents of the proton, and have led to a detailed understanding of hadronic matter through the subsequent development and experimental justification of the theory of Quantum Chromodynamics.

Diffractive processes, in which there are no quantum numbers exchanged between groups of initial and final state particles, are known to contribute significantly to high energy hadron–hadron collisions. At present, such low momentum transfer processes are only understood phenomenologically in the framework of Regge theory, and are parameterised as pomeron exchange. Despite the great success of this parameterisation in describing many aspects of hadron–hadron interactions, the pomeron is not understood in any way in terms of partonic QCD dynamics.

At HERA, the very high centre of mass energy of the electron–proton collisions allows the structure of the proton to be studied at values of the Bjorken scaling variable that are more than two orders of magnitude smaller than were previously accessible. Furthermore, the opportunity to measure simultaneously both the scattered electron and hadronic system allows deep–inelastic measurements of diffractive processes to be made for the first time.

In this thesis, the first measurements of the contribution of diffraction to the proton structure function are presented. In chapter 2 the current understanding of the structure of the proton is reviewed, along with a framework within which diffractive deep–inelastic processes may be studied. In chapter 3 the components of the H1 detector used in the analysis are reviewed, and in chapter 4 the way in which this detector is used to select and measure the characteristics of deep–inelastic scattering events is detailed. In chapters 5 to 9 the presence of diffraction in deep–inelastic scattering is suggested, investigated, confirmed and quantified.

The final chapter reviews the results obtained.

# Chapter 2

# Diffraction in DIS at HERA

## 2.1 Introduction

Historically, deep–inelastic scattering has played an important role in elucidating the partonic structure of hadrons. The very large centre of mass energy of $ep$ collisions at HERA permits cross section measurements at values of the Bjorken scaling variable, $x$, down to $\approx 10^{-4}$. Moreover, the availability of information on the hadronic final state allows, for the first time, the structure of any diffractive scattering mechanism to be investigated in the deep inelastic regime, that is, for values of $\beta$, the appropriate Bjorken scaling variable, down to $\approx 10^{-3}$.

## 2.2 Electron–Proton Interactions at HERA

At collider energies, the electron[1]–proton ($ep$) cross section is dominated by inelastic scattering:

$$e^- + p \rightarrow e^- + X \tag{2.1}$$

where the identity of the final state $X$ is arbitrary. The four momentum transfer squared, $Q^2$, is defined

$$Q^2 = -q^2 = -(k^\mu - k'^\mu)^2 \tag{2.2}$$

[1]The HERA accelerator is capable of running with positrons instead of electrons, and unless it is indicated otherwise, the material in this chapter applies equally for positrons.

where $k^\mu$ and $k'^\mu$ are the four momenta of the incoming and outgoing electrons respectively, and the momentum transfer is mediated by a virtual photon, or $Z^0$. The minus sign is introduced such that $Q^2$ is always positive. Such collisions are known as "Neutral Current" (NC) interactions as both exchange bosons have zero electromagnetic charge. Other mechanisms are possible, including the charged current interaction

$$e^- + p \rightarrow \nu_e + X \tag{2.3}$$

where a $W^-$ is exchanged[2]. Interactions involving the exchange of either a $Z^0$ or $W^-$ only contribute significantly at very high values of $Q^2$ because the large masses of these bosons suppress the cross section by the factors

$$\frac{\sigma(Z^0, W^-)}{\sigma(\gamma)} \propto \left| \frac{Q^2}{Q^2 + M^2_{Z^0,W^-}} \right|^2 \tag{2.4}$$

with respect to that for photon exchange.

Neglecting the $Z^0$, the NC interaction may be considered as:

$$\gamma^* + p \rightarrow X \tag{2.5}$$

with the electron acting as a source of space–like virtual photons. When the momentum transfer is small, such that $Q^2 \ll 1\,\mathrm{GeV}^2$, then the photon is nearly on mass shell, or "almost real". Such interactions are known as photoproduction. When the wavelength of the virtual photon is much smaller than the size of the proton ($Q^2 \gg (0.71\,\mathrm{GeV})^2$) and significant energy is transfered, the interaction may be described as "deep–inelastic" scattering (DIS).

## 2.3 Kinematics of Deep–Inelastic Scattering

A schematic representation of a DIS event is shown in figure 2.1. In addition to $Q^2$, the kinematics are commonly described by introducing

$$x = \frac{Q^2}{2P \cdot q} \tag{2.6}$$

[2]For positron–proton collisions the charged current process is $e^+ + p \rightarrow \bar{\nu}_e + X$ where the exchanged boson is a $W^+$.

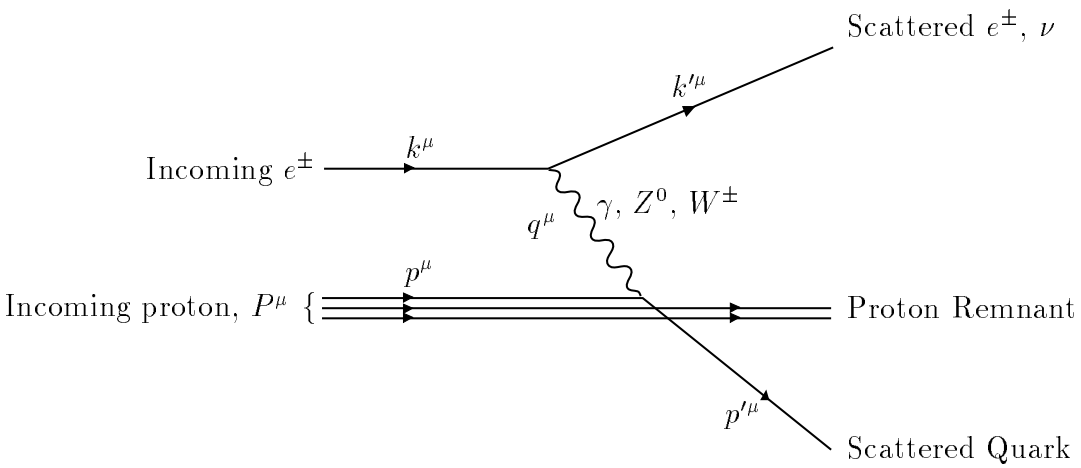


Figure 2.1: The kinematics of deep–inelastic $ep$ scattering in the lowest orders of QCD and QED. The scattered quark along with the two remaining quarks forms the final state $X$ with 4-momentum $P'^{\mu}$.

the Bjorken scaling variable, which in the infinite momentum frame of the proton may be identified as the fraction of the proton's momentum carried by the struck parton[3];

$$y = \frac{P \cdot q}{P \cdot k} \tag{2.7}$$

the fractional energy loss of the electron in the proton rest frame, that is the frame in which HERA collisions are equivalent to fixed target collisions with an incident electron energy of $\sim 23\,\text{TeV}$; and

$$W^2 = (q + P)^2 \tag{2.8}$$

the invariant mass of the final state excluding the scattered electron, commonly referred to as the hadronic final state as all of the particles derive from hadronic fragments of the proton. There are only two independent kinematic variables out of $Q^2$, $x$, and $y$; they are related by

$$Q^2 = sxy \tag{2.9}$$

[3]This identification may be made in any reference frame if the partons are assumed to be mass–less and to have no transverse momentum in the proton.

where $s$ is the centre of mass energy of the $ep$ collision, given by

$$\begin{aligned} s &= (k+P)^2 \\ &= m_e^2 + m_p^2 + 2k \cdot P \\ &= m_e^2 + m_p^2 + 2E_e E_p - 2\mathbf{k} \cdot \mathbf{P} \\ &\simeq 4E_e E_p \end{aligned} \tag{2.10}$$

where $E_e$ and $E_p$ are the incident energies of the electron and proton. For $E_e = 26.7\,\text{GeV}$ and $E_p = 820\,\text{GeV}$ then $s = 87576\,\text{GeV}^2$. $W^2$ and $Q^2$ are related by

$$W^2 = \frac{(1-x)Q^2}{x} + m_p^2 \tag{2.11}$$

## 2.4 The Structure of the Proton

The inclusive differential cross section for the inelastic collisions between electrons and protons, both spin–$\frac{1}{2}$ particles, may be written

$$\frac{d^2\sigma(ep \to eX)}{dE'd\Omega} = \frac{\alpha^2}{Q^4}\frac{E'}{E}L_{\mu\nu}W^{\mu\nu} \tag{2.12}$$

where $E$ and $E'$ are the initial and final energies of the scattered electron. At values of $Q^2$ where the cross section is dominated by photon exchange, then $L_{\mu\nu}$ is simply the lepton tensor from QED. Constraints of Lorentz invariance and current conservation allow the unknown hadron tensor, $W^{\mu\nu}$, to be parameterised in terms of a minimum of two independent functions such that the cross section may be written

$$\frac{d^2\sigma(ep \to eX)}{dxdQ^2} = \frac{4\pi\alpha^2}{xQ^4}\left[y^2 xF_1 + (1-y)F_2\right] \tag{2.13}$$

although this formalism is, as yet, devoid of predictive power.

### 2.4.1 The Quark Parton Model

The naive parton model, or quark parton model (QPM) assumes that the proton is composed of free, point–like fermions, called quarks, whose momentum distributions are described by parton density functions, $f_i(x, Q^2)$, whose normalisation

are constrained by the momentum sum rule

$$\sum_i \int_0^1 dx\, x\, f_i(x) = 1 \tag{2.14}$$

where the sum is over all the different types of quarks. This simply states that the quarks account for all of the momentum of the proton. A consequence of the assumption that lepton-quark scattering is point–like is that these parton density functions should only depend on $x$, that is, be independent of $Q^2$, or "scale invariant", as $x$ contains no scale of mass or length. This is the Bjorken Scaling Hypothesis [1]. By writing the cross section for electron–proton scattering in terms of parton density functions, a relationship between these functions and the structure functions $F_1$ and $F_2$ may be identified

$$F_2 = x \sum_i e_i^2\, f_i(x) \tag{2.15}$$

where

$$F_2 = 2xF_1 \tag{2.16}$$

Equation 2.16, known as the Callan-Gross relationship, is a direct consequence of the spin–$\frac{1}{2}$ nature of quarks: for spin zero partons the ratio $\frac{2xF_1}{F_2}$ would be zero. The cross section may now be written entirely in terms of $F_2(x, Q^2)$ and the parameter $R(x, Q^2)$, defined

$$R(x, Q^2) = \frac{F_2(x, Q^2) - 2xF_1(x, Q^2)}{2xF_1(x, Q^2)} \tag{2.17}$$

such that

$$\frac{d^2\sigma_{ep}}{dxdQ^2} = \frac{2\pi\alpha^2}{xQ^4}\left[2(1-y) + \frac{y^2}{1+R}\right] \cdot F_2(x, Q^2) \tag{2.18}$$

where $R = 0$ corresponds to the Callan-Gross relationship being satisfied.

Scaling was indeed observed at the Stanford Linear Accelerator in DIS in 1969 [2], and measurements of the the ratio $\frac{2xF_1}{F_2}$ at the same experiment confirmed the spin-$\frac{1}{2}$ nature of the point–like partons.

### 2.4.2 QCD Evolution and the Violation of Scaling

Early experiments demonstrated that quarks can only account for about half of the proton momentum; the left hand side of equation 2.14 was found to be

equal to $0.5 \pm 0.05$ [3]. Scale invariance is observed to be approximately true for $x \approx 0.15$, but significant variations of the structure function $F_2$ with $Q^2$ are observed at higher and lower values of $x$ (figure 2.2). These deviations from the expectations of the quark parton model are explained by the theory of quantum chromodynamics (QCD).

In QCD, the quarks are not quite free, but interact through strong interactions mediated by bosons called gluons. That the gluons interact with themselves as well as with the quarks permits the strength of the coupling, $\alpha_s(Q^2)$, to decrease with increasing $Q^2$, in contrast with QED where the strength of the coupling may only increase[4]. As $Q^2 \to \infty$ then $\alpha_s(Q^2) \to 0$. This property is known as asymptotic freedom, and has the consequence that at sufficiently high values of $Q^2$, the quarks appear to be free.

Here, $Q^2$ represents the momentum transfer scale relevant to the "hard scattering" process, that is, the process to which a partonic interpretation is applied. This need not, necessarily, be the four–momentum transfer at the electron vertex (equation 2.2).

When $\alpha_s(Q^2)$ is small, solutions to QCD may be well approximated by perturbative expansion, and QCD processes may be treated within the framework of Feynman diagrams. The scale at which perturbative quantum chromodynamics (pQCD) is no longer valid is taken typically to be $Q^2 \sim 1\,\mathrm{GeV}^2$.

QCD permits a simple interpretation of the violation of the scaling hypothesis. As the virtuality of the probe ($Q^2$) increases, the structure of the proton is revealed in finer detail. The quarks within the proton begin to be seen as quarks surrounded by a cloud of virtual partons, and the effects of gluon bremsstrahlung, where high momentum quarks lose momentum through the emission of soft gluons, must be taken into account. As $Q^2$ increases, there is a higher probability of finding a quark at low $x$ which has lost momentum through gluon bremsstrahlung, and so a smaller one of finding a quark at high $x$. This means that at high values of $x$, $F_2(x, Q^2)$ should decrease with increasing $Q^2$, whilst at low values of $x$ it should increase.

[4]The non-Abelian nature of the strong interaction allows $\alpha_s(Q^2)$ to rise or fall with increasing $Q^2$. The number of degrees of freedom (colours) in the theory constrains it to fall.

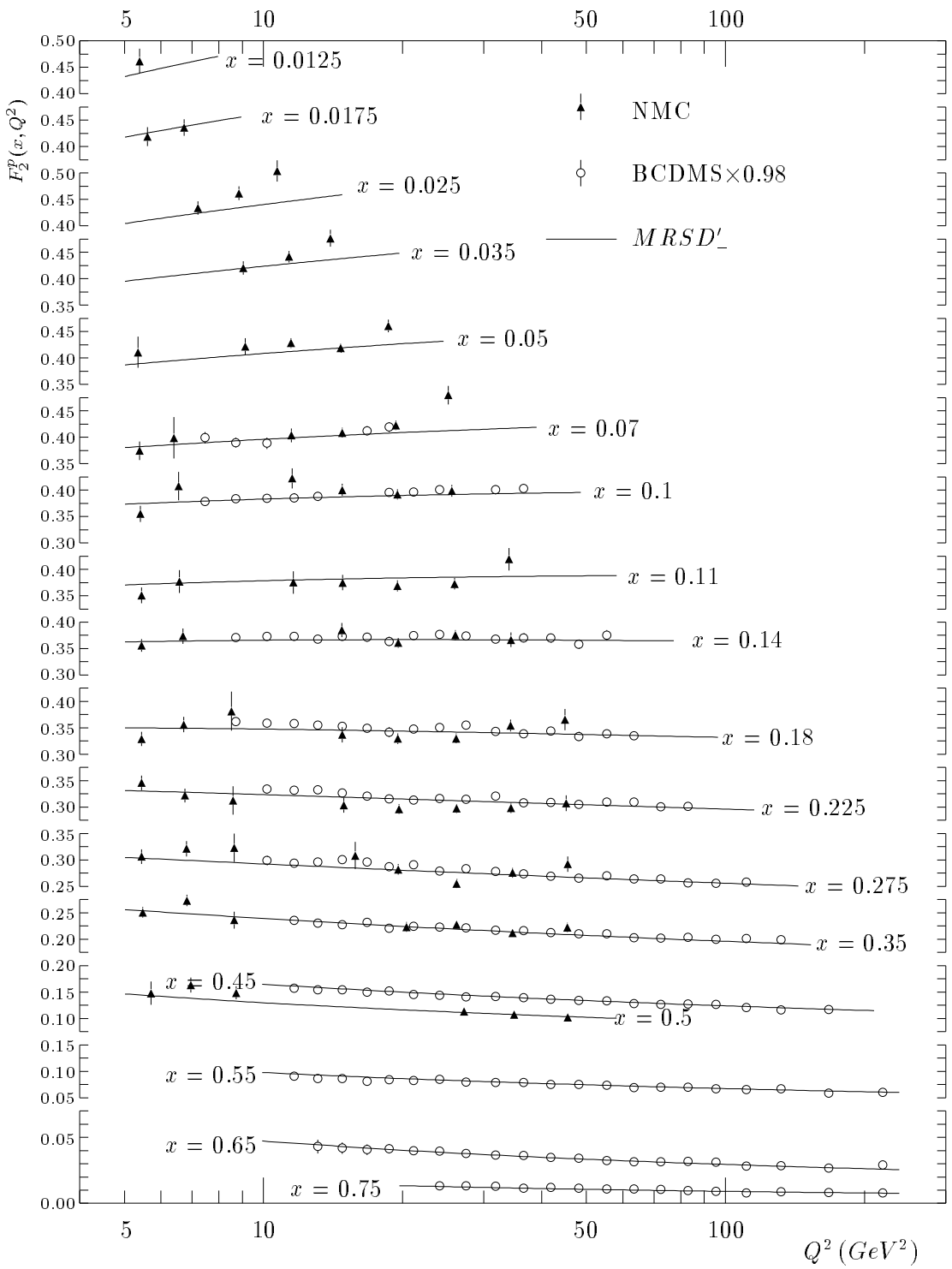


Figure 2.2: $F_2^p(x,Q^2)$ from NMC and BCDMS for $Q^2 > 5\,GeV^2$. Also shown is the prediction using the $MRSD'_-$ parton density distributions, which are based on the DGLAP evolution equations. In the fit of the $MRS$ distributions it was found that the BCDMS data needed to be scaled by a factor of 0.98.

The mechanism of these scaling violations is formalised in the Dokshitzer, Gribov, Lipatov, Altarelli, Parisi (DGLAP) evolution equations [4]. Considering the radiation of a single gluon from a quark results in the modification of the structure function from equation 2.15 to

$$F_2(x,Q^2) = \sum_i e_i^2 \int_x^1 \frac{dy}{y} f_i(y) \left( \delta\left(1-\frac{x}{y}\right) + \frac{\alpha_s}{2\pi} P_{qq}\left(\frac{x}{y}\right) \log\frac{Q^2}{\mu^2} \right) \tag{2.19}$$

where $P_{qq}(\frac{x}{y})$ represents the probability of a quark of momentum fraction $x$ reducing its momentum by a fraction $y$ by radiating a gluon. The regularisation parameter $\mu^2$ is introduced to avoid divergences. In addition to the radiation of a single gluon from a quark ($q \rightarrow q+g$), the DGLAP equations include the possibility of a gluon splitting into a quark or a gluon pair ($g \rightarrow q+\bar{q}$ or $g \rightarrow g+g$).

Taken in full, the DGLAP equations permit a parton density known for all $x$ at a certain $Q_0^2$, where $Q_0^2$ is large enough to allow perturbative calculations, to be predicted for all $x$ and all $Q^2 > Q_0^2$. Since the data do not cover the entire range in $x$, extrapolations are necessary from high $x$, where the structure function has been measured with great precision, into the low–$x$ region, thus introducing theoretical uncertainty.

It should be noted that at very low values of $x$ (less than $\sim 10^{-4}$) and moderately small $Q^2$ (less than $\sim< 10\,\mathrm{GeV}^2$), it is not clear that the DGLAP formalism is sufficient to describe the gluon dominated structure of the proton. The limitation of the DGLAP formalism is that for gluon initiated processes like that shown in figure 2.3, the momenta of the gluons in the "ladder" must be strongly ordered in transverse momentum such that

$$Q^2 \gg k_{T_n}^2 \gg \ \ldots\ k_{T_i}^2\ \ldots\ \gg k_{T_1}^2 \tag{2.20}$$

It has not been demonstrated that this approximation is valid, and a relaxation of this strong ordering is possible with the Balitsky, Fadin, Kuraev, Lipatov (BFKL) evolution equations [5].

Whereas the DGLAP equations predict the $Q^2$ dependence of the parton densities, the BFKL equation predicts the $x$ behaviour. When the effect of the variation of $\alpha_s$ with $Q^2$ may be neglected, that is in a small range in $Q^2$, the BFKL evolution may be solved analytically to give a solution for the gluon density $\propto x^{-\lambda}$

at low $x$ with

$$\lambda = \frac{12\alpha_s}{\pi} \log 2 \approx 0.5 \tag{2.21}$$

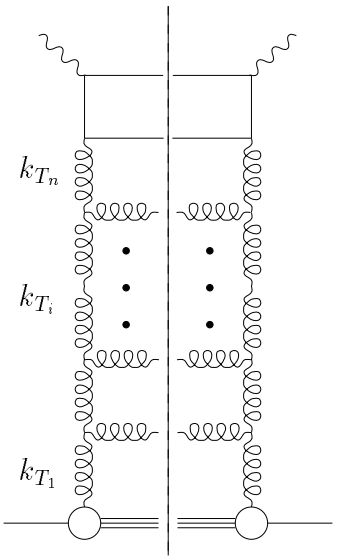


Figure 2.3: QCD evolution in DIS at low $x$. The complete figure represents the squared amplitude that must be calculated to obtain the cross section. When the gluon ladder is "cut" along the dotted line, the Feynman diagram for the deep inelastic scattering process is obtained. The DGLAP and BFKL equations differ in the treatment of such diagrams in the way in which the gluons are ordered in increasing transverse momentum ascending from the proton vertex.

### 2.4.3 Measurement of the $F_2(x, Q^2)$ at HERA

The high centre of mass energy at HERA allows precision measurements of the proton structure function $F_2(x, Q^2)$ to be made at values of $x$ down to $\sim 10^{-5}$ at values of $Q^2 > 1\,\mathrm{GeV}^2$. Comparison of measurements of $F_2(x, Q^2)$ at different centre of mass energies, that is, with different incident beam energies, should permit measurements of $F_1$.

A recent measurement of the proton structure function [6] made by the H1 collaboration is shown as a function of $x$ at different values of $Q^2$ in figure 2.4.

Similar measurements have also been made by the ZEUS collaboration [7], and the data from both experiments exhibit a strong rise in $F_2(x, Q^2)$ as $x$ decreases. Note that the data shown in figure 2.4 are extracted using a QCD calculation of R (equation 2.17) which relies on assumptions about the parton density functions.

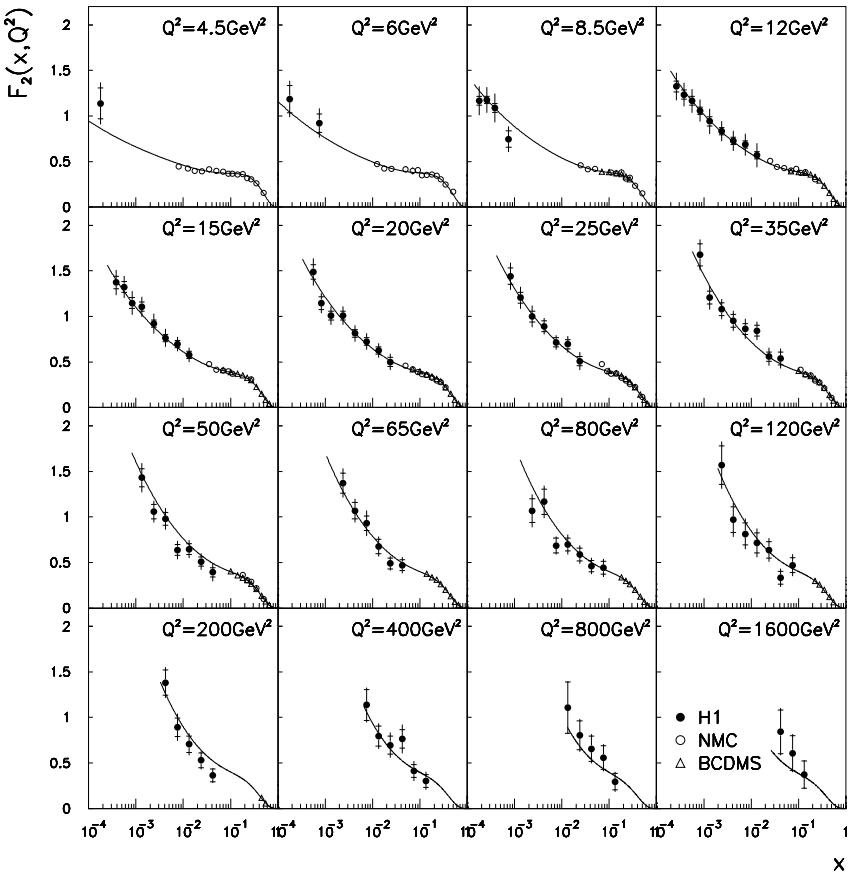


Figure 2.4: The proton structure function $F_2(x, Q^2)$ as a function of $x$ at different values of $Q^2$. The closed circles represent the H1 data. The inner error bars denote the statistical errors, while the full error bars represent the statistical and systematic errors added in quadrature, not taking into account the 5% systematic error on the measurement of the luminosity. Open circles and triangles represent NMC and BCDMS measurements respectively. The curve is the result of a next to leading order QCD fit based on the DGLAP evolution equations. The $x$ dependence may be well described by $F_2(x) \propto x^{-0.3}$ at low $x$.

## 2.5 From Partons to Hadrons

So far, this discussion of electron–proton collisions has only considered processes at the level of partons. That free partons are never observed, only colour singlet hadron states, is understood to be a consequence of the variation of the strength of the strong coupling, $\alpha_s(Q^2)$, with the momentum scale of the interaction, $Q^2$. Though partons may be treated as effectively free at very high energies (small distances), as the outgoing partons leave the scattering process, the strength of the strong coupling becomes rapidly very large such that coloured objects are never observed in the macroscopic world. This property of QCD is known as "colour confinement". Thus the initial scattering process must be followed by a process in which the outgoing, coloured partons convert into colour singlet states.

The process by which partons combine into hadrons is considered in two distinct phases: one in which the application of perturbative QCD is appropriate, and one in which it is not. The first stage is commonly known as "parton showering", and amounts to the application of higher order QCD corrections to the description of the hard scattering process. Diagrams in which the incoming and outgoing partons undergo QCD bremsstrahlung processes ("initial" and "final" state parton showers) are calculated using the DGLAP equations (section 2.4.2) until the virtuality of the partons reaches a scale at which perturbative calculations are no longer applicable (typically $1\,\mathrm{GeV}^2$). After this stage is reached, a purely phenomenological approach must be adopted the convert the remaining partons into colourless states. The second stage, known as fragmentation, is usually described by considering colour "strings" stretched between the partons which break to produce colourless hadrons and other particles as the partons separate. Many parameters in the models of fragmentation are incalculable; rather, they are adjusted to match the observed characteristics of the data.

## 2.6 QED Radiative Corrections

So far, only single photon exchange has been considered in the DIS process $ep \to eX$. Higher order processes in QED have the consequence that the kinematics

determined from the electron no longer correspond to the kinematics at the proton vertex, which are the kinematics relevant to the structure functions. This means that the measured, or "radiative" cross section must be corrected for these higher order effects to determine the Born cross section, and thus the structure functions.

The processes which produce the largest differences between the radiative and Born cross sections are those involving initial state radiation. Initial state radiation, where the incident electron emits a real photon before entering the scattering process, results in a reduction of the true centre of mass energy such that the value of $y$ reconstructed from the electron is too high if the nominal beam energies are assumed. The effects of initial state radiation are reduced if very high values of $y$ are not considered because an electron energy close to the nominal beam energy is kinematically incompatible with the emission of a highly energetic photon. Final state radiation does not result in significant corrections since the radiated photon is typically almost collinear with the scattered electron, and so not resolved as separate from the electron in the apparatus. Whilst radiative corrections are calculable with great precision given the proton structure functions at all values of $x$ and $Q^2$, some uncertainty is inevitable due to the migration of events into the data sample from outside the kinematic domain defined at the Born level.

## 2.7 Diffraction

In the diffractive interactions of hadrons, one or both of the incident hadrons emerge from the scattering process either intact, or in a low mass excited state. Diffractive processes are characterised by rapidity gaps, that is large regions in pseudo–rapidity[5], $\eta$, between the emerging particles that are devoid of any significant energy, where $\eta$ is defined

$$\eta = -\ln \tan \frac{\theta}{2} \tag{2.22}$$

where $\theta$ is the polar angle of the particle. This lack of energy may be interpreted by the exchange of a colourless object mediating the long range strong interaction between hadrons.

[5] "True" rapidity is never used in this work, and pseudo–rapidity is abbreviated to rapidity.

These scattering processes are highly peripheral: the momentum transfer involved, $t$, is very small, typically $-t \leq 1\,\mathrm{GeV}^2$. For such soft (small momentum transfer) processes, a perturbative treatment has not been achieved.

## 2.8 Regge Theory and The Pomerančuk Pole

The characteristics of diffraction at collider energies are well described by the phenomenological model known as the Regge theory [8, 9]. This theory has allowed many successful predictions to be made concerning the long range, perturbatively incalculable, strong forces between hadrons. In Regge theory, a scattering process, for example $p + p \rightarrow p + p$ in the $s$ channel is described by considering the equivalent $t$ channel process, here $p + \bar{p} \rightarrow p + \bar{p}$. The set of all possible resonance states that conserve quantum numbers (charge, spin, parity, baryon number etc.) are linked in energy–angular momentum space by a path known as a Regge trajectory, and the physical particles along it at positions of integral spin are known as "poles" of the trajectory, or Regge Poles. It is the extrapolation of this trajectory from the $t$ channel (positive $t$) back into the $s$ channel (negative $t$) that governs the energy dependence of the scattering process. Thus the characteristics of the cross section for $p + p \rightarrow p + p$ are determined by the mass and spin of all of the possible intermediate states in the equivalent $t$ channel process. Regge theory successfully describes the $t$ and $s$ dependence, along with other characteristics, of many inelastic collisions (for example $\pi^- + p \rightarrow \pi^0 + n$ and $\pi^- + p \rightarrow \rho^0 + n$).

A prediction of Regge theory is that the energy dependence of a particular $s$–channel process in the limit $-t \approx 0$ is governed by the intercept of the corresponding Regge trajectory $\alpha(t)$ at $t = 0$ such that

$$\frac{d\sigma(s)}{dt} \propto s^{2\alpha(0)-2} \tag{2.23}$$

where $s$ is the centre of mass energy. All of the known hadrons lie along Regge trajectories with intercepts $\alpha_i(0)$ less than $\approx 0.6$. For example, the two trajectories along which the $\rho(770)$ and $\omega(782)$ lie have intercepts at 0.6 and 0.5 respectively. Thus, for both of these trajectories the cross section falls rapidly with increasing centre of mass energy. This is in stark contrast to the total cross sections for

$pp$ and $p\bar{p}$ scattering, where the dependence on $s$ is roughly constant[6]. In the language of Regge theory, such behaviour corresponds to a trajectory formed by particles which have vacuum quantum numbers (zero charge, zero isospin, zero baryon number, positive parity) and even spin, and the lowest mass Regge pole is known as the pomeron ($\mathbb{P}$), after Pomerančuk. That no physical particles have been observed corresponding to this trajectory, which dominates hadron interactions at high energies, explains the enduring theoretical interest in the identity of the $\mathbb{P}$. Processes associated with $\mathbb{P}$ exchange are known as diffractive.

## 2.9 Diffractive Deep–Inelastic Scattering

### 2.9.1 Standard and Diffractive DIS

Figure 2.5 shows a non-diffractive deep–inelastic scattering process (hereafter referred to as "standard-DIS") contrasted with one involving a colourless exchange, which, if the colourless exchange is a $\mathbb{P}$, is a diffractive deep–inelastic scattering process (henceforth referred to as diffractive–DIS). In the standard–DIS process the virtual photon couples to a coloured component of the proton, a quark, such that the colour of the proton is opened up. The resultant final state includes a scattered or "current" quark and two remnant or spectator quarks which continue near to the original direction of the proton. Typically, two jets, that is collimated groups of particles, are present after hadronisation: the current jet, and the remnant jet, which are near to the original directions of the current quark and remnant quarks respectively. Though much of the remnant jet usually escapes from the H1 apparatus into the forward beam–pipe, the current jet is well contained within the detector, except at very high values of $x$. A colour field connects the scattered and remnant quarks such that the condensation of this field during hadronisation fills this intervening region of rapidity with hadrons. Though random fluctuations in the hadronisation process may result in empty regions of rapidity, the production of large rapidity gaps by this mechanism is expected to be exponentially suppressed with increasing gap size [10].

In diffractive processes (figure 2.5b), the photon does not interact directly

[6] In fact the cross section rises slightly with increasing $s$ (see section 2.9.5).

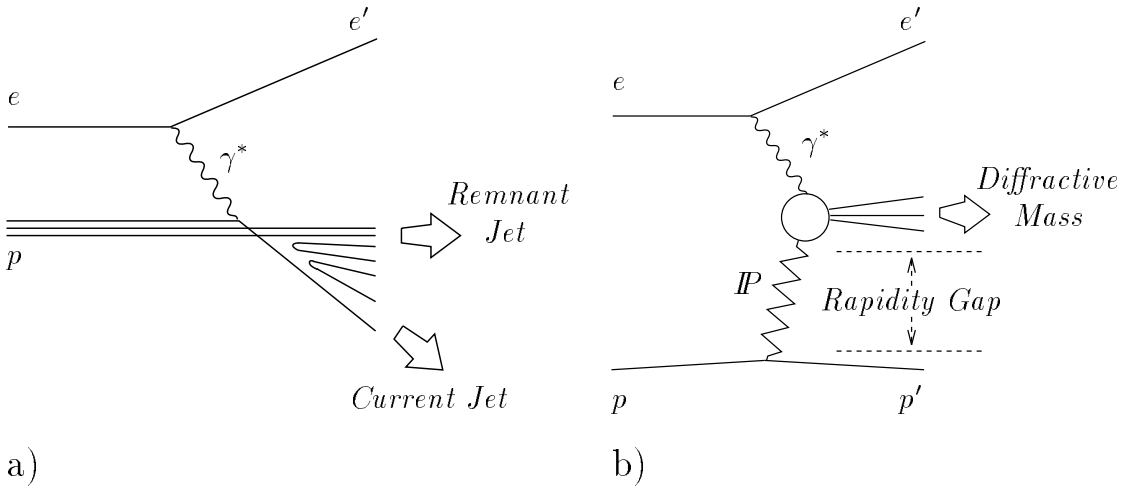


Figure 2.5: a) Standard–DIS. b) Diffractive–DIS. The rapidity gap between the elastically scattered proton and the diffractive mass is associated with the colourless exchange, the IP. If the scattered proton dissociates, the rapidity gap is between the decay products of the proton and the diffractive mass.

with the proton, but with a colourless component of it, here a IP. The proton emerges from the interaction either intact, or in a low mass excited state[7]. As there is no colour connection between the scattered proton and the remainder of the final state, no hadrons are produced in between, resulting in a large rapidity gap containing little or no energy.

In the absence of detector apparatus dedicated to tagging the scattered proton, the large rapidity gap is the experimental signature of events involving a colourless exchange.

### 2.9.2 The Kinematics of Diffraction

The vectors used to parameterise diffractive–DIS are shown in figure 2.6. In such processes, two further degrees of freedom are introduced: the scattering angle and energy loss of the proton, such that in addition to the usual kinematic variables,

[7] $N^*$ for double diffractive dissociation (proton dissociation), $N^*$ or $\Delta$ for non–diffractive exchanges.

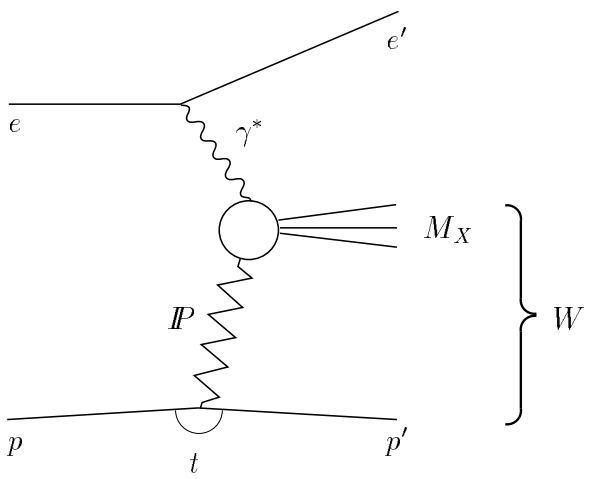


Figure 2.6: The kinematics of diffractive–DIS. $W$ is the invariant mass of the total final state excluding the scattered electron; $M_X$ is that excluding both scattered electron and proton (or colourless remnant.) In standard–DIS, where no colourless remnant exists, $M_X = W$. The 4–momentum transfer at the proton vertex, $t$, is the virtuality of the IP.

$x$, $y$, $Q^2$ and $W^2$, the following quantities may be defined:

$$t = (p - p')^2 \tag{2.24}$$

the momentum transfer squared at the proton vertex;

$$x_{I\!P} = \frac{q.(P - p')}{q \cdot P} = \frac{Q^2 + M_X^2 - t}{Q^2 + W^2 - m_p^2} \approx \frac{Q^2 + M_X^2}{Q^2 + W^2} \tag{2.25}$$

and

$$\beta = \frac{Q^2}{Q^2 + M_X^2 - t} \approx \frac{Q^2}{Q^2 + M_X^2} \tag{2.26}$$

where $M_X$ is the invariant mass of the hadronic final state excluding the colourless remnant. Kinematic constraints lead to a minimum bound[8] on $|t|$, given by

$$t_{min} \approx -\frac{Q^2}{2x} + \frac{m_f^2 + m_p^2}{2} + \frac{Q^2}{2x}\sqrt{\left[1 - x\frac{(m_f + m_p)^2}{Q^2}\right]\left[1 - x\frac{(m_f - m_p)^2}{Q^2}\right]} \tag{2.27}$$

in the limits $m_p^2 \ll Q^2$ and $x \ll 1$, where $m_f$ is the mass of the colourless remnant, equal to $m_p$ if the proton remains intact [11].

[8]The usual convention that $t_{min} > t$ specifies the less negative kinematic limit on $t$ is adopted.

If $|t|$ is small, and the centre of mass energy is much greater than the proton rest mass, then $x_{I\!P}$ and $\beta$ may be identified with the fraction of the proton momentum carried by the $I\!P$, and the fraction of the momentum of the $I\!P$ that enters the hard scattering process respectively. Thus $\beta$ can be considered as the scaling variable relevant to deep–inelastic electron–pomeron collisions, equivalent to the Bjorken–$x$ in electron–proton scattering. Note that

$$x = x_{I\!P} \cdot \beta \tag{2.28}$$

Kinematic constraints [12] also lead to a minimum bound on the expected size of the rapidity gap in the hadronic final state between the colourless remnant and the diffractive mass of

$$\Delta\eta \geq \ln \frac{1}{x_{I\!P}} \tag{2.29}$$

Considering the process $ep \rightarrow epX$ within the framework of Regge theory (section 2.8) the double differential cross section $\frac{d^2\sigma_{ep\rightarrow epX}}{dtdM_{Xe}}$ exhibits the behaviour

$$\frac{d^2\sigma}{dt\, dM_{Xe}} \propto \left(\frac{s}{M_{Xe}^2}\right)^{2\alpha(t)-1} \tag{2.30}$$

where $M_{Xe}$ is the invariant mass of the final state including the scattered electron, but excluding the scattered proton, and $\alpha(t)$ is the leading Regge trajectory. If $|t|$ is small, and $s \gg m_p^2$ then $M_{Xe}^2$ is simply $s \cdot x_{I\!P}$ and so the cross section follows

$$\frac{d^2\sigma}{dt\, dM_{Xe}} \propto \left(\frac{1}{x_{I\!P}}\right)^{2\alpha(0)-1} \tag{2.31}$$

such that for $I\!P$ exchange, where $\alpha_{I\!P}(0) \simeq 1$, the behaviour is approximately $\propto \frac{1}{x_{I\!P}}$. This is in marked contrast to the dependence expected for the other Regge trajectories where the cross section remains roughly constant or even rises with increasing $x_{I\!P}$. This leads to the expectation that $I\!P$ exchange should rapidly become the dominant mechanism for rapidity gap production as $x_{I\!P}$ decreases below 0.1.

### 2.9.3 The Diffractive Structure Function $\mathbf{F_2^D}(x, Q^2, x_{I\!P}, t)$

Although the success of the Regge formalism lends much support to the hypothesis of factorisation, it offers no insight into the structure or identity of the $I\!P$. It

has been suggested that if the $\mathbb{P}$ has partonic sub–structure, then such structure may be probed in diffractive hard scattering interactions [13, 14, 15, 12], such as diffractive–DIS.

To facilitate the search for evidence of partonic sub–structure within the $\mathbb{P}$, the cross section for $ep \rightarrow epX$ may be conveniently expressed in terms of a "diffractive structure function" [16, 17] defined

$$\frac{d^4\sigma_{ep\rightarrow epX}}{dxdQ^2dx_{I\!P}dt} = \frac{2\pi\alpha^2}{xQ^4}\left[2(1-y)+\frac{y^2}{1+R^D}\right]\cdot \mathbf{F_2^D}(x,Q^2,x_{I\!P},t) \tag{2.32}$$

where the contribution from $Z^0$ exchange is neglected. The parameter $R^D$ is not necessarily the same as the $R$ entering into the totally inclusive cross section (equation 2.18) as although the process considered involves the collisions of spin–$\frac{1}{2}$ electrons and protons, the cross section described is no longer totally inclusive. No calculation for $R^D$ exists, and for the remainder of this work $R^D = 0$ is taken, following [17].

### 2.9.4 Factorisation

It has been suggested [17, 14, 15] that this structure function may be factorised into two components, such that

$$\mathbf{F_2^D}(x,Q^2,x_{I\!P},t) = f_{I\!P/p}(x_{I\!P},t)\cdot F_2^{I\!P}(\beta,Q^2) \tag{2.33}$$

where $f_{I\!P/p}(x_{I\!P},t)$ is known as the pomeron flux factor, and parameterises the soft, non-perturbative dynamics associated with production of a $\mathbb{P}$ from a proton. The second term, the "pomeron structure function" $F_2^{I\!P}(\beta,Q^2)$ is then associated with the structure of the hard interaction between the pomeron and the virtual photon. If this hypothesis is valid, then these two functions should be entirely independent of one another. The factorisation hypothesis is motivated by the considerable success with which Regge phenomenology describes inelastic and elastic scattering in hadron–hadron collisions [18].

### 2.9.5 The Pomeron–Proton Vertex

The relevant momentum scale at the proton–$\mathbb{P}$ vertex is $t$ (typically $|t| \ll 1\,\mathrm{GeV}^2$), and so a perturbative treatment is not appropriate. Various parameterisations for $f_{\mathbb{P}/p}(x_{\mathbb{P}}, t)$ exist, based upon Regge–inspired fits of pre–HERA data. Donnachie and Landshoff [15] use Regge theory together with an elastic form factor for the proton and find

$$f_{\mathbb{P}/p}(x_{\mathbb{P}}, t) = \left(\frac{31.5}{4\pi^2}\right) \cdot \left(\frac{4m_p^2 - 2.8t}{4m_p^2 - t}\right) \cdot \left(\frac{1}{[1 - t/0.7]^2}\right) \cdot \left(\frac{1}{x_{\mathbb{P}}}\right)^{2\alpha_{\mathbb{P}}(t)-1} \tag{2.34}$$

where

$$\alpha_{\mathbb{P}}(t) = \alpha_{\mathbb{P}}(0) + \alpha'_{\mathbb{P}} t = 1 + \epsilon + 0.25t \tag{2.35}$$

The parameter $\epsilon = 0.085$ describes the rise in the total cross section in $p\bar{p}$ and recently in $\gamma p$ [19]. Ingelman and Schlein [13] determine the dependence on $x_{\mathbb{P}}$ and $t$ from fits to data, using Regge theory only for the total normalisation, and obtain

$$f_{\mathbb{P}/p}(x_{\mathbb{P}}, t) = \frac{1}{2.3}\left[6.38e^{-8|t|} + 0.424e^{-3|t|}\right] \cdot \left(\frac{1}{x_{\mathbb{P}}}\right) \tag{2.36}$$

whereas Berger, Collins and Streng [12, 14] suggests

$$f_{\mathbb{P}/p}(x_{\mathbb{P}}, t) = \frac{100}{16\pi} \cdot \left(\frac{1}{x_{\mathbb{P}}}\right)^{2\alpha_{\mathbb{P}}(t)-1} \cdot e^{-R_N^2|t|} \tag{2.37}$$

where $R_N^2 = 4.7\,\mathrm{GeV}^{-2}$. In all three parameterisations $t$ is in GeV.

Considered over the HERA kinematic regime, ($10^{-4} < x_{\mathbb{P}} < 10^{-1}$), these three parameterisations differ by less than a factor 2 in overall normalisation, and all resemble the basic behaviour $f_{\mathbb{P}/p}(x_{\mathbb{P}}, t) \propto x_{\mathbb{P}}^{-1}$ expected from simple Regge theory.

Since the squared amplitude in figure 2.3 is similar to the Feynman diagram for a diffractive scattering process involving the exchange of a gluon ladder with no overall colour, the two gluon system described by the BFKL equations is often referred to as the "BFKL pomeron". In this analogy [20] the intercept of this pomeron, $\alpha_{\mathrm{BFKL}}(0)$ is $\lesssim 1 + \lambda$. The BFKL equations then represents another framework within which the diffractive exchange of two gluons may be considered.

It is possible, then, that the dependence on $x_{\mathbb{P}}$ may be complicated by the presence of both a "soft" $\mathbb{P}$ with $\alpha_{\mathbb{P}}(0) \sim 1$ as outlined above, and a "hard"

$\mathbb{P}$, corresponding to the BFKL pomeron with $\alpha_{\text{BFKL}}(0) \lesssim 1.5$. If the latter contributes at the very small values of $|t|$ that dominate the overall diffractive cross section, then the resulting dependence of $\mathbf{F_2^D}(x, Q^2, x_{\mathbb{P}}, t)$ on $x_{\mathbb{P}}$ may be both more complicated than $\propto x_{\mathbb{P}}^{-n}$ and steeper.

### 2.9.6 The Structure of the Pomeron

It has been argued that under the assumption of factorisation, it is natural to treat the pomeron as an effective hadron, that is an object, containing partons, with significant spatial extent. Within the framework of QCD, the large momentum scale, $Q^2$, introduced into the hard interaction by the highly virtual photon, allows a perturbative treatment of the structure of the $\mathbb{P}$, in the same way in which pQCD may be applied in calculations of the structure of the proton. Furthermore, the potentially small size of the $\mathbb{P}$ compared to that of the proton may make the $\mathbb{P}$ particularly sensitive to non–linear QCD phenomena, associated with, for example, gluon recombination [17].

Clear evidence exists for inelastic diffractive hard scattering in the observation of high $P_T$ jets in $p\bar{p}$ data [21]. These data favour a hard partonic structure [22], although there is debate as to whether discrimination is permitted between a quark or gluon dominated pomeron [17, 23].

A partonic interpretation of a factorisable pomeron leads to the identification of $F_2^{\mathbb{P}}(\beta, Q^2)$ with the parton density functions in the pomeron, $f_i(\beta, Q^2)$, such that

$$F_2^{\mathbb{P}}(\beta, Q^2) = \sum_i e_i^2 \left[\beta f_i(\beta, Q^2)\right] \tag{2.38}$$

where the sum is over all the different partons. It is unclear whether the partons within the pomeron obey the momentum sum rule:

$$\int_0^1 \sum_i x f_i(x) = 1 \tag{2.39}$$

where $f_i(x)$ are the parton density functions, or whether the hard scattering is mediated predominantly by quarks (figure 2.7b) or gluons (figure 2.7c).

It is commonly assumed that the $\mathbb{P}$ is composed of gluons. In analogy with the long range van der Waals forces between atoms and molecules, diffractive

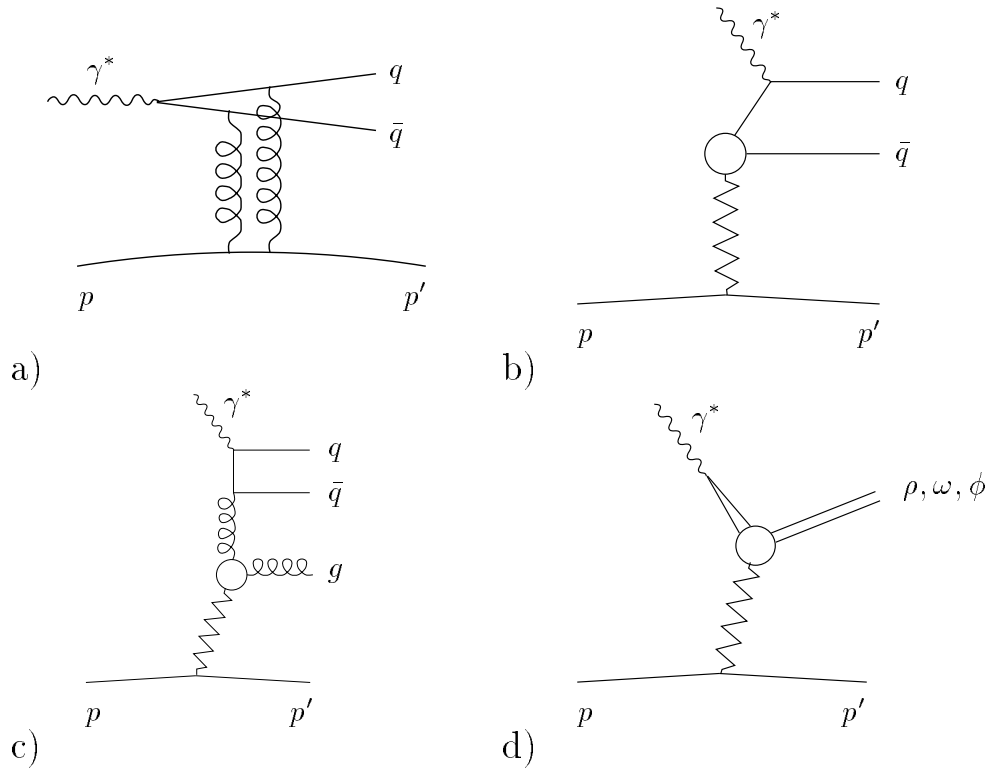


Figure 2.7: Different models of pomeron induced processes in DIS. a) The Nikolaev-Zakharov model. The two gluons may also couple to the same quark, in which case the picture is similar to the Low-Nussinov Pomeron underlying the picture of Donnachie and Landshoff. b) The simple two-quark model. c) The simple two gluon model. d) The direct interaction, in which the entire momentum of the pomeron enters to scattering process, here producing a light vector meson ($\rho(770), \omega(783), \phi(1020)$). In model b)-d) the pomeron is parameterised by a phenomenological flux.

interactions are considered as multi–gluon exchanges associated with the long range QCD interactions between hadrons [14]. If deep–inelastic $e$-$\mathbb{P}$ collisions are gluon initiated (figure 2.7c), then two extreme gluon distributions which obey the sum rule may be derived:

$$x_{g/\mathbb{P}}\, g(x_{g/\mathbb{P}}) = 6x_{g/\mathbb{P}}(1 - x_{g/\mathbb{P}}) \tag{2.40}$$

for a pomeron containing two gluons or

$$x_{g/\mathbb{P}}\, g(x_{g/\mathbb{P}}) = 6(1 - x_{g/\mathbb{P}})^5 \tag{2.41}$$

where the gluons are as soft as the gluon sea in a nucleon [12, 14, 13]. Here $x_{i/\mathbb{P}}$ is the momentum fraction of the $\mathbb{P}$ carried by the parton $i$, where $i = q$ for quarks

and $i = g$ for gluons. For gluon initiated scattering a coupling to the virtual photon is only possible through a quark pair such that $\beta \leq x_{g/I\!P}$. Thus a gluon density $\propto (1 - x_{g/I\!P})^5$ corresponds approximately to an $F_2^{I\!P}$ that is proportional to $(1 - x)^7$.

If the pomeron is a two quark system, and assuming that only $u\bar{u}$ and $d\bar{d}$ contribute, then the momentum sum rule is fulfilled by

$$x_{q/I\!P}\, q(x_{q/I\!P}) = \frac{6}{4} x_{q/I\!P}(1 - x_{q/I\!P}) \tag{2.42}$$

However, Donnachie and Landshoff [15] argue that the momentum sum rule need not be fulfilled. They consider diffraction as the exchange of two gluons, following [24, 25], and find that in hadron–hadron collisions the $I\!P$ has a point–like coupling to quarks, similar to a charge conjugation +1 isoscalar photon [26]. For diffractive-DIS they find that this leads to an effective structure dominated by quarks with density

$$x_{q/I\!P}\, q(x_{q/I\!P}) = \frac{1}{3} C_i \pi\, x_{q/I\!P}\, (1 - x_{q/I\!P}) \tag{2.43}$$

where $C_i \approx 0.2$ for $u(\bar{u})$ and $d(\bar{d})$ quarks, and $\approx 0.1$ for $s(\bar{s})$ quarks. Summation over the quark flavours gives a total momentum sum of $\approx 0.2$, such that the resulting $F_2^{I\!P}$ is a factor 5 smaller than that required to satisfy the momentum sum rule. Further calculations reveal an additional, gluon component $\propto (1 - x_{g/I\!P})^5$ which is dependent on $t$ and becomes significant for $x_{g/I\!P}$ less than $\sim 0.1$, generating small deviations from factorisation [27].

Genovese, Nikolaev and Zakharov [28] calculate the cross section for the process shown in figure 2.7a in which the virtual photon fluctuates into a $q\bar{q}$ pair which couple to the proton through the exchange of two gluons. In contrast to the model of Donnachie and Landshoff, the coupling of the $I\!P$ is not point–like, and the two gluons may couple to different quarks. This calculation involves the extension of the BFKL equation into the non–perturbative region, addressing both the low and high $|t|$ regions within a single framework. They find significant violations of factorisation, which can be approximated by a pomeron with two components which have a different dependencies on $x_{I\!P}$. The first amounts to a valence quark component with densities $\propto x_{q/I\!P}(1 - x_{q/I\!P})$, the second comprises quark and gluon seas arising from QCD evolution which have softer density functions. The two components are associated with effective flux factors that behave

like $\sim x_{I\!P}^{-n}$ where $n$ increases with decreasing $x_{I\!P}$ from $n \sim 1.2$ at $x_{I\!P} = 2 \cdot 10^{-2}$ to $n \sim 1.4$ at $x_{I\!P} = 2 \cdot 10^{-4}$ for the valence component, and similarly from $n \sim 1.3$ to $n \sim 1.6$ for the sea component.

Of these models, only that of Genovese, Nikolaev and Zakharov explicitly includes the effects of QCD bremsstrahlung in the generation of the parton densities. For this model, the summation of the parton densities leads to a $I\!P$ structure function which is approximately flat in $\beta$ for $\beta < 0.8$, with a very weak dependence on $Q^2$.

The effects of QCD evolution on the structure of the pomeron in the factorisable models have also been studied. It has been observed that a gluonic pomeron may be very much smaller than the proton, and as such particularly sensitive the any non–linear QCD effects, associated with gluon recombination ($gg \rightarrow g$) [29]. Considered within the BFKL formalism, such terms lead to a decrease in the effective value of $\lambda$, such that the differences between the "soft" and "hard" pomerons are reduced.

In region above $\beta = 0.8$ contributions exist from the diffractive production of light vector mesons ($\rho(770), \omega(783), \phi(1020)$) in which the virtual photon fluctuates into a meson state which scatters off the pomeron (figure 2.7d). This results in sharp resonance peaks in the $M_X$ distribution for values of $M_X$ below $\approx 4\,GeV$.

## 2.10 Photoproduction

The cross section for $ep$ falls with $Q^2$ as $\approx 1/Q^4$ such that the rate of $ep$ interactions is dominated by photoproduction processes, in which $Q^2 \sim 0$. In contrast to DIS, where most aspects of the interaction may be treated with perturbative QCD, in photoproduction such a treatment is only possible for the small subsample of events involving significant transverse momentum transfer, known as "hard". The remaining "soft" photoproduction interactions can currently only be understood using predominantly phenomenological models, such as the vector meson dominance model [30] (VMD).

It is possible for a photoproduction interaction to "fake" the signature of a

DIS electron in detector apparatus if, for example, the hadronic final state produced contains a neutral and a charged pion very close to one another. Although the probability of this happening is small, the very high rate of photoproduction interactions requires that this background be understood before a precision measurement of the DIS cross section may be made.

## 2.11 Monte Carlo Models

For any physics programme at HERA, Monte Carlo (MC) generators are indispensable. The reasons for this are twofold. Firstly, the complex effects of finite acceptance, resolution, and limited coverage in solid angle of the many different sub–detectors effectively preclude any direct analytical treatment, and must be experimentally evaluated with the aid of a simulation that reproduces the features of the data as closely as is practicable. Secondly, the presence of strongly interacting particles in the scattering processes means that the effects of the perturbatively intractable long range process of hadronisation must be unfolded from the data in order that meaningful comparisons with theoretical expectations may be performed.

### 2.11.1 Models of Standard Deep–Inelastic Scattering

For this study, two MC generators are used to simulate standard DIS processes. DJANGO [31] generates DIS events with a full treatment of electro-weak corrections to order $\alpha$. The generator is effectively an interface between two packages: HERACLES [32] and LEPTO [33]. HERACLES calculates the cross section, including the effects of higher order QED radiation, and generates the particles associated with the lepton current. LEPTO then generates the remainder of the event. DJANGO is used in conjunction with ARIADNE [34], which models the effects of gluon radiation according to the prescription of the Colour Dipole Model (CDM). To study the effect of different schemes, an alternative treatment of such higher order QCD corrections may be performed using LEPTO with "Matrix Elements + Matched Parton Showers" (MEPS), in which all the QCD corrections of $\mathcal{O}(\alpha_s)$ are included along with further parton showers such that double counting

is avoided.

It is found that while CDM provides a better description of the distribution of energy flow in the hadronic final state than the MEPS model (figure 2.8), it does not accurately reproduced the observed frequency of jet production. Though MEPS does not reproduce the energy flow as well, particularly in the forward region, it provides a better description of the jet rates [35, 36]. This is not too

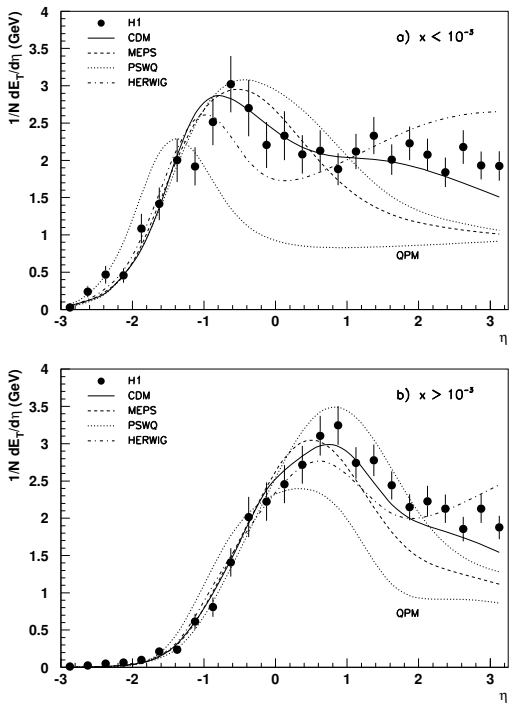


Figure 2.8: Measurements of transverse energy flow in DIS for two regions of $x$. The data are compared with several models which treat higher order QCD corrections in different ways. Two of the models, MEPS and CDM, are discussed in the text.

surprising, since $\mathcal{O}(\alpha_s)$ QCD processes (for example $\gamma^* g \rightarrow q\bar{q}$) are calculated according to the matrix element in MEPS, where as in CDM they are not explicitly included, and are only accounted for approximately by the colour dipole radiation.

For all DIS Monte Carlos the parton density functions are taken from the

recent MRS$^{H}$ parameterisations [37], which are constrained to the 1992 HERA data on the proton structure function [38, 39]. The resulting structure function is re–weighted to match the more recent measurement of $F_2$ by the H1 Collaboration [6].

### 2.11.2 Models of Diffractive Deep–Inelastic Scattering

Deep–Inelastic scattering events involving a diffractive exchange are generated using the RAPGAP program [40]. This includes complete matrix element calculations for the quark and gluon initiated subprocesses shown in figure 2.7b and 2.7c. Any pomeron structure function may be combined with any pomeron flux factor. For this study, three different pomeron parameterisations are used, referred to as Hard Quark (HQ), Hard Gluon (HG) and Soft Gluon (SG). The HQ and HG samples both use a pomeron parton density function $f(x) \propto x(1-x)$, while the SG has $f(x) \propto (1-x)^5$. All three were generated with the pomeron flux parameterisation of Streng (equation 2.37).

### 2.11.3 Photoproduction Models

The PYTHIA code is used to generate both hard and soft photoproduction events to provide an estimation of the background to the DIS sample from $\gamma p$ interactions. In addition, RAYVDM [41] was used to produce soft diffractive $\gamma p$ Monte Carlo events. Hard diffractive photoproduction was studied using POMPYT [42] with hard pomeron structure functions for quark and gluon initiated processes, as specified for the HQ and HG samples discussed above.

# Chapter 3

# The H1 Detector

## 3.1 The HERA Electron–Proton Collider

The HERA $e^{\pm}p$ collider is designed to collided 820 GeV protons with 30 GeV electrons or positrons. The different masses of the protons and leptons require two separate storage rings to achieve this. The two rings, 6.3 km in circumference, are situated in the same tunnel, and the two beams can be brought into collision at four interaction points.

The electromagnetic fields used to guide the electrons and protons around the rings focus the particles into small packets or "bunches", with about 28.8 m or 96 ns between each bunch. In 1993, the period of data taking considered in this thesis, HERA was operated with 84 colliding electron and proton bunches. Sixteen "pilot" bunches, 6 proton and 10 electron, had no colliding partners. These non–colliding bunches allow backgrounds not associated with electron–proton ($ep$) collisions to be studied. The electron ring was operated with a beam energy of 26.7 GeV, slightly below the nominal value.

## 3.2 Overview of the H1 Detector

The H1 detector is positioned around the north interaction point at HERA. The detector measures the direction, energy, and often the identity, of particles emerg-

ing from collisions at the interaction point over a solid angle of nearly $4\pi$. The angular coverage is limited mainly by the beam pipe, but also by power and readout cabling and cooling systems.

The H1 detector is shown in figure 3.1, along with the coordinate systems adopted for this thesis. The incoming proton beam defines the positive $z$ direction in the right handed set of Cartesian coordinates $(x, y, z)$. A spherical coordinate system $(r, \theta, \phi)$ is defined in the normal way with reference to the Cartesian coordinates, such that $\theta = 180^o$ corresponds to the direction of the incoming lepton–beam.

The H1 detector employs two principle methods of particle detection: tracking and calorimetric measurements. Tracking chambers measure the path taken by charged particles traversing their volume. If this path is curved due to the presence of a strong magnetic field, then measurements of momenta are possible.

Calorimeters absorb the energy of nearly all incident particles and convert it into a measurable signal. Fine segmentation in a calorimeter allows measurements of the shape, or 'profile', of the energy depositions to be made, allowing particle identification.

Tracking and calorimetry can be seen as complementary: the neutral particles undetected by the tracking chambers can be measured by calorimeters. Very low energy particles which are not well measured by the calorimeter have small radii of curvature in the magnetic field allowing a very precise momentum determination in tracking detectors. Conversely, high energy particles with straight tracks may be well measured by a calorimeter.

The design of the H1 detector addresses the following physics requirements:

- A high efficiency for electron (positron) identification and a high resolution in both energy and spatial measurements are required to study differential cross sections in deep–inelastic neutral current physics.
- In deep–inelastic charged current physics, the presence of a neutrino can only be inferred from 'missing' energy, requiring a high degree of hermeticity in addition to excellent energy resolution.

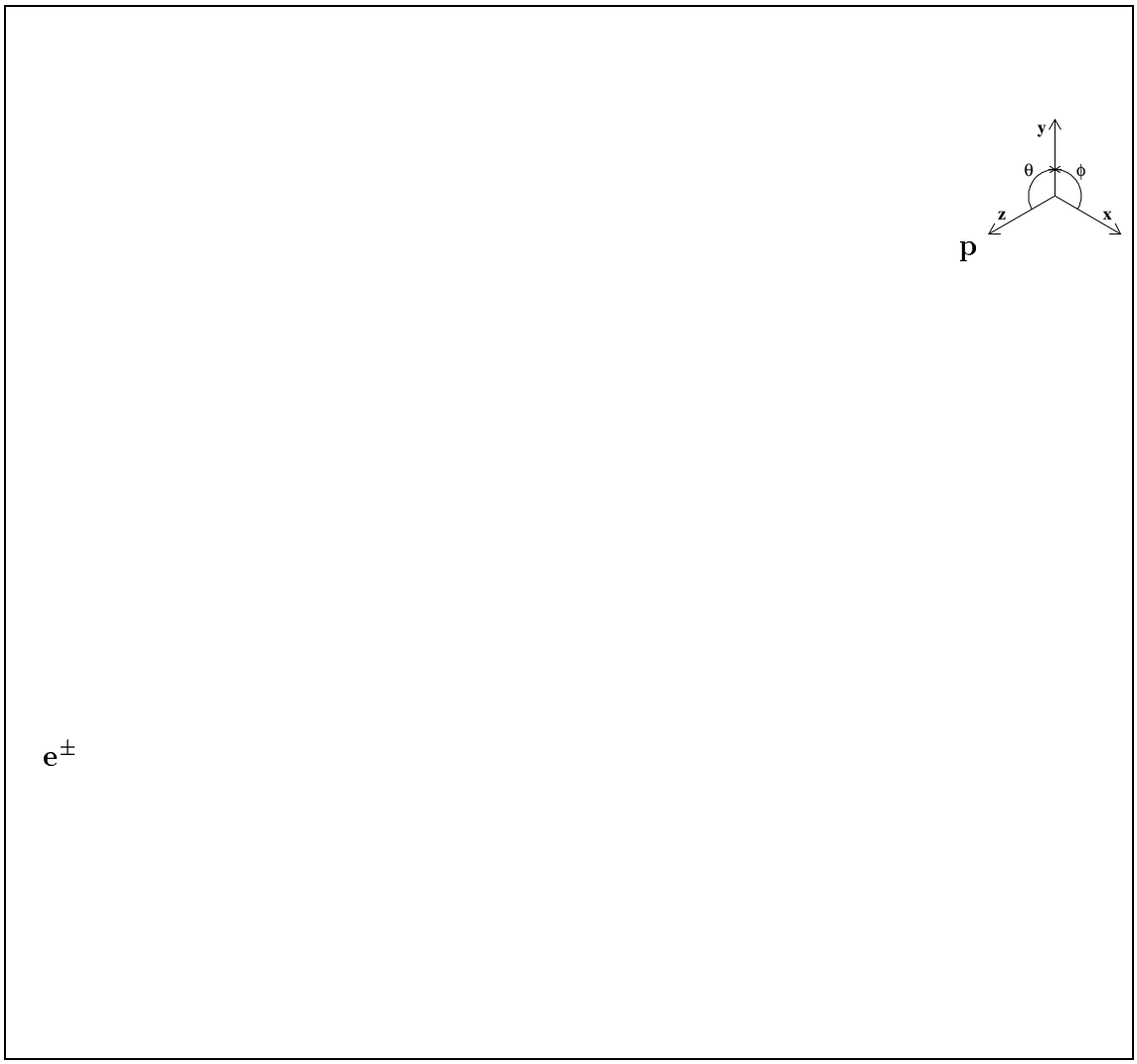


Figure 3.1: The H1 detector. The coordinate system is shown, along with the directions of the incoming beams. The size of the detector is $\sim 12\,\mathrm{m} \times 10\,\mathrm{m} \times 15\,\mathrm{m}$ and the weight $\sim 2800\,\mathrm{t}$. The proton remnant tagger ($z = 26\,\mathrm{m}$), electron tagger ($z = -33\,\mathrm{m}$) and photon tagger ($z = -103\,\mathrm{m}$) are not shown.

- Tracking is required to aid particle identification, to study charged multiplicities and energy flows, and to complement the calorimetry by accurately measuring the energy of soft charged particles.
- Muon identification is important in searches for the decay of both heavy flavour mesons as well as many exotic particles of interest at HERA.
- The high boost of the centre of mass of the collisions necessitates an asymmetric design.
- The short time interval between colliding bunches (96 $ns$) and high rates from proton induced backgrounds require sophisticated triggering. The discrimination of genuine $e$-$p$ collisions from the various background processes must occur as early as possible in the data chain to limit the dead time of the experiment.

The disparate energies of the electron and proton beams result in particle densities that are typically much larger in the forward direction ($\theta < 90^o$) than in the backward direction. Consequently the forward region of the detector contains a large number of highly segmented detectors to make accurate measurements of very high energy jets, whilst in the backward direction more emphasis is placed on electron identification. The individual detector components relevant to this analysis are described below.

## 3.3 Calorimetry

The active region of a calorimeter consists of passive layers of a dense material which causes particles passing through it to lose energy, interspersed with active layers of a sensitive sampling material in which the energy deposition produced can be measured.

When a high energy electromagnetic particle, that is an electron (positron) or a photon, passes through a thick absorber, it rapidly loses energy through bremsstrahlung and pair production. The additional particles thus created then undergo the same reactions, quickly generating a cascading 'shower' of particles,

where the number of particles initially increases exponentially with the penetration of the shower into the medium. The interaction of electromagnetic particles with matter is characterised by the radiation length, $X_0$, which is the mean distance in which a particle loses all but $\frac{1}{e}$ of it's initial energy. As the energy of the particles within the shower decreases, the main source of energy loss becomes excitation and ionisation. The energy at which the losses from bremsstrahlung and ionisation are equal is called the critical energy, $E_c$, which for electrons in lead is 6.9 MeV, and for electrons in iron is 42 MeV. As the shower develops, it spreads out laterally due to Coulomb scattering. In all materials, this spread is of the order one Moliere unit, $R_m = 21(X_0/E_c)$, where $E_c$ is in MeV. If the shower is fully contained within the calorimeter, then the initial energy of the incident particle is proportional to the amount of ionisation collected within the active regions.

When a strongly interacting particle passes though matter, both elastic and inelastic scattering between the incident particles and nucleons occurs. This results in secondary hadrons being produced, and a shower develops. The characteristic scale for the longitudinal development of such a shower is the interaction length, $\lambda_i$, which is typically much larger than $X_0$ (for lead $\lambda_I \approx 20X_0$). The development of the shower ends when the resultant hadrons are of sufficiently low energy that they are stopped by ionisation or nuclear capture. Hadronic showers typically have a larger longitudinal and transverse size than electromagnetic ones. In most calorimeters (called non-compensating calorimeters), between 20% and 30% of the energy of an incident hadron is lost through excitation or break up of nucleons. Furthermore, since a hadron will typically produce a shower containing both charged and neutral pions, the resulting shower will contain both hadronic and electromagnetic components as the neutral pions decay into photons and initiate an electromagnetic shower as described above. The difference between the response of the calorimeter for electromagnetic and hadronic particles must be compensated for, and this process is made difficult by the possibility of large fluctuations in the relative contributions from hadronic and electromagnetic components in the deposited energy.

### 3.3.1 The Liquid Argon Calorimeter

The Liquid Argon Calorimeter (LAC) [43] covers the range in polar angle between $\theta \approx 4^o$ and $\theta \approx 153^o$. It is divided into two components: the electromagnetic calorimeter (EMC) and the hadronic calorimeter (HAC). Both employ liquid argon as the sampling medium, and both are contained in a single cryostat to minimise the amount of dead material before the calorimeter.

As the shower initiated by an energetic particle entering the calorimeter develops in the absorbing material, it is periodically sampled by the layers of liquid argon. Argon atoms are ionized, and the resultant charge measured using rectangular cathode pads typically a few centimeters in size. Liquid Argon is chosen for it's high atomic density which results in an efficient production of large ionisation, and because the electrons and ions produced do not undergo further inelastic interactions (as argon is a noble gas).

The total thickness of the LAC varies in recognition of the inherent asymmetry of collisions at HERA. The EMC varies from $\approx 20X_0$ in the backward direction to $\approx 30X_0$ in the forward (proton) direction, and the thickness of the HAC varies similarly between $5\lambda_I$ and $7\lambda_I$.

The LAC is highly segmented: a total of $\approx 65000$ channels are read out. This exceptional granularity enables a highly sophisticated treatment of the problem of electronic noise. By keeping only those calorimeter cells associated with significant depositions of energy and rejecting isolated depositions of energy consistent with noise, the energy distribution of noise in "empty" events selected by random triggers is peaked at zero with $\sigma_E = 0.25\,\mathrm{GeV}$ [44]. The LAC is non-compensating: the response for hadrons is $\approx 30\%$ less than that for electrons [43]. This inequality of response is corrected for using a software re–weighting technique [45]. This technique attempts to separate those components of jets, or showers from individual hadrons, which are electromagnetic from those which are hadronic based upon the observation that electromagnetic showers are more localised than hadronic showers. The fine segmentation allows the non–compensation to be statistically corrected for by applying an energy dependent rescaling factor to the hadronic component.

Test beam measurements of LAC modules show an energy resolution consistent with $\frac{\sigma_E}{E} \approx \frac{0.12}{\sqrt{E}} \oplus 0.01$ for electrons and $\frac{\sigma_E}{E} \approx \frac{0.50}{\sqrt{E}} \oplus 0.02$ for charged pions [43, 46], where $E$ is the energy[1] in GeV. Both the resolution of the calorimeter and the overall energy scale have been verified in the H1 experiment. By comparing the measured track momentum of positrons and electrons with their corresponding energy deposition in the LAC, the electromagnetic energy scale is presently known to 3%. The absolute scale of the hadronic response has been verified to a precision of 6% by studies of transverse momentum balance in DIS events [35].

### 3.3.2 The Backward Electromagnetic Calorimeter

The Backward Electromagnetic Calorimeter (BEMC) is required to measure the energy and position of scattered electrons in low $Q^2$ ($5\,\mathrm{GeV}^2 \lesssim Q^2 \lesssim 100\,\mathrm{GeV}^2$) DIS events, and also to contribute to the measurement of the hadrons in the backward direction.

The BEMC is a lead scintillator sandwich calorimeter, covering the angular range $151^o \leq \theta \leq 177^o$ with full azimuthal acceptance. It comprises 88 stacks, 56 of which are square in cross section with a side length of 159 mm. The stacks around the outer edge of the BEMC are trapezoidal or triangular in shape, while the four innermost stacks around the beam pipe are triangular (figure 3.2). Each stack contains 50 active sampling layers of 4 mm thick scintillator interspersed with 49 layers of 2.5 mm lead. The entire structure corresponds to 22.5 radiation lengths, or 0.97 hadronic absorption lengths. The Moliere radius is 3.4 cm.

The scintillators are read out along the sides of the stacks by wavelength shifters (WLS). For the 56 'square' and 16 'trapezoidal' stacks, two pairs of 80 mm wide WLS extend along the entire active length on opposite sides. In addition, two 160 mm wide WLS cover only the last 15 active sampling layers of the remaining two sides. Each one of the wavelength shifters is assigned a separate readout channel. The distribution of the total signal from a stack between the four long WLS allows the centre of gravity of a cluster in the BEMC to be known to an

[1] Unless otherwise indicated, the units of energy are always GeV.

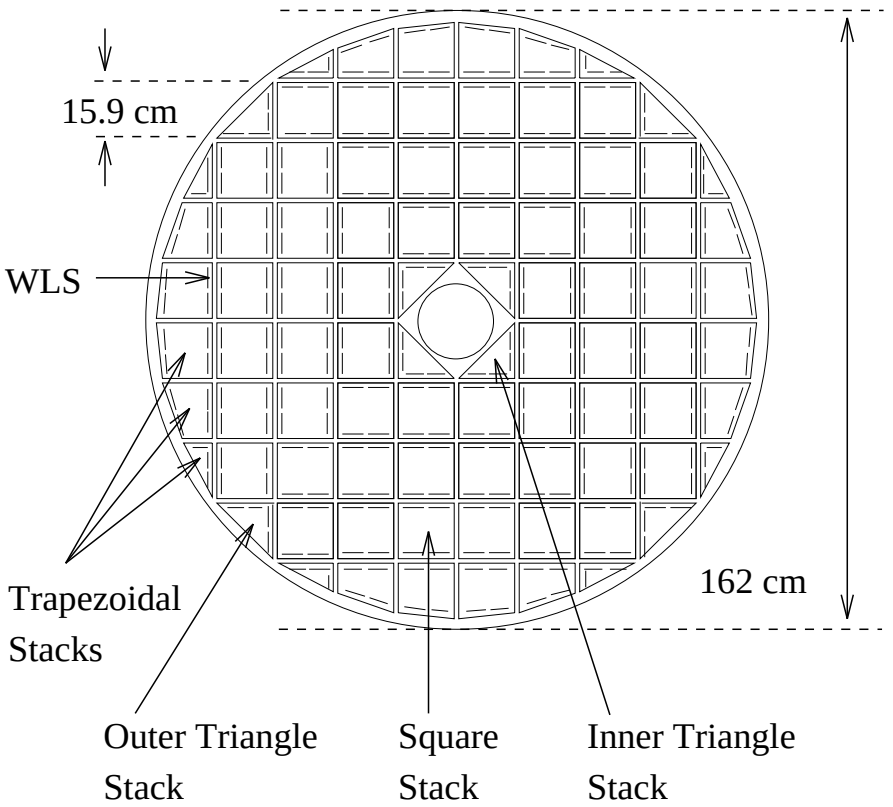


Figure 3.2: Transverse layout of the BEMC. The different types of stacks referred to in the text are shown. Also shown are the the positions of the long wavelength shifters (WLS).

accuracy of 13 mm [47]. The fraction of the total signal contained in the short WLS yields information on the longitudinal profile of the shower. Geometrical constraints lead to a slightly different arrangement of WLS for the 'triangle' stacks, which have a reduced number of readout channels. The total number of channels read out is 472.

The resolution of the BEMC in the H1 environment can be parameterised as $\frac{\sigma_E}{E} = \frac{0.42}{E} \oplus \frac{10\%}{\sqrt{E}} \oplus C$ with $E$ in units of GeV [48]. The resolution has been studied using test beams of electrons of energies ranging from 1 GeV to 80 GeV. The sampling term of $\frac{10\%}{\sqrt{E}}$ is in agreement with design expectations. The average noise in the H1 environment is found to be 140 MeV per stack, typically giving rise to 420 MeV noise per cluster, as a cluster usually contains 9 stacks. The

constant term in the energy resolution for an individual stack was found to be below 1%. Although the response of individual channels was initially equalised to better than 1%, in the 2 year period since this calibration aging effects have caused a dispersion of the calibration constants. The luminosity collected during the 1993 data taking period allowed 21 of the more central BEMC stacks to be calibrated individually. For these stacks the value of the constant $C$ was found to be between 0.03 and 0.003, depending on the statistical significance of the calibration. For the remaining stacks a global calibration was made, giving an overall systematic uncertainty in the energy scale of 1.7%[48].

The energy resolution of the BEMC for hadrons is significantly worse than that for electron (positrons) described above. Typically, hadrons entering the BEMC deposit only 30% of their energy, while 30% of all hadrons do not interact at all: their minimum ionising signal is approximately $2\sigma$ above the level of electronic noise, and remains undetected. Studies with kinematic fitting suggest consistency with an energy resolution of about $\frac{100\%}{\sqrt{E}}$, although the resolution is only loosely constrained [49].

The BEMC plays a dominant role in the triggering of low $Q^2$ DIS events. For this purpose the BEMC single electron trigger (BSET) is used to identify scattered electrons within the angular acceptance of the BEMC. In this trigger the analogue signals from each WLS are analysed to form an energy deposition in each stack associated with a particular bunch crossing. Two energy thresholds are applied to these signals. A lower threshold is set just above the noise level, while a higher threshold is used as a cluster seed. In the 1993 data taking period these levels were set at 1.0 GeV and 2.3 GeV respectively. If a stack has an energy above the higher threshold then energies from all adjacent stacks above the lower threshold are combined with the seed stack into a cluster. Trigger bits are then set dependent on the existence of a cluster above a third, still higher threshold. This cluster energy threshold was set at 4.0 GeV during 1993 [50].

### 3.3.3 The Plug Calorimeter

The Plug Calorimeter (Plug) was designed to close the forward acceptance gap between the beam pipe ($\theta \approx 0.3^o$) and the forward edge of the LAC ($\theta \approx 3^o$). By

extending the angular coverage of the calorimeter system closer to the beam pipe in the forward direction, the Plug can minimise the amount of missing transverse momentum carried by hadrons which escape undetected through the front of the detector. It can also help to veto beam-wall and beam-gas induced backgrounds.

The Plug comprises 9 layers of copper absorber interleaved with eight sampling layers of silicon. Some of the important physical parameters of the plug are given in table 3.1. The energy resolution is limited by the coarse sampling, and incomplete containment of showers. When fully operational, a resolution of $\frac{150\%}{\sqrt{E}}$ is expected [47].

| | |
|---|---|
| Position | $+476\,cm \leq z \leq +545\,cm$ |
| Overall Radius | $6 \leq r \leq 32\,cm$ |
| Radius of detector planes | $6 \leq r \leq 25\,cm$ |
| Range in polar angle | $12.5 \leq \theta \leq 58\,mrad$ |
| | $(0.71^o \leq \theta \leq 3.32^o)$ |
| Number of detectors (design) | 672 |
| Number of detectors (1993) | 504 |
| Number of read out channels (design) | 336 |
| Number of read out channels (1993) | 224 |
| Total length | $69\,cm \equiv 4.25\lambda_I \equiv 44.6X_0$ |

Table 3.1: Important physical parameters of the plug calorimeter

### 3.3.4 The Tail Catcher

In addition to muon detection, the read out pads of the muon chambers in the instrumented iron return yoke (section 3.5.1) provide an energy measurement of any hadrons that are not fully contained in the LAC or BEMC. Test beam measurements with $\pi$ and $\mu$ beams in the range 10–80 GeV demonstrated that the energy response is linear up to $\sim 40$ GeV with a resolution of $\frac{100\%}{\sqrt{E}}$ [47].

## 3.4 Tracking

A multi-wire proportional proportional chamber (MWPC) contains many anode wires spanning a gas filled chamber, with cathode wires or pads around the outside of the gas volume, and an electric potential between the anodes and cathodes. When a charged particle passes through the chamber, it ionises atoms of the gas. The ions move towards the cathodes, the electrons towards the anodes. The electrostatics within the chamber are such that the charged particle always crosses a region where the electric field is intense enough to cause rapid amplification of any initial ionisation. The rapidly approaching charge induces a signal in the sense wire, which is then amplified and recorded by subsequent electronics. The chamber is constructed such that the maximum drift distance is short, so that the signal arrives within a few tens of nanoseconds of the particle traversing the chamber. The rapid response of MWPCs make them useful for triggering.

A typical drift chamber consists of many individual cells, each cell containing a set of anode ('sense') wires separated by field wires, surrounded by cathode wires or pads. Drift chambers are designed such that the field is almost uniform across the cell. When a charged particle traverses one of the drift cells, the electrons produced by ionisation drift with a near constant velocity towards the sense wires. Only in the immediate vicinity of the sense wires does the field strength increase sufficiently to produce further ionisation, and an amplification of the signal. Since the position of the sense wire is known, the drift time can be associated with a point in space along the trajectory of the particle, known as a hit. Series of such hits recorded on successive sense wires may then be reconstructed into an estimate of that trajectory, known as a track. If the electric field is well known, then a drift chamber can give accurate spatial reconstruction over a large volume. Since at HERA the time between bunch crossings is only 96 ns, then the drift distance is restricted to no more than $\sim$ 5 to 10 cm for a typical drift velocity of $50\,\mu\mathrm{m\,ns^{-1}}$, otherwise charge deposition from too many different collisions is present in the tracking chambers. The charge deposited on the wire is proportional to the amount of initial ionisation, which is dependent on velocity of the particle. The velocity of a particle can be deduced by comparing the total charge deposited as the particle crosses the drift volume with the measured momentum ($\frac{dE}{dx}$ measurement).

Signals from the H1 drift chambers are read out using flash analogue to digital converters (FADCs) with a sampling frequency of 104 MHz. This allows the moment when the signal arrives at the sense wires to be determined to within a few nanoseconds, so that the drift distance can be measured with a resolution of $\approx 200\,\mu$m. In drift chambers where charge can be collected from either side of the plane of sense wires, the location of the original ionisation is ambiguous. The H1 drift chambers overcome this problem by staggering the sense wires with respect to the nominal centre of the chamber, such that the track appears unphysical if reconstructed on the wrong side of the plane of sense wires. By using resistive wires read out at both ends, it is possible to compare the magnitudes of the signals at each end to deduce the point along the wire at which the ionisation arrived ("charge division"). The resolution obtained using charge division is typically of the order of 1% of the sense wire length.

The H1 tracking system is shown in figure 3.3. The system is divided into

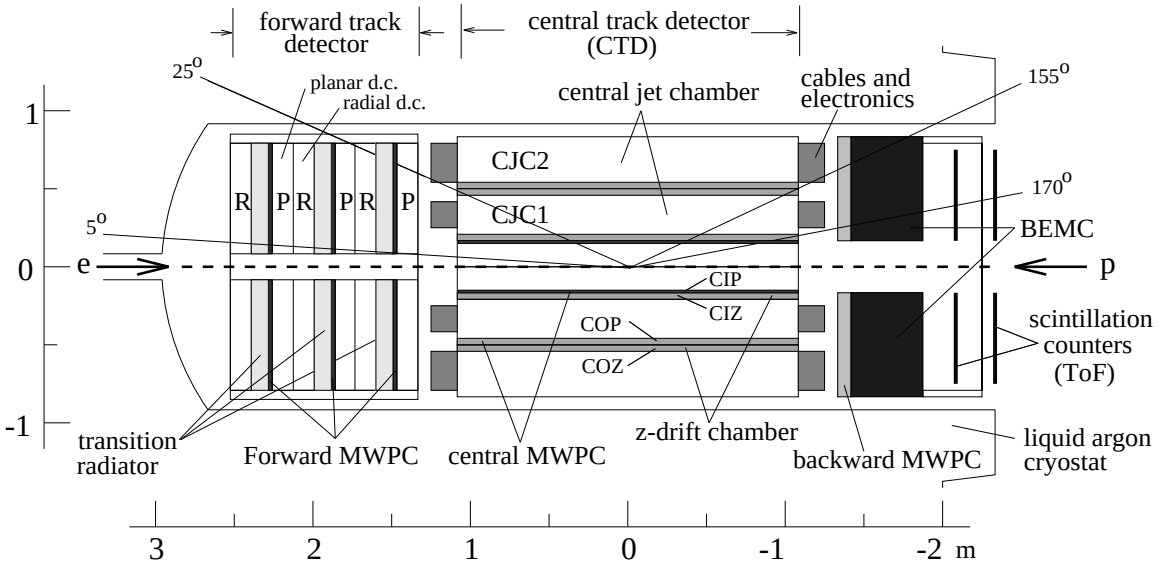


Figure 3.3: An $r$-$z$ projection of the H1 trackers

central, forward and backward regions, with the tracking detectors in each region optimised for the typical track multiplicities and trajectories in those regions.

### 3.4.1 The Forward Track Detector

The Forward Track Detector (FTD) consists of three identical super–modules, repeated in $z$. Each super–modules contains, in order of increasing $z$, a planar wire drift chamber (PWDC), a forward multi-wire proportional chamber (FMWPC), a passive transition radiator, and a radial wire drift chamber (RWDC). This arrangement can be seen in figure 3.3.

The PWDCs contains sense wires arranged in planes perpendicular to the beam axis. Each PWDC contains three sets of parallel wires, each set rotated by $60^o$ with respect to one another. The drift cells are $\approx 56\,\mathrm{mm}$ wide. The wires are only read out at one end, so coincidences in all three sets of wires are required to resolve ambiguities. The FMWPCs are read out by cathode pads to provide a fast trigger signal from the forward region. When a relativistic particle crosses a boundary between media with two different dielectric constants, there is a small probability that it will emit a transition radiation (TR) photon. The passive transition radiators are designed to maximise this probability allowing discrimination between electrons and hadrons. The angle of emission of the TR photons is small, and so the existence of TR photons is seen as an increase in the amount of charge deposition in the RWDCs. The sense wires in the RWDCs are strung radially, with the maximum drift distance varying between 10 mm and 50 mm at the inner and outer radii of the chambers respectively. The wires are read out at both ends, allowing a spatial point to be reconstructed from each signal. Track segments can be reconstructed in the radial chambers and linked to any found in the planar chambers to give tracks through the whole forward tracker. These tracks can be linked to tracks in the central tracking detector (section 3.4.2) to give complete tracking back to the track vertex. In addition to TR detection, $\frac{dE}{dx}$ measurements can also be used for particle identification.

### 3.4.2 The Central Tracking Detector

The main components of the Central Tracking Detector (CTD) are the Central Drift Chambers (CJC1 and CJC2), which are arranged concentrically around the beam pipe. Both have planes of sense wires running parallel to the beam axis,

with the different drift regions defined by planes of cathode wires. Each drift cell is inclined by $30^o$ with respect to the radial direction such that a stiff track from the interaction region always passes through more than one drift cell. This helps to resolve track reconstruction ambiguities as track segments must be connected across different cells. In addition, it is possible to use the exact matching of the track segments at the drift cell boundaries to determine the passing time of the particle to an accuracy of $\approx 0.5\,\mathrm{ns}$, allowing tracks to be assigned to the correct bunch crossing. Drift time and charge division measurements determine the $r-\phi$ and $z$ coordinates respectively, with resolutions of $\sigma_{r-\phi} \approx 350\,\mu\mathrm{m}$ and $\sigma_z \approx 5\,\mathrm{cm}$ [47].

To enhance the resolution of the $z$ measurements of tracks in the central regions, there are two smaller drift chambers with 4 layers of sense wires strung around the beam axis in the $r-\phi$ plane. The Central Inner $Z$ Chamber (CIZ) is situated immediately inside the CJC1, and the Central Outer $Z$ Chamber between CJC1 and CJC2. In these chambers the $r-\phi$ measurement comes from charge division, while the $z$ measurement comes from the drift time with a resolution of $\sigma_z \approx 200 - 500\,\mu\mathrm{m}$ [47].

The CTD contains two MWPCs for triggering on tracks emanating from the interaction point, the Central Inner and Outer Proportional Chambers (CIP and COP). The CIP is located between the beam pipe and the CIZ, while the COP is positioned between the CJC2 and the COZ. Both the CIP and COP contain two concentric chambers which are read out by cathode pads, where the different layers are staggered in $\phi$ to increase the effective resolution. The arrangement of the different components of the CTD is shown in figure 3.4.

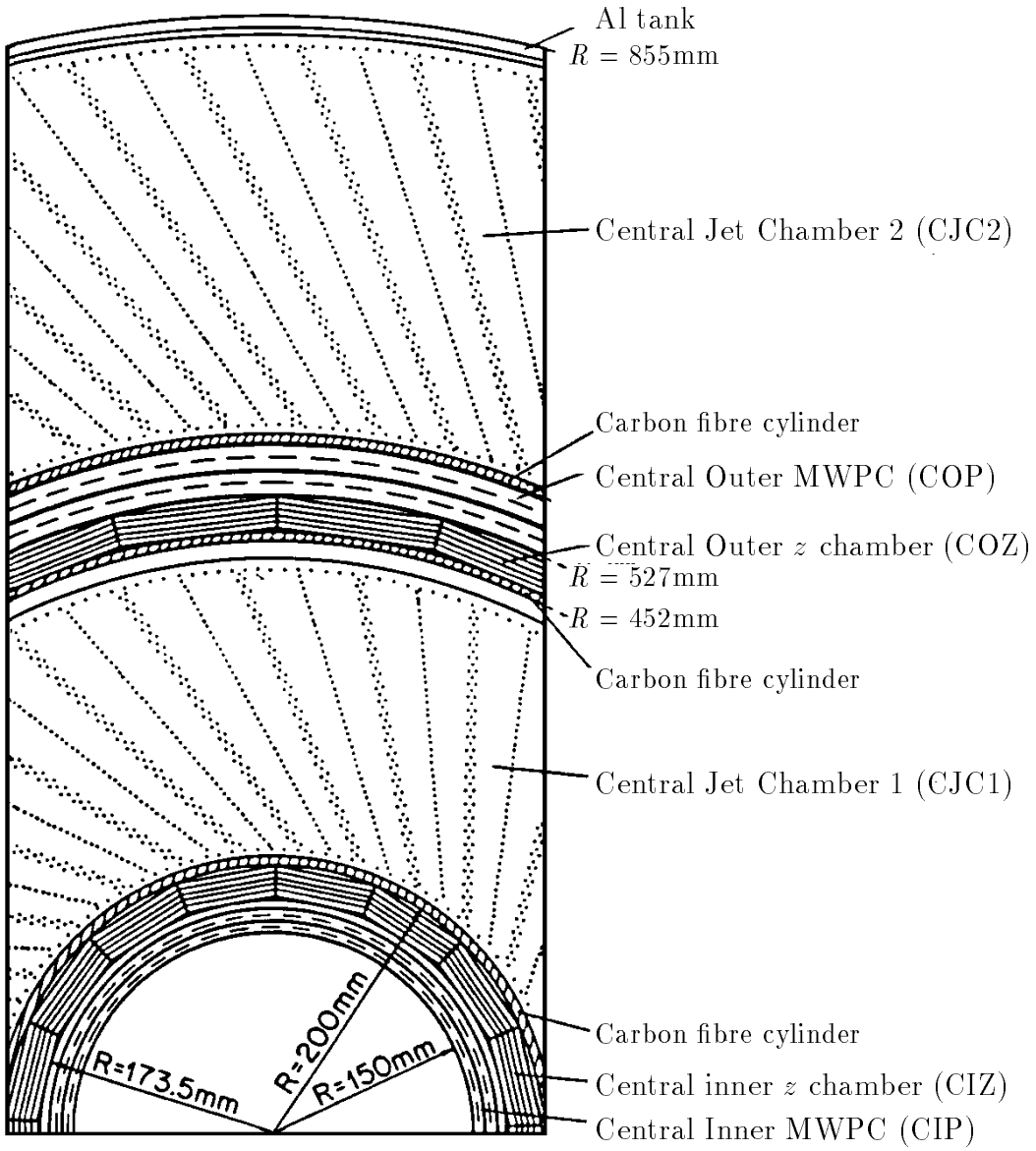


Figure 3.4: A section through the central track detector, perpendicular to the beam. The wires in the CJC are parallel to the beam axis and the drift cells are tilted at an angle of $30^o$ to the radial direction.

### 3.4.3 The Backward Multi-wire Proportional Chamber

For angles greater than $\approx 154^o$, the ability of the CTD to accurately reconstruct tracks becomes increasingly limited. The Backward Multi-wire Proportional Chamber (BPC) not only provides fast triggering information, but also gives accurate spatial information on charged particles traveling in the backward direction. This is achieved by read out of the anode wires instead of the cathode pads. The BPC contains four planes of anode wires, each rotated by $45^o$ with respect to the previous layer, allowing accurate spatial reconstruction from coincidences between signals from the different layers. The active region extends from an inner radius of 135 mm to 650 mm, corresponding to an angular coverage of $155^o \leq \theta \leq 174.5^o$. The spatial resolution of the chamber is $\sigma_{x,y} \approx 1\,\mathrm{mm}$, which corresponds to a resolution of $\sigma_\theta \approx 0.5\,\mathrm{mrad}$ for a particle from the nominal interaction point. The resolution is of the same order of magnitude as the limit imposed by multiple scattering in material in front of the chamber. By studying events containing well reconstructed tracks pointing toward the BEMC, the systematic uncertainty in the angular measurement from the BEMC has been verified to be within 2 mrad [6].

## 3.5 Muon Detection

As has already been mentioned (section 3.3.4) the return yoke for the main H1 magnet is instrumented with limited streamer tubes (LSTs). In addition to acting as a tail catcher for the Liquid Argon Calorimeter and the BEMC, the iron instrumentation allows the detection and tracking of penetrating muons.

The kinematics of collisions at HERA result in event topologies containing a higher average momentum for muons produced in the forward direction than for those produced more centrally, along with a higher density of background tracks. For muons to be unambiguously identified in the forward direction, the instrumented iron detection is augmented by the Forward Muon Detector (FMD), which covers the angular range $3^o \leq \theta \leq 17^o$.

### 3.5.1 The Instrumented Iron

The instrumented iron is divided into three sections: the central barrel region, and the forward and backward end caps. Each is divided symmetrically about a vertical plane passing through the beam axis. Layers of LSTs are interleaved with the layers of iron in each section. The cross section of each LST is a 10 mm $\times$ 10 mm square. A single wire, at ground potential, is constrained to lie along the centre of each tube. Three of the sides of each tube are coated with a low resistivity graphite paint to which a high voltage is applied. The fourth side is coated with a paint of a much higher resistivity, to which readout strips or pads are attached, depending on the location of the LST within the return yoke. In addition, the wires along the centre of each LST are also read out.

### 3.5.2 The Forward Muon Detector

The Forward Muon Detector (FMD) is situated outside the iron return yoke, in front of the main body of the detector, in the region $6.4\,\mathrm{m} \leq z \leq 9.4\,\mathrm{m}$. It comprises 6 layers of drift cells, three on either side a toroidal magnet which deflects charged particles in $\theta$. The drift cells are 20 mm deep and 120 mm wide, and contain single sense wires running down the centre of each. Spatial measurements from drift time and charge division give resolutions of $\approx 250\,\mu\mathrm{m}$ and $2 - 6\,\mathrm{cm}$ respectively. This large inequality in the resolution from the two spatial measurements leads to two distinct arrangements of drift cells within a layer. Four layers contain cells arranged so as to give a better measurement of the radial coordinate, and are known as $\theta$-layers. The remaining two layers, the $\phi$-layers, give a better measurement of the azimuthal coordinate. On each side of the toroidal magnet there is one $\phi$-layer sandwiched between two $\theta$-layers.

The FMD gives an independent momentum measurement for muons with momenta in the range $5 \leq p \leq 200\,\mathrm{GeV}$, but is optimally used to identify the track left by the muon in the FTD (section 3.4.1) where a more accurate momentum measurement can be made.

## 3.6 Scintillation Walls

At H1, the rate of genuine electron-proton collisions is considerably smaller than the rate of proton beam induced background events by which they can be mimicked. To distinguish between the two, fast scintillator based detectors are used to correlate the timing of particles from the collision with the nominal time of the bunch crossing.

### 3.6.1 The Time of Flight System

The Time of Flight system (ToF) consists of two planes of scintillator situated at $z \approx -2\,\mathrm{m}$. They are of approximately the same area as the BEMC (section 3.3.2), behind which they are situated, and measure the time of passing of charged particles with a resolution of $\approx 4\,\mathrm{ns}$. The inner layer, that is the layer nearest to the interaction region, is divided into 16 individual counters, the outer layer into 8. This limited spatial resolution allows signals in the ToF to be correlated with those in the BEMC. To protect them from synchrotron radiation from the electron beam, each layer is sandwiched between 6.5 mm sheets of lead. In addition, the inner sections of each layer can be moved away from the beam line mechanically.

A particle which originates from a proton beam-wall or proton beam-gas collision upstream from H1 will enter the ToF system at about the same time as the proton bunch itself. However, a particle from a genuine $ep$ collision will enter ToF $\approx \frac{2\Delta z}{c}$ later, where $\Delta z$ is the distance that the collision occurs in front of the ToF. For collisions at the nominal interaction point, this is a difference of about 13 ns, which corresponds roughly to the time at which the electron beam passes through the ToF, although there is some variation in the time of arrival due to the length of the proton bunch of $2 - 3\,\mathrm{ns}$. Signals in the ToF are categorised as belonging to one or more of three time windows with respect to the nominal bunch crossing time. One window, called the "global" window, is intended to contain all signals associated with a single bunch crossing, and so is $\sim 96\,\mathrm{ns}$ in length. A second window, the 'background' window, is positioned around the expected time of arrival of the proton bunch at the ToF with a size of $\approx 25\,\mathrm{ns}$. The interaction window, that is the time period during which particles from a

genuine $ep$ collision are expected to arrive at the ToF immediately follows the background window, and is 13 ns long. Synchrotron radiation from the electron beam is also expected to arrive at the ToF during the interaction window.

### 3.6.2 The Veto Walls

Further upstream from the ToF system, at $z = -6.5\,\mathrm{m}$ and $z = -8.1\,\mathrm{m}$ are two considerably larger planes of scintillation counters, the veto walls. They cover the same area as the rear face of the LAC (section 3.3.1). The outer wall ($z = -8.1\,\mathrm{m}$) has a timing resolution of $\sim 8\,\mathrm{ns}$, the inner wall one of 3 ns, and they work on the same principle as the ToF system, providing a tool to monitor and reject proton beam induced backgrounds.

## 3.7 The Electron and Photon Taggers

The H1 luminosity system, shown in figure 3.5, consists of two Čerenkov calorimeters: the photon detector (PD) situated at $z \approx -100\,\mathrm{m}$ and the electron tagger (ET) at $z \approx -33\,\mathrm{m}$, both of which sit very close to the beam line. The luminosity is calculated by measuring the rate of the Bremsstrahlung interaction[2] $ep \to ep\gamma$. The acceptance of the two detectors allows the study of the rate of this interaction, in which the structure of the proton is not resolved and the cross section is very precisely known, at $Q^2$ less than $\sim 0.01\,\mathrm{GeV}^2$. Provided that the acceptance is also well known, this measurement can be translated into an accurate measure of the luminosity.

Each detector consists of an array of crystals, each crystal square in cross section with a depth of 200 mm, or $\approx 22X_0$. The PD is a $5 \times 5$ array with a transverse size of $100\,\mathrm{mm} \times 100\,\mathrm{mm}$, the ET a $7 \times 7$ array of size $154\,\mathrm{mm} \times 154\,\mathrm{mm}$. The positional resolution achieved is better than 1 mm, and the energy resolution is $\frac{\sigma_E}{E} = \frac{10\%}{\sqrt{E}} \oplus 1\%$ [47].

The backgrounds to the Bremsstrahlung process used in the luminosity mea-

[2]Such interactions are often called Bethe-Heitler events.

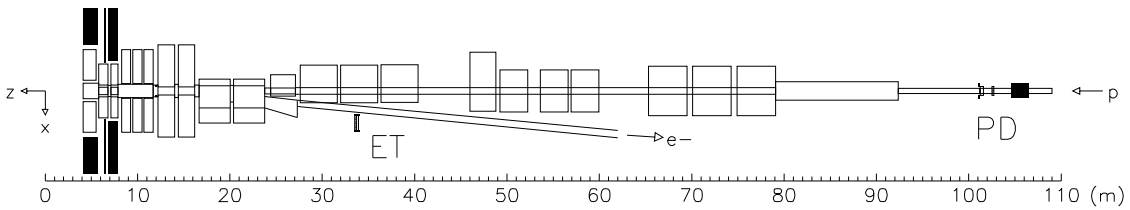


Figure 3.5: The H1 luminosity system

surement are the interaction of the electron beam with residual gas particles ($e$ beam-gas background), synchrotron radiation, and proton beam halo. To protect the PD from proton beam induced backgrounds there is a 2 m thick lead wall further upstream along the proton beam line. A lead sheet, approximately $2X_0$ thick, protects it from synchrotron radiation. A water Čerenkov counter, of thickness $\approx 1X_0$, between the PD and the lead sheet is used to veto events in which the Bremsstrahlung photon interacted with the sheet of lead. The contribution from $e$ beam-gas background is calculated using the rate of events in pilot bunch crossings (see section 3.1).

The biggest uncertainty in the luminosity calculation is the acceptance, for which a systematic uncertainty of 5.5% was estimated for the 1993 running period [6]. It has been estimated that the current systematic uncertainty on the luminosity of 7% can be reduced to 5% in the future [47].

## 3.8 The Proton Remnant Tagger

The forward proton tagger ($\mathrm{P_{TAG}}$) consists of two layers, each composed of scintillator sheets sandwiched by lead shielding. It is situated 24 m from the interaction point in the proton direction, and the scintillator sheets cover an area of about $60 \times 60\,\mathrm{cm}^2$ transverse to and around the beam pipes. The resulting coverage in rapidity is $5.8 < \eta < 8$.

## 3.9 Triggering and Data Acquisition

The time interval between successive bunch crossings at HERA is 96 ns, whereas the time taken to read out all of the information from all of the sub–detectors is $\approx$ 1 ms, and during this time the detector is "dead", that is not able to take further data. The task of the triggering system is to reconcile these two disparate time scales by making a fast decision, based upon a limited amount of information, about whether an event is interesting or not, thus minimising the time during which the detector is not sensitive, called the "dead time".

The task of the trigger is complicated by the fact that it takes a time equivalent to $\sim$ 24 bunch crossings for the triggering information from each sub–detectors to be delivered to the central trigger logic. To avoid having to wait for this time after every bunch crossing to make a decision on whether an interesting interaction occurred, information from each sub–detector is "pipe-lined". Pipe-lining is the storage of information from each sub–detector over many successive bunch crossings in a buffer, such that all bunch crossings can be analysed. The exact method used to pipe-line the information from each sub–detector is different, with information from between 27 and 35 successive bunch crossings stored in each.

The triggering system is divided into four distinct levels. The first level trigger (L1) combines the individual trigger elements into sub–triggers, of which there can be up to 128. Sub–triggers designed to identify physics events, that is those which can be associated with genuine $e$-$p$ collisions, generally combine background rejection elements (such as the ToF veto - section 3.6.1) and physics selection elements (such as the BSET element 3.3.2.) In addition, sub–triggers to identify cosmic events and to monitor background levels and triggering efficiencies are also constructed.

If any one of the sub–trigger conditions is satisfied, a signal is sent to "freeze" the pipe-lines (call an L1Keep), and all the information in the pipe-lines from the sub–detector begins to be read out by the data acquisition system (DAQ). Each sub–detector compresses the data and sends it along a fiber–optic ring to the central data acquisition system (CDAQ). The DAQ is based on the VMEbus system [51] and full details can be found in [52]. It is during this time that the level

2 and 3 triggers are designed to operate. Each of these triggers analyses only the same data as available at level 1, but with increasing degrees of sophistication. If either level 2 or 3 decides to reject the event, then the read out process is stopped and the pipe-lines are re-enabled, thus limiting the dead time. Although these two levels were not commissioned for the 1992 and 1993 running periods, the L1 trigger was able to be optimised such that the rate of accepted events was constrained to less than $\sim 60\,\mathrm{Hz}$, corresponding to $\sim 0.6\,\mathrm{Mb\,s^{-1}}$, a level which resulted in acceptable dead–times of $\sim 10 - 15\%$.

Once the readout process is complete, the CDAQ "builds" the event, decompressing all of the information it received, and sends it to the level 4 trigger, often referred to as the L4 Farm. The L4 Farm consists of an array of fast parallel RISC processors which execute a fast, specialised version of the reconstruction code. Events are filtered through a sophisticated suite of background rejection algorithms, including ones that reject, for example, collisions which originated upstream from the nominal interaction region.

Once the L4 Farm receives an event, it operates independently of the preceding trigger stages enabling data taking to proceed while background rejection is performed. The unreconstructed data from those events which were not rejected, along with those from 1% of the rejected events which are kept for monitoring purposes, are sent to the central DESY mainframe computer for permanent storage.

During 1993 the L4 Farm reduced the event rate from $\sim 60\,\mathrm{Hz}$ after L1 to $5 - 10\,\mathrm{Hz}$.

## 3.10 Simulation of the H1 Detector

All Monte Carlo data used in this thesis are passed through a detailed simulation of the H1 detector, H1SIM [53]. For the photoproduction Monte Carlo data, the simulation procedure is optimized to increase the statistics available for background studies. Only those generated particles with polar angles greater than $156^o$ were passed to H1SIM. Only if, after the simulation and reconstruction of

this component of the event, the event contained an electron candidate with cluster energy greater than 7 GeV and a reconstructed BPC hit within 15 $cm$ of the cluster, was the whole event passed through the simulation and reconstruction. With this method [60], only 1 to 5% of photoproduction events require full simulation, enabling sufficient statistics to be generated such that the resulting data samples correspond to between 1 and 7 times the luminosity of the 1993 data.

# Chapter 4

# Event Selection

## 4.1 The Data Sample

The data analysed in this thesis were collected during the period June-October 1993. Only data taken during periods when the BEMC, BPC, CJC, LAC, and ToF (sections 3.3.2, 3.4.3, 3.4.2, 3.3.1 and 3.6.1 respectively) were fully operational are considered. During 1993 the HERA machine delivered $\sim 1\,\mathrm{pb}^{-1}$ of luminosity, of which $\sim 0.6\,\mathrm{pb}^{-1}$ was collected by the H1 experiment. A combination of on–line monitoring and careful subsequent off–line selection give a final data sample of $(271 \pm 14)\,\mathrm{nb}^{-1}$ for which the detector was known to be operating effectively for low $Q^2$ electron analysis [55].

## 4.2 H1 Data Collection, Reconstruction and Classification

Those data selected by the trigger described in section 3.9 are stored, unreconstructed, on magnetic tapes. Reconstruction involves the conversion of these "raw" data into information useful for physics analysis: particle trajectories and associated momentum measurements are extracted from many individual signals from the trackers, and calorimeter data are converted into estimations of deposited energy. After reconstruction, the data are classified by L5, the fifth level

trigger, which consists of selection procedures developed by individual physics working groups to select events for further analysis. Events can be flagged as belonging to one or more "classes", that is as having been selected by one or more of the classification algorithms. All the events belonging to one or more of the L5 classes, along with the classification information, are stored permanently on POT or "Physics On Tape"[1] cartridges. The POT selection criteria are deliberately loose such that refinements of the reconstruction code usually require only those data on POT to be reprocessed.

Despite the reduction in the number of events stored in the POT sample from the total contained in the raw data, the reduction in total data volume is not significant due to the increased size of each event from the additional information associated with the reconstruction[2]. Consequently further reduction is necessary to facilitate fast access for analysis. A second selection with more stringent requirements produces the data summary tapes (DST). For most data classes the reduction achieved allows storage on disk, with referral back to the larger data samples on cartridge unnecessary for all but a few specialised analysis tasks.

## 4.3 Kinematic Reconstruction

At fixed target experiments, only the scattered lepton is usually available for the reconstruction of the kinematic variables. At H1, however, both the scattered electron and the hadronic system are well measured. This permits the reconstruction of the kinematics of an $ep$ collision from the momentum of either the scattered lepton, the hadronic system, or a combination of both. As the kinematics are thus over constrained, the systematic uncertainties associated with their reconstruction may be studied, quantified and controlled by the application of several independent methods of calculating $x$, $y$ and $Q^2$.

In terms of the variable of the scattered lepton, the kinematics are obtained by recasting equations 2.2, 2.6 and 2.7 in terms of the lepton momentum mea-

[1] Called "Production Output Tapes" at some experiments.

[2] The 1993 data sample resides on $\sim$ 2500 raw data cartridges, which reduces to $\sim$ 2000 POT cartridges.

surement in the laboratory frame such that

$$Q_e^2 = 4EE'\cos^2\frac{\theta_e}{2} \tag{4.1}$$

$$y_e = 1 - \frac{E'}{E}\sin^2\frac{\theta_e}{2} \tag{4.2}$$

and

$$x_e = \frac{Q_e^2}{sy_e} \tag{4.3}$$

where $E$ is the incident electron energy, $E'$ the scattered electron energy, $\theta_e$ the angle of the scattered electron in the H1 coordinate system, and $\sqrt{s}$ the centre of mass energy (equation 2.10). This measurement of the kinematics based entirely on the electron momentum, the "electron only" method, gives an excellent resolution in the determination of $Q^2$, which is always $\approx 5\%$ for the region $7.5 \leq Q^2 \leq 80\,\mathrm{GeV}^2$ considered here. The resolution for $y$ is also good at high $y$, but degrades rapidly as $y \to 0$ due to the term $\propto 1/y$ in the error propagation of $y$:

$$\frac{\delta y}{y} = \frac{1-y}{y}\left(\frac{\delta E'}{E'} \oplus \frac{\delta\theta}{\tan\frac{\theta}{2}}\right) \tag{4.4}$$

giving poor resolution at low $y$, or high $x$.

When reconstructing the kinematics from the hadronic system, cognisance must be taken of the inevitable loss of some particles due to incomplete coverage in solid angle. In collisions at HERA, much of the target jet, that is the remnant of the proton, is lost in the beam pipe in the forward direction. In addition, it is often impossible to unambiguously assign particles as belonging to either the target or current jet. To overcome these problems, the method of Jacquet and Blondel [56] may be used, in which the kinematics are calculated from

$$y_{jb} = \frac{1}{2E}\sum_i (E^i - P_Z^i) = \frac{\Sigma}{2E} \tag{4.5}$$

$$Q^2_{jb} = \frac{1}{1-y}\left(\left(\sum_i P_X^i\right)^2 + \left(\sum_i P_Y^i\right)^2\right) \tag{4.6}$$

where the summation is over all of the final state particles, excluding the scattered electron. Note that the effect due to losses in the forward direction are minimised, since for particles with $\theta \sim 0$, both $E - P_Z$ and transverse momentum are small. This method gives better resolution in $y$ at low $y$, but becomes significantly worse

than the electron only method at high $y$ (figure 4.1)because of losses of particles in the backward direction, which contribute maximally to $E - P_Z$. The resolution of $Q^2_{jb}$ is always worse than that offered by the electron only method.

The $\Sigma$ method combines the measurements from the scattered electron with those from the remaining final state in a way that not only improves upon the determination of $y$ from the Jacquet–Blondel method at high $y$, but also dramatically reduces the effects of initial state radiation. In this method, the term in the denominator of equation 4.5 is replaced by one that admits the possibility of initial state radiation. In the case of the initial state radiation of a photon, of energy $E_\gamma$, collinear with the incident electron, the conservation of energy and longitudinal momentum lead to

$$2E = \sum_{all}(E - P_Z) = \Sigma + E'(1 - \cos\frac{\theta_e}{2}) + 2E_\gamma \tag{4.7}$$

where $\Sigma$ is as defined in equation 4.5. Therefore, in order to arrive at the true $y$ at the hadron vertex, the term $2E$ in equation 4.5 must be replaced by

$$2E \rightarrow 2E_\Sigma = \Sigma + E'(1 - \cos\frac{\theta_e}{2}) \tag{4.8}$$

in recognition of the reduction in the centre of mass energy of the collision, such that

$$y_\Sigma = \frac{\Sigma}{\Sigma + E'(1 - \cos\frac{\theta_e}{2})} \tag{4.9}$$

Replacing $E$ by $E_\Sigma$ in equation 4.1 gives an expression for $Q^2$

$$Q^2_\Sigma = \frac{E'^2 \sin^2\theta_e}{1 - y_\Sigma} \tag{4.10}$$

which is also independent of initial state radiation. Combining $y_\Sigma$ and $Q^2_\Sigma$ using the nominal centre of mass energy

$$x_\Sigma = \frac{Q^2_\Sigma}{s y_\Sigma} \tag{4.11}$$

completes the $\Sigma$ prescription.

The $y$ resolution of this method is good even at low $y$ (figure 4.1) as $y$ no longer appears in the denominator:

$$\frac{\delta y}{y} = (1 - y)\left(\frac{\delta\Sigma}{\Sigma} \oplus \frac{\delta E}{E} \oplus \frac{\delta\theta}{\tan\frac{\theta}{2}}\right) \tag{4.12}$$

It should be noted that although $x_\Sigma$ is affected less dramatically by initial state radiation than $x_{el}$, the corrections are still non–zero as $x_\Sigma$ is constructed using the nominal centre of mass energy. A review of all of the reconstruction methods mentioned here, including a full discussion of the $\Sigma$ method, may be found elsewhere [57].

The resolutions of the determination of $y$ by the electron, Jacquet–Blondel and $\Sigma$ methods are compared in figure 4.1. The poor resolution of the electron

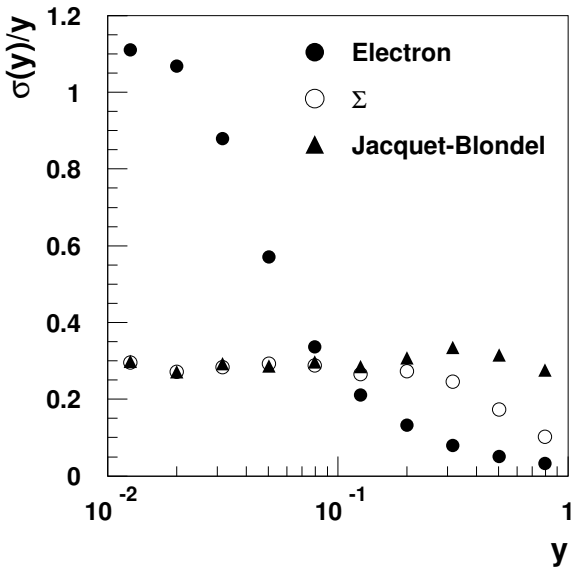


Figure 4.1: The resolution of the electron, Jacquet–Blondel and $\Sigma$ reconstruction methods for Monte Carlo events after simulation and reconstruction.

method at low $y$ and the large radiative corrections, which approach $\approx 20\%$ at high $y$, restrict it's applicability to $0.05 < y_e < 0.6$ [58]. The resolution of the $\Sigma$ method limits the use of this reconstruction method to $0.01 < y_\Sigma < 0.7$ [59].

## 4.4 The Selection of Deep–Inelastic Scattering Events

The analysis presented here is based upon a sample of neutral current deep–inelastic scattering data (section 2.2) in the range $7.5 \leq Q^2 \leq 80\,\mathrm{GeV}^2$. Such

data are characterised by an energetic electron scattered into the backward part of the H1 detector, which is covered by the BEMC. Consequently the identification of electrons scattered into the BEMC, and the rejection of backgrounds which produce "fake" candidate electrons in the BEMC, is central to the selection of the data.

Electrons candidates are identified by searching for electromagnetic (EM) clusters in the BEMC. EM clusters tend to exhibit less lateral dispersion, and to penetrate less deeply into the calorimeter than hadronic clusters, allowing the possibility of distinguishing between the two if the calorimeter is sufficiently segmented. Associating tracking information with energy deposition in the calorimeters allows discrimination between energy depositions associated with neutral and charged particles. For the $Q^2$ range considered here, if $y < 0.7$ then the electron is expected to be the most energetic particle entering the BEMC as even if the current jet is in the backward direction, the energy is typically shared between many hadrons[3].

The processes capable of producing spurious electron candidates, or "background" processes, include photoproduction interactions (section 2.10), and collisions of beam particles with either residue gas particles ("beam–gas"), or the beam-pipe material ("beam–wall").

In a photoproduction interaction, the electron is scattered at $\theta \approx 180^o$ and remains in the beam pipe, undetected in the BEMC calorimetry[4]. Energy and momentum conservation require the remainder of the event to have a higher total longitudinal momentum than a DIS event, such that the probability of a highly energetic particle being produced in the backward direction is expected to fall rapidly with increasing energy. However, the cross section for $ep$ scattering rises rapidly because $Q^2$ decreases as $\sigma(ep \rightarrow eX) \propto \frac{1}{Q^4}$, and so the rate of photoproduction events is orders of magnitude higher than that for neutral current DIS. Consequently, if even a small fraction of photoproduction events produce electron candidates, then the contamination of the candidate DIS events can be

[3]The errors caused by the incorrect identification of the scattered electron were studied, and found to be inconsequential in comparison with those associated with finite resolution and background processes.

[4]Recall that at HERA the proton direction is define to be the positive $z$ axis, or $\theta = 0^o$, and so the direction of incident electron is $\theta = 180^o$.

significant. In proton beam–gas events, the centre of mass is highly boosted in the proton beam direction, such that, as for photoproduction, the probability of producing an electron candidate is expected to decrease rapidly with increasing energy. It is possible, however, for a proton beam–gas collision upstream from the interaction region to produce an energetic hadron which enters the BEMC from the rear, producing a significant energy deposition. The overwhelming majority of such events are vetoed by the ToF device (section 3.6.1), and even if they are not, then it is unlikely that they will produce a track pointing towards the interaction region. The rate of electron beam–gas interaction should, as for $ep$ beam–beam collisions, be dominated by photoproduction off an effectively stationary proton. Since the centre of mass energy of such a collision is much smaller than that for an $ep$ beam–beam collision, it is less likely to produce an electron candidate. Beam–wall collisions exhibit signatures that are similar to beam–gas collisions since they occur with similar centre of mass energies.

### 4.4.1 On–line Selection

The basis of the selection of low $Q^2$ neutral current DIS events is the BSET trigger (section 3.3.2). The rate of this trigger is dominated by "single diode" events, in which synchrotron radiation from the electron beam enters the BEMC from the rear and interacts with a wavelength shifter. The majority of which are removed by the L4 Farm, as discussed later in section 4.4.5. The remaining data sample is dominated by beam–wall, beam–gas and photoproduction interactions described above. The two L5 event classes associated with the selection of low $Q^2$ DIS events, known as NCHAD and NCLQSQ, must satisfy the following requirements:

1. The efficiency of the selection for low $Q^2$ DIS events must be high.
2. The selection must reduce the dominant contribution to the rate of the BSET trigger from background processes, while still satisfying the previous requirement.
3. The efficiencies of the selection for the retention of the signal, and the rejection of the backgrounds, must be calculable.

To allow calculations of the efficiencies of the selection to be made, considerable overlap is explicit in the definitions the two L5 classes. The NCHAD selection is based upon the existence of an EM cluster in the BEMC, and a charged track emanating from the beam axis (a "vertex"). The NCLQSQ selection requires an EM cluster in the BEMC that exhibits characteristics consistent with an electron or positron. The classes are defined for both the POT and DST selection stages, with increasing levels of stringency for the reasons discussed in section 4.2.

### 4.4.2 POT Selection

For the POT selection, the NCHAD class requires the following:

1. a BEMC cluster with energy $E' \geq 4\,\mathrm{GeV}$
2. a reconstructed vertex

Here, a reconstructed vertex is a point along the beam line to which one or more of the tracks in the event can be extrapolated. Information on the average position of the interaction point in the $r$-$\phi$ plane is extracted continually from tracking information during the data taking to produce a frequently updated nominal interaction position in $r$-$\phi$, which is stored in a database for future reference. In the subsequent reconstruction, a series of attempts are made to constrain each track in the CTD and FTD to this point in the $r$-$\phi$ plane. The $z$ coordinate obtained from the fit is referred to as the "$z$-vertex" of the event. If two or more tracks can be thus constrained, a combined fit determines the $z$-vertex position with a corresponding improvement in accuracy. For a vertex to be reconstructed from the CTD, one or more tracks must have

1. $\geq 4$ hits in the CJC,
2. a distance of closest approach, $DCA$, from the nominal $r$-$\phi$ interaction position $\leq 3\,\mathrm{cm}$,
3. a distance in $z$ from the nominal interaction point of the point where the $DCA$ is defined, $|Z_{DCA} - Z_0| \leq 120\,\mathrm{cm}$,

4. a $\chi^2$ of the vertex fit $\leq 50$

whilst for a track in the FTD to result in a vertex, it must have

1. $|Z_{DCA} - Z_0| \leq 100\,\mathrm{cm}$,
2. $DCA \leq 5\,\mathrm{cm}$,
3. a momentum $P \geq 400\,\mathrm{MeV}$.

The NCLQSQ selection demands

1. no activity in the ToF, or at least one ToF signal in the interaction window with not more than two signals in the background window.
2. the existence of a BEMC cluster with
   (a) energy $E' \geq 6\,\mathrm{GeV}$
   (b) a centre of gravity outside the 'inner triangle' region of the BEMC, that is $|x_{cog}| \geq 13\,\mathrm{cm}$ or $|y_{cog}| \geq 13\,\mathrm{cm}$
   (c) a reconstructed spatial point in the BPC within 10 cm in the $r$-$\phi$ plane, or an energy weighted cluster radius, $R \leq 8\,\mathrm{cm}$

To avoid problems associated with temporal misalignment of the information from the various detectors, the ToF requirement was checked for three bunch crossings: the nominal bunch crossing, and one bunch crossing before and after. To allow the efficiency of the ToF to be monitored, the ToF requirement was not applied to one out of every ten events.

In addition to the requirements for events with electron candidates in the BEMC outlined above, the NCLQSQ class also includes events with a cluster having an energy of more than 4 GeV in the "overlap" region, where the angle of the scattered electron is less than $156^o$, and the energy deposited may be shared between outer region of the BEMC and the most backward region of the LAC. In this region a special clustering technique was applied to combine individual clusters in the LAC, with $Z_{cog} \leq -140\,\mathrm{cm}$, with clusters in the BEMC, with $R_{cog} \geq 64\,\mathrm{cm}$, if they were within 20 cm of one another in the $r$-$\phi$ plane [54].

### 4.4.3 DST Selection

In the DST selection, the ToF cut described above was applied to the NCHAD class. For the NCLQSQ class, the DST selection required a higher energy in the BEMC cluster of $E \geq 8\,\mathrm{GeV}$.

### 4.4.4 Mini–DST Selection

Although the data sample from the NCHAD and NCLQSQ classes can be stored on disk after the DST selection, a further selection is made to provide a common base for structure function analysis and to further speed the analysis process. The mini-DST selection required

- a BEMC cluster with energy $E \geq 7\,\mathrm{GeV}$,
- a reconstructed $z$-vertex,
- a BPC spatial point within 5 cm of the most energetic BEMC cluster.

The mini-DST selection reduces the number of events in the data sample from $\sim 365 \cdot 10^3$ in the POT sample to $\sim 96 \cdot 10^3$ events.

### 4.4.5 Final Selection

Although the POT, DST, and mini–DST selections have a high efficiency for low $Q^2$ NCDIS, a significant contribution from background processes remains. This is because the selection up until the mini–DST level has to be as insensitive to any changes arising from improvements in the understanding of the performance, efficiency and calibration of the detector.

To eliminate, as far as possible, the remaining backgrounds, an additional selection stage is necessary to render the final sample suitable for detailed physics analysis. This selection is based upon:

1. Electron identification. Further cuts are placed upon the lateral dispersion of the EM cluster, and how well it can be associated with a spatial point in the BPC. By using the limited spatial resolution of the ToF device to associate background signals with electron candidates in the BEMC, the ToF requirements can be further tightened.

2. Accurate measurement of the position and energy of the EM cluster. To ensure that the EM cluster is well contained in the BEMC, restrictions on the position of the cluster with respect to the edges of the BEMC are necessary.

3. Event kinematics. By restricting the data sample to a specific kinematic region, contamination from photoproduction background can be reduced, radiative corrections minimised, and confidence gained that the reconstructed kinematic variables are an accurate reflection of the truth.

4. Background rejection using tracking information. In addition to simply demanding a well reconstructed vertex, the position of the vertex can be constrained to lie within the nominal interaction region for beam-beam collisions, further reducing the contamination from beam-gas and beam-wall interactions. Further selection is possible on the "quality" of the event, by requiring that the tracking information is consistent with a NCDIS event.

5. Further rejection of synchrotron radiation induced background.

These additional requirements are described below.

### Electron Identification

Electrons entering the BEMC will, on average, produce showers with less lateral dispersion than those produced by hadronic particles. Events are required to have an energy weighted cluster radius, ECRA, of less than 4 cm. This is an effective discriminator against photoproduction events in which a charged hadron produces energy deposition in the BEMC, although it is not effective against events in which a neutral hadron, for example a $\pi^0$, decays via $\pi^0 \rightarrow 2\gamma$ before reaching the BEMC and thus produces an EM shower.

Demanding that the electron candidate is associated with tracking information, that is a spatial hit in the BPC, can effectively reject clusters originating from neutral hadrons. For the final selection, the distance between the centre of gravity of the cluster and the nearest spatial BPC hit, DCLBP, is required to be less than 4 cm. The distributions of ECRA and DCLBP for the DST sample are shown compared to DIS Monte Carlo and photoproduction Monte Carlos in figure 4.2. For the data with $E_e > 16$ GeV, no contamination from photoproduction

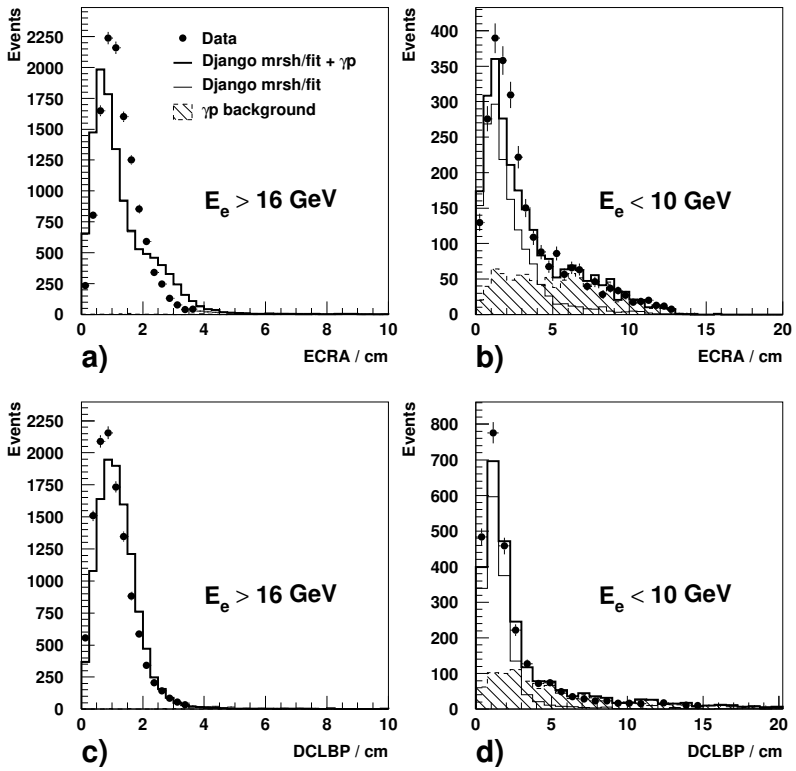


Figure 4.2: Distributions of ECRA and DCLBP for data from the DST sample (see text). The data are compared with the predictions from DIS and photoproduction background Monte Carlos, where both components are normalised according to the luminosity.

remains, whereas in for the data with $E_e < 10$ GeV significant tails due to this component are observed in both distributions, which are well described by the Monte Carlo. The effects of the disagreement between data and Monte Carlo at

high electron energy (figures 4.2a and 4.2c) have been studied in detail, and are not found to constitute a significant systematic uncertainty [61].

The ToF requirement of the mini-DST selection requires that there is either no activity in the ToF, or there is at least one signal in the interaction window and not more than two signals in the background window. Contributions from backgrounds can be further reduced by verifying that if there is a signal in the background window, it cannot be associated spatially with the electron candidate. The position of the candidate cluster centre of gravity ("*cog*") is projected onto the plane of the ToF device, and the event is rejected if there is a match between the *cog* and the ToF background signal.

### Accurate Cluster Measurement

In order that the position and energy of the electron candidate are well measured, care must be taken that the shower is well contained in the BEMC. In the POT selection, the cut on the position of the cluster centre of gravity ($|x_{cog}| \geq 13\,\mathrm{cm}$ or $|y_{cog}| \geq 13\,\mathrm{cm}$) excludes the innermost region of the BEMC covered by the 'inner triangle' stacks, in which an abnormally high rate of triggers are observed. In addition, these stacks are not fully instrumented, leading to an inferior reconstruction of the *cog*, and are not well calibrated [61]. In this analysis, the position of the electron candidate is taken from the spatial BPC hit, not the cluster *cog*, as the BPC position measurement is significantly more accurate[5]. The more accurate information from the BPC allows a more stringent cut of $\theta_{BPC} \leq 173^o$ to be made so that the inner triangle region of the BEMC is more effectively excluded.

The active region of the BPC has an outer radius of $\approx 60$cm. In order that the sample be well contained within the coverage of the BPC, a requirement of $\theta_{BPC} \geq 156^o$ is imposed on the final sample.

[5]Recall that the spatial resolution of the BEMC is $\sigma_{x,y} \sim 13\,\mathrm{mm}$ (section 3.3.2), whereas the spatial resolution of the BPC is $\sigma_{x,y} \sim 1\,\mathrm{mm}$ (section 3.4.3).

### Event Kinematics

In addition to the limits on $y$ discussed in section 4.3, the remaining contribution from photoproduction background in the mini–DST sample necessitates further restrictions of the kinematic extent of this study.

As the energy of the electron candidate decreases below $\sim 15\,\mathrm{GeV}$, the contribution from photoproduction becomes more significant. For the electron method, the restriction of $y < 0.6$ required to limit the size of radiative corrections corresponds to a lower limit on the electron energy of $10.6\,\mathrm{GeV}$, which limits strongly the contribution from photoproduction remaining after the selection described in the preceding sections. In figure 4.3 the distributions of the electron candidate energy and $y_e$ are shown for the data, and for DIS and photoproduction Monte Carlos after the application of all selection cuts excluding that on electron energy (or $y_e$ for the electron method).

The upper limit of $y_\Sigma < 0.7$ necessary for the $\Sigma$ method is not equivalent to a well defined limit on the electron energy, as information from the hadronic final state is included for the calculation of $y_\Sigma$. Therefore, a further cut of $E' > 8\,\mathrm{GeV}$ is used for this reconstruction method.

Studies of the description of the electron energy spectrum for energies below $8\,GeV$ (not shown in figure 4.3), and of the description of the signal in the electron tagger by the photoproduction Monte Carlo, lead to the conclusion that this background is known to an accuracy of 50% of the estimated contamination [60].

## Background Rejection Using Tracking Information

The position of the event vertex can be used to reduce the contribution from beam-gas and beam-wall interactions, as events produced by such interactions will not preferentially be produced in the region of the nominal interaction point. The distribution of the event $z$-vertex position is shown in figure 4.4.

In addition to the position of the event z-vertex, the degree to which the

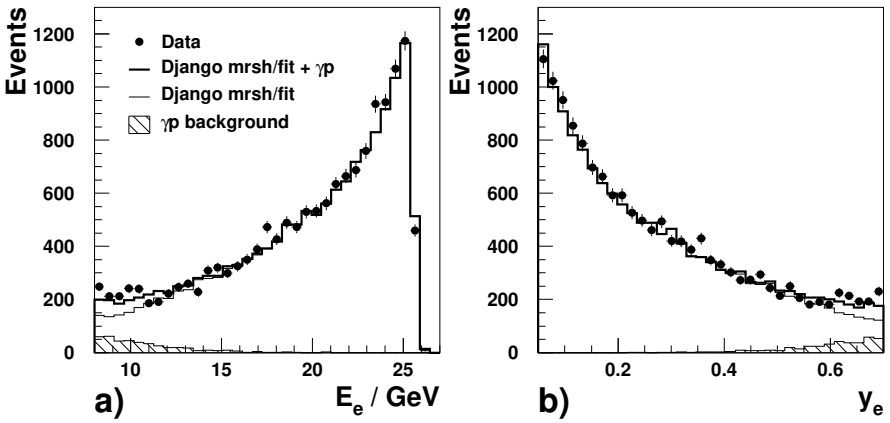


Figure 4.3: Estimated contribution of photoproduction background to the final selection. Both the photoproduction and DJANGO simulation are absolutely normalised to the data luminosity. The upper solid line shows the DJANGO and photoproduction added together. The structure function used for DJANGO is taken from recent measurements at HERA (see text).

tracking information is consistent with a collision in the interaction region can be used to further reduce background contamination. Events were rejected in which less than 16% of the hits in CJC1 and CJC2 were contained in vertex constrained tracks.

### Rejection of Synchrotron Induced Background

The dominant contribution to the raw rate of the BSET trigger (section 3.3.2) comes from events in which a substantial proportion of the total energy of the BEMC cluster is collected in a single wavelength shifter channel. These events are caused by synchrotron radiation from the electron beam entering the BEMC from the rear and interacting in the wavelength shifters. A conservative cut is applied to reject the majority of these events at the L4 farm (section 3.9) limiting the maximum fraction in a single diode to 0.95. A more stringent requirement limiting the maximum fraction to 0.8 is made in the final selection. No events of this type are predicted by the Monte Carlo to remain after this cut.

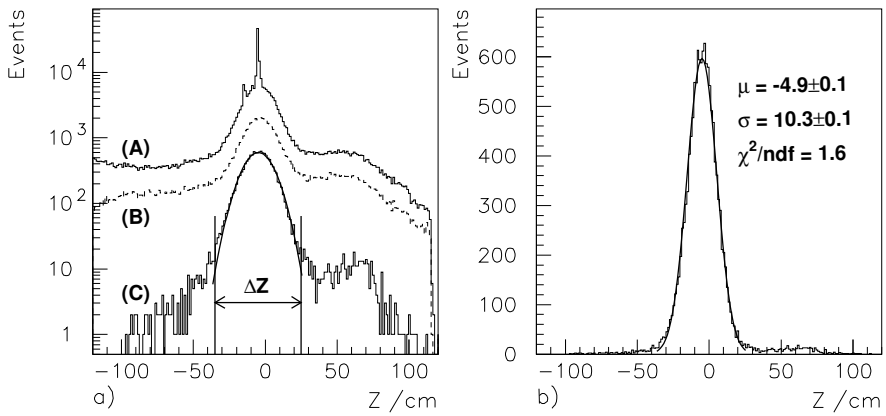


Figure 4.4: Distribution of the position in $z$ of the event vertex for the event samples. a) from top to bottom: (A) the DST sample, (B) the mini-DST sample, and (C) the final selection, excluding the $z$ vertex requirement. For the final selection, the range in $z$ vertex position accepted, $-35\,\mathrm{cm} \leq z \leq 25\,\mathrm{cm}$, is shown. b) the final selection, with a linear scale on the vertical axis. The mean $\mu$ and standard deviation $\sigma$ are from a Gaussian fit performed over the range accepted, $\Delta z$, which is shown in a).

### 4.4.6 Summary of DIS Selection Procedure

The selection used to identify low $Q^2$ NCDIS is

- BCL2 Trigger (not used for Monte Carlo)
- Maximum fraction of $E_{BEMC}$ from single diode 80%
- $7.5 \leq Q^2 \leq 80\,GeV^2$
- $0.05 \leq y_e \leq 0.6$ $(0.01 \leq y_\Sigma \leq 0.7)$
- $156^o \leq \theta_e \leq 173^o$
- ToF requirement
- BEMC cluster centre of gravity outside of inner triangle region $(|x_{cog}| \geq 13\,\mathrm{cm}$ or $|y_{cog}| \geq 13\,\mathrm{cm})$
- Reconstructed $z$-vertex from the FTD or CTD in the region $(-35\,\mathrm{cm} \leq z \leq 25\,\mathrm{cm})$

- Distance of nearest BPC point from cluster cog DCLBP $\leq 4\,\mathrm{cm}$
- Energy weighted cluster radius ECRA $\leq 4\,\mathrm{cm}$
- Fraction of hits in CJC1 and CJC2 in vertex constrained tracks $\geq 16\%$

The distribution in $(x, Q^2)$ of the 16428 events satisfying these cuts can be seen in figure 4.5.

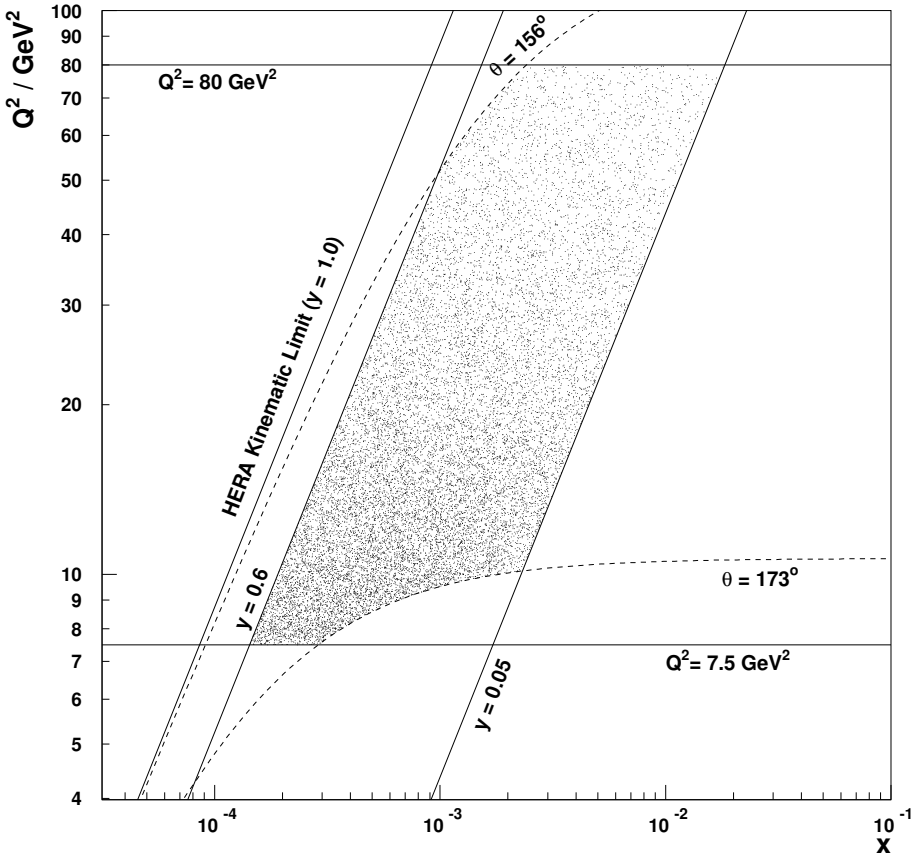


Figure 4.5: The final sample of neutral current DIS events selected with the electron reconstruction method.

### 4.4.7 Remaining Background

Photoproduction events can still remain in the sample after selecting on ECRA, DCLBP and $E'$. In particular, if a photoproduction event contains a neutral and charged hadron which both enter the BEMC separated by only a small angle, then the neutral hadron can produce an EM shower, and the charged hadron can provide an associated hit in the BPC. For those data selected with the electron ($\Sigma$) method, the remaining contribution from photoproduction after all the cuts described above is estimated to be $1.0 \pm 0.5\%$ ($1.1 \pm 0.6\%$) of the total sample, rising to $13 \pm 7\%$ ($16 \pm 8\%$) for those data with $E' < 12\,\mathrm{GeV}$.

The contribution from backgrounds not associated with beam-beam collisions can be estimated by studying the non-colliding bunches. The number of events from the electron pilot bunch surviving all cuts is 2, while no events remained from either the proton pilot bunches or empty bunches. The fraction of the total proton current in the pilot bunches was calculated to be $0.074 \pm 0.007$, while for the electron pilot bunches the fraction was $0.138 \pm 0.025$ [61]. These fractions translate into estimates of the total remaining non-beam background of $15 \pm 10$ and $0 \pm 14$ from electron and proton beam induced backgrounds respectively.

### 4.4.8 Efficiency of Selection

Where possible, the efficiencies of all aspects of the selection are determined directly from the data. Although the simulation of the H1 detector is intended to include as many resolution and efficiency effects as possible, in practice there may still be small residual effects visible in the data which are not adequately described by the Monte Carlo.

The BCL2 trigger has an efficiency of $100 \pm 1\%$ for the energy range $E' \geq 10\,\mathrm{GeV}$ [6], whilst studies of the efficiency of the ToF requirement suggest an additional inefficiency of $1 \pm 1\%$ in the data.

In all of the Monte Carlo data, the position of the event vertex is parameterised by a Gaussian distribution with a width of 10 cm centred at $-5$ cm, whilst in the data the longitudinal profiles of the electron and proton bunches produce

a $z$-vertex distribution that is not so simple (figure 4.4). In particular, a small fraction of the measured luminosity comes from collisions involving protons in the satellite bunches, visible in figure 4.4a as the broad peak at $z \sim 70\,\mathrm{cm}$. These are attributable to the late injection into HERA of a component of the proton bunch. Studies using the ToF and luminosity systems reveal that $5.2 \pm 1.0\%$ of the total luminosity is rejected by demanding a $z$-vertex in the range $-35\,\mathrm{cm} \leq z \leq 25\,\mathrm{cm}$, 3.5% of which may be attributable to the effect of the satellite bunches.

The determination of the efficiency of the $z$-vertex cut requires the estimation of the number of genuine NCDIS events surviving all of the selection criteria except the $z$-vertex requirement. The satellite bunches complicate the determination of the efficiency for finding a reconstructed vertex in this region, as genuine $ep$ collisions are rejected by demanding a $z$-vertex position within the nominal interaction region.

In addition, any remaining photoproduction in the sample will further reduce any efficiency calculated naively from the data. The vertex finding efficiency can be determined independently using the CIP chambers [62]. A vertex can be constructed by demanding a coincidence between hits in the two cathode planes of the CIP in combination with a BPC point in front of the electron candidate, reducing the contamination from photoproduction and providing and entirely independent vertex determination. An analysis using the CIP shows that an additional global inefficiency of $2 \pm 2\%$ must be introduced into the Monte Carlo [62].

The CIP can also reduce the uncertainty in the estimation of the efficiency of the DCLBP cut. By requiring a coincidence of hits in the CIP to lie close to a line projected from the reconstructed $z$-vertex and the cluster centre of gravity, the number of photoproduction events passing all cuts except the DCLBP requirement can be reduced. Such an analysis demonstrates that the efficiency of the DCLBP criterion is well described by the Monte Carlo [62].

## 4.5 Summary

The selection procedure outlined in this chapter results in 16221 events for the electron method, and 19418 events for the $\Sigma$ method. The remaining background from non-beam backgrounds to estimated to be negligible ($\ll 1\%$). Contamination from photoproduction background amounts to $\sim 1\%$, concentrated at low electron candidate energies, which correspond to low values of $x$ or high values of $y$, where it reaches $\sim 15\%$ of each sample.

# Chapter 5

# The Observation of Diffractive DIS

## 5.1 The Observation of Large Rapidity Gap Events

The low $Q^2$ NCDIS data obtained by the selection described in the previous chapter exhibit an excess over the expectations of standard NCDIS models of events in which little or no energy deposition is observed in a large region of rapidity adjacent to the proton beam direction.

First results of the analysis of these "Large Rapidity Gap" (LRG) events have been reported by both the ZEUS and H1 collaborations [63, 64].

In this chapter, it is demonstrated that this excess of LRG events may not be attributed to either fluctuations in hadronisation in standard models of DIS, or unexpectedly high contributions from the known beam-beam or beam-gas backgrounds to the DIS sample. It is shown that these events may be described by the presence of diffraction in the DIS sample, where the highly virtual photon probes a colourless component of the proton, the pomeron; a picture in which large rapidity gaps are naturally produced. Detailed analysis of the data leads to a phenomenological model, based upon a partonic description of the pomeron, which can describe all of the observed properties of the LRG events. The understanding so gained allows predictions of the possible extent of the total contribution to DIS from diffraction to be made.

The angular coverage of the H1 liquid argon calorimeter (section 3.3.1) corresponds to a maximum measurable rapidity of $\eta_{\rm LAC} \sim 3.65$, with small variations introduced by the exact position of the $ep$ event vertex. The size of the observed 'rapidity gap' can be characterised by $\eta_{max}$, defined to be the rapidity of the cluster in the LAC with energy $E \geq 0.4\,{\rm GeV}$ that is nearest to the proton beam direction.

Figure 5.1 shows an example of a DIS events with a large rapidity gap in the LAC, contrasted with a more typical low $Q^2$ DIS event. For the LRG event in figure 5.1b the first significant deposition of energy occurs at $\theta = 54^o$, or $\eta_{\rm max} = 0.66$, which corresponds to an observed rapidity gap of $\Delta\eta = \eta_{\rm LAC} - \eta_{\rm max} \approx 3$ units of rapidity. The distribution of $\eta_{\rm max}$ in the low $Q^2$ NCDIS data, along with the expectation from standard–DIS models, is shown in figure 5.2. The observation of this excess of events with a large rapidity gap is unaffected by varying the minimum energy required for a cluster, and an excess is also observed if other definitions are used for the position of the first significant deposition of energy [64].

## 5.2 The Selection of Large Rapidity Gap Events Using $\eta_{\rm max}$

The failure of the conventional DIS models to describe the $\eta_{\rm max}$ distribution in figure 5.2 suggests that there may be an additional mechanism present in the data. To isolate a sample of large rapidity gap events in which the contribution from processes described by the conventional models of DIS is expected to be small, a selection is made requiring that $\eta_{\rm max} < 1.8$. A total of 1043 events, that is 6.8% of the low $Q^2$ DIS sample, satisfy this criterion. Of these, 15 events have a charged track reconstructed in either the CTD or FTD in the angular region $4.6^o < \theta < 18.8^o$ ($3.2 > \eta > 1.8$) with momentum greater than 0.3 GeV, and none have such a track with momentum greater than 0.4 GeV. For 17 events, there is no cluster other than the scattered electron with energy greater than 0.4 GeV in either the LAC or the BEMC. An alternative analysis requiring the total energy of all cells with rapidity $\eta_{\rm cell}$ within the range $\eta_{\rm LAC} > \eta_{\rm cell} > \eta_\Sigma$ to be less than 0.4 GeV yields 979, or 6.4%, selection $\eta_\Sigma = 1.8$.

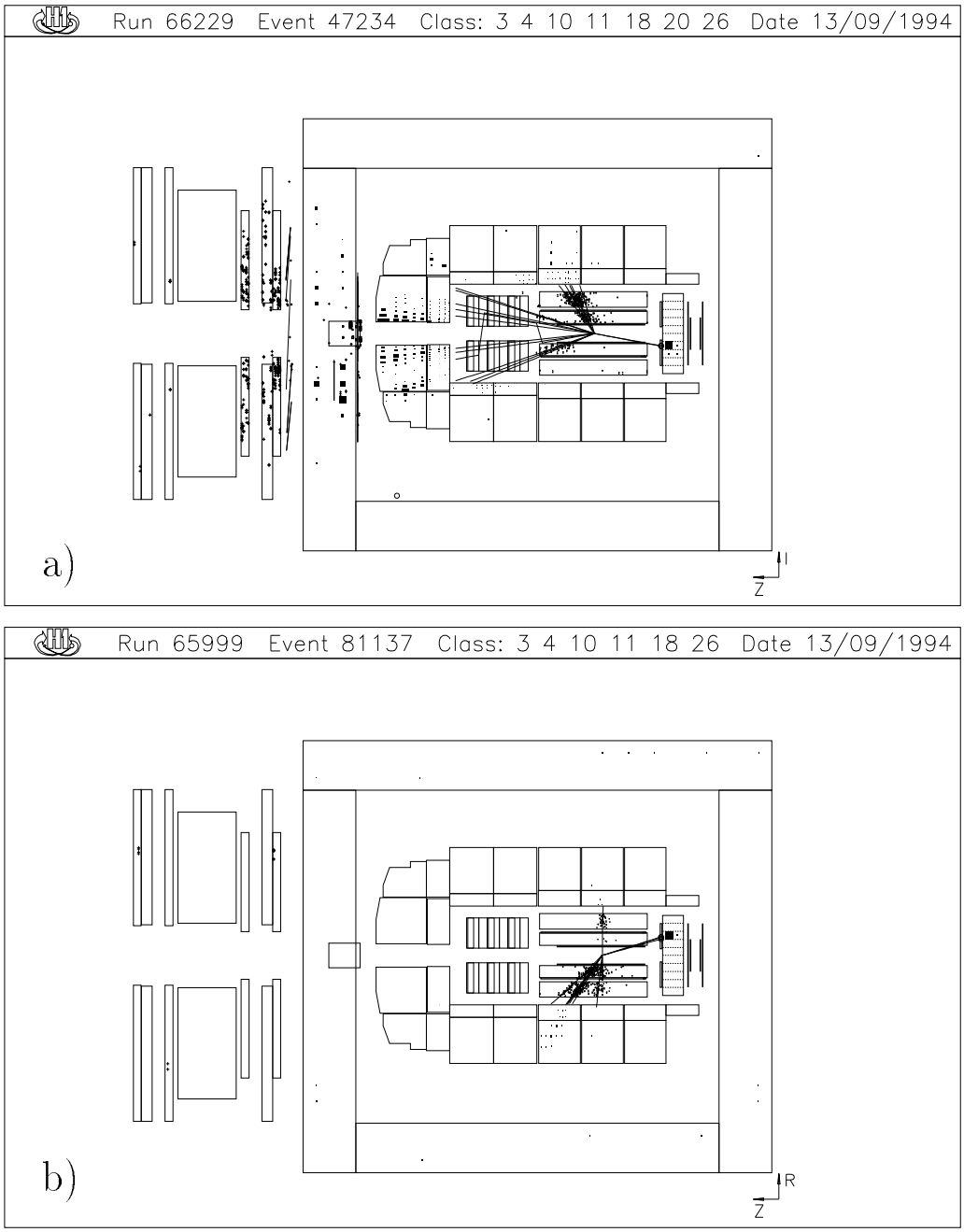


Figure 5.1: a) A typical low $Q^2$ DIS event. Considerable activity is visible in the Plug, Forward Muon Detector, Forward Iron end cap and the inner forward region of the LAC. b) An example of a Large Rapidity Gap event (LRG). The detectors in the forward region mentioned above all contain no significant activity above noise thresholds.

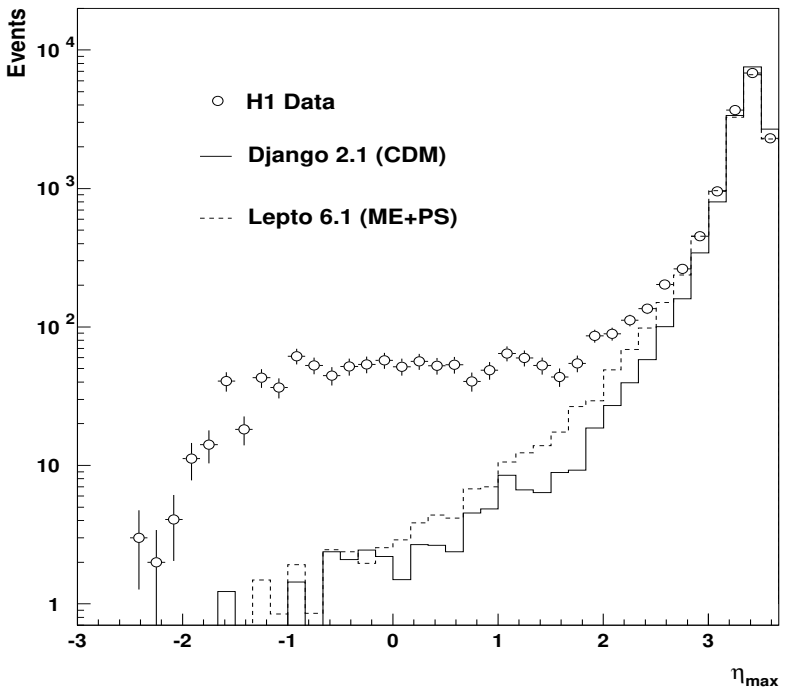


Figure 5.2: Distributions of $\eta_{\max}$ for low $Q^2$ NCDIS data along with expectation from CDM and MEPS. The Monte Carlo are normalised to the luminosity of the data.

### 5.2.1 Background Studies for the $\eta_{\max}$ Selection

It is evident from the distribution of $\eta_{\max}$ in figure 5.2 not only that a small fraction of events simulated according to the prescriptions of conventional DIS Monte Carlos satisfy the criterion $\eta_{\max} < 1.8$, but also that the level of contamination of the sample depends upon the particular model of DIS used. The prediction for the number of events in the $\eta_{\max} < 1.8$ sample from standard–DIS Monte Carlos varies from 72 to 124, where the uncertainty arises from the current understanding of the proton structure functions, and of the process of hadronisation. If recent measurements of the proton structure function from the H1 collaboration [6] are used in conjunction with the Colour Dipole Model (CDM) of QCD radiation, which can best reproduce measurements of the hadronic final state [35], then a contribution of $72 \pm 2\ (F_2) \pm 52$ (QCD) events is expected. The MEPS

prescription for QCD radiation, which describes the energy flow in the hadronic final state less well than CDM, although it provides a better description of jet rates, is used to estimate the uncertainty due to QCD radiation.

Pile–up in the liquid argon calorimeter, the effect of energy deposited in earlier of later bunch crossings, which produces spurious energy deposition in the forward region of the calorimeter and therefore biases against the rapidity gap selection, was found to be insignificant [65]. Proton beam–gas events are not topologically compatible with a large rapidity gap in the vicinity of the proton beam, and do not contribute to the sample.

The contribution from electron beam–gas events, in which beam electrons interact with residual gas particles in the beam pipe, is likely to be enhanced in the large rapidity gap sample, as the electron interacts with a proton that is essentially at rest. Thus the contribution from this source of potential background must be studied in detail. Three independent methods are adopted:

- analysis of the event kinematics given the assumption of an electron beam–gas event
- analysis of the event $z$-vertex distribution
- contribution to the sample from non-colliding bunches

**Kinematic analysis**

The centre of mass energy, $\sqrt{s'}$, for the collisions of 26.7 GeV electrons and stationary protons is $s' = 100.2\,\mathrm{GeV}^2$, compared to $s^{ep} = 87576\,\mathrm{GeV}^2$ for $ep$ beam beam collisions. This means that for a given reconstructed $(y, Q^2)$, the value of $x$ is increased by a factor of $\frac{s^{ep}}{s'} = 874$ if it is assumed to be a beam-gas rather than a beam-beam collision. For 317 out of the 1043 events in the sample (30%) this results in unphysical kinematics with $x > 1$. Given that only part of the sample can be demonstrated to be incompatible with electron beam–gas background on kinematic grounds alone, the residual level of this background must be estimated by other means.

**Analysis of the event $z$-vertex distribution**

Electron beam–gas events produce a flat distribution in $z$ to the extent that the reconstruction efficiency is constant throughout the geometrical acceptance domain of the CTD. Consequently an estimation of the contribution from such events can be made from the extent to which the $z$-vertex distribution of the final sample is not consistent with a Gaussian. The $z$-vertex distribution of the $\eta_{\max}$ sample is shown in figure 5.3a, where for this particular investigation the final selection of $-35\,\mathrm{cm} < z_{vertex} < 25\,\mathrm{cm}$ has not been imposed. Events outside of the accepted region in $z$ are visible. Figure 5.3b, showing the reconstructed $z$-vertex

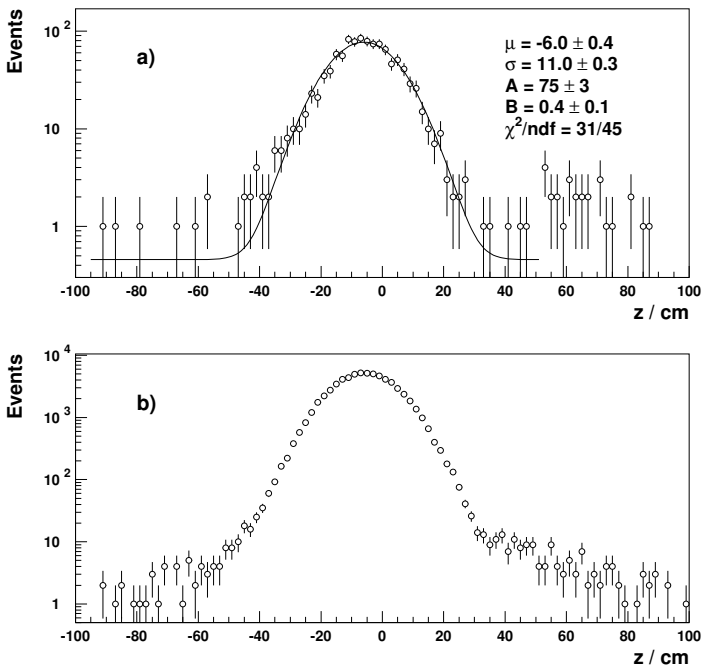


Figure 5.3: Distributions of the $z$-vertex for a) the $\eta_{\max}$ sample and b) a DIS Monte Carlo with a Gaussian generated vertex distribution of width $\sigma = 10\,\mathrm{cm}$. The fit performed on the data excludes the region of the satellite bunch, visible as a slight excess at $z \sim 60\,\mathrm{cm}$. The function with which the data are fitted is detailed in the text.

for a Monte Carlo simulation of low $Q^2$ DIS generated with a Gaussian $z$-vertex

position, demonstrates that least some of these events may be attributable to misidentification of the event vertex during reconstruction. Performing a fit of the form

$$N(z;\mu,\sigma) = \frac{A}{\sigma\sqrt{2\pi}}\ exp\left\{\frac{-(z-\mu)^2}{2\sigma^2}\right\} + B$$

to the $\eta_{\max}$ sample and accounting for the effect of bad vertex reconstruction suggests a residual background of $10 \pm 3$ events in the final $\eta_{\max}$ sample.

**Analysis using non-colliding bunches**

The $\eta_{\max}$ sample contains one event from the electron pilot bunches. Applying a correction for the relative luminosity in the colliding and non-colliding bunches gives an estimate of $8 \pm 8$ electron gas events in the sample. This is in agreement with the estimate based on the $z$-vertex distribution.

To summarise, there is evidence that the background from electron beam-gas interactions is enhanced in the large rapidity gap sample, with the estimated contribution rising from $\approx 0.1\%$ for the total low $Q^2$ sample to $\approx 1\%$ for the LRG sample. However, two independent methods of evaluating the background preclude contributions above the percent level.

Using the simulation of photoproduction produced to study background in the low $Q^2$ sample as a whole demonstrates that non-diffractive photoproduction does not contribute to the rapidity gap sample. This is to be expected: if conventional DIS contributes approximately 7% to the $\eta_{\max} < 1.8$ sample, and conventional photoproduction contributes $\approx 1\%$ to the DIS sample, then if it is assumed that the $\eta_{\max}$ selection acts upon the two potential contributions in the same way then 0.7 photoproduction events are expected amongst the 1043 LRG events.

Extrapolation of the measured hadronic two photon cross section [66] shows that the two photon processes contribute $\ll 1$ event to the sample. Three Compton events ($ep \rightarrow ep\gamma$) are removed from the sample. The muon system (section 3.5) is used to verify that the contribution from cosmic shower events is insignificant [65, 64].

Having established that the observation of a significant number of large ra-

pidity gap events cannot be accounted for within the conventional framework of DIS as fluctuations in the process of hadronisation, or from non-colliding beam backgrounds, the possibility that an additional mechanism may be present in DIS must be investigated. This possibility will be discussed in the remainder of this chapter.

## 5.3 Properties of the Large Rapidity Gap Events

In this section we examine the basic properties of the large rapidity gap events: how they are distributed in terms of the basic kinematic variables of deep–inelastic scattering, and the basic properties of the hadronic final state. The results of the comparison of these properties with those of the DIS sample as a whole may give some indication of the nature of the mechanism producing these events.

The large rapidity gap events are distributed over the entire $Q^2$ and Bjorken-$x$ range studied, that is $7.5\,\mathrm{GeV}^2 < Q^2 < 80\,\mathrm{GeV}^2$ ($\overline{Q^2} = 17.3\,\mathrm{GeV}^2$) and $10^{-4} < x < 10^{-1.75}$ ($\overline{x} = 0.0010$). The distribution of the LRG events in $(x, Q^2)$ is shown in figure 5.4. It is evident that in comparison with the total low-$Q^2$ sample (figure 4.5), the relative contribution from LRG events falls as $Q^2$ or $x$ increase as the LRG events are produced preferentially at lower values of $x$ and $Q^2$ (for the total sample $\overline{Q^2} = 20.0\,\mathrm{GeV}^2$ and $\overline{x} = 0.0016$.)

The fraction of LRG events in the data as a function of $Q^2$ is shown in figure 5.5a, where $Q^2$ is reconstructed from the energy and angle of the scattered electron. The ratio $R(Q^2)$ is seen to fall with increasing $Q^2$. The may not reflect the underlying mechanism producing the LRG events due to the correlation between $Q^2$ and $x$. Events with large $Q^2$ are preferentially found at larger values of $x$ than those at small $Q^2$, as can be seen in figure 5.4. Events with large $x$ tend to have more hadronic activity in the forward direction than those at small $x$. This can be understood by considering the direction of the scattered parton in the Naive Quark Parton Model, $\eta_{\mathrm{QPM}}$, which is given by

$$\eta_{\mathrm{QPM}} = \frac{1}{2}\log\left\{x \cdot \left(\frac{xs}{Q^2} - 1\right) \cdot \frac{E_p}{E}\right\} \tag{5.1}$$

An increase in $x$ is strongly correlated with a shift of $\eta_{\mathrm{QPM}}$ forwards, whilst the

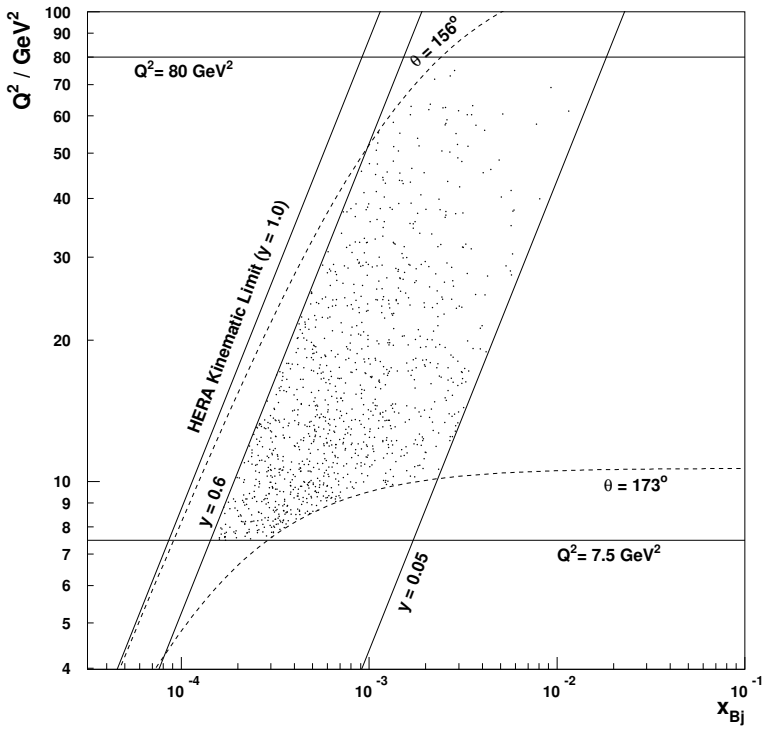


Figure 5.4: The distribution of large rapidity gap events in the low-$Q^2$ DIS sample with the electron reconstruction method.

effect of an increase in $Q^2$ is less pronounced. Thus the use of an $\eta_{\max}$ criterion as a selection may result in a sample biased in $x$. To study this, the ratio $R(Q^2)$ is shown in four narrow bins in $x$ in figures 5.5d-e. Within these narrow bins in $x$, $R(Q^2)$ no longer exhibits any significant dependence on $Q^2$, which is consistent with, but not conclusive evidence for, a production mechanism for the large rapidity gap events which is leading twist in QCD. Note that the accessible range in $Q^2$ is different for the different $x$ regions, which can be seen clearly in figure 5.4. The ratio is seen to decrease with increasing $x$, falling from $\sim 8\%$ for $10^{-3.5} < x < 10^{-3.25}$ to $\sim 3\%$ for $10^{-2.5} < x < 10^{-2.2}$. This decrease is likely to be, at least partially, a result of the bias of the $\eta_{\max}$ selection.

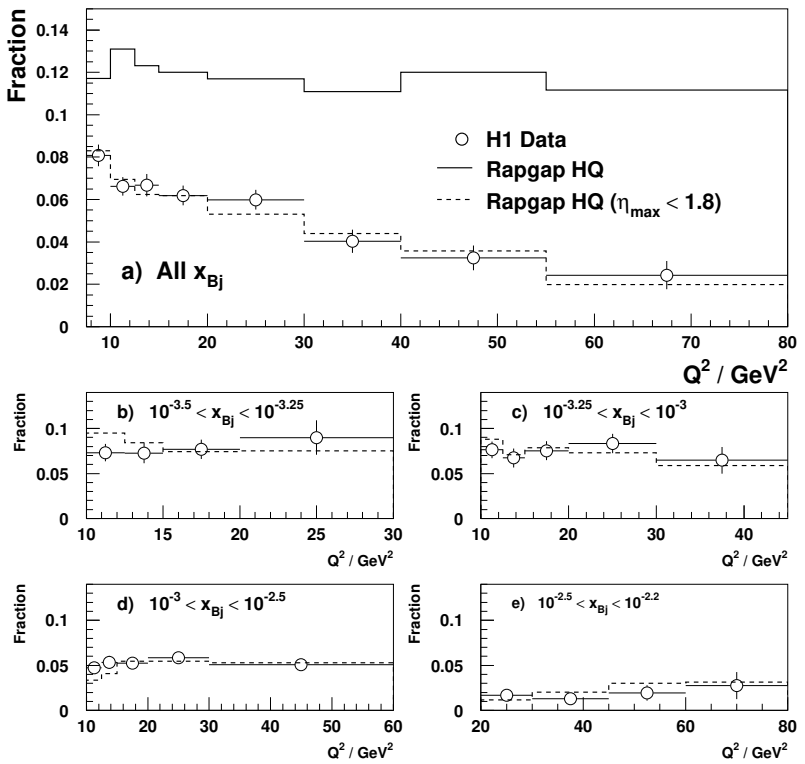


Figure 5.5: The fraction of LRG events, $R(Q^2)$, in the low $Q^2$ DIS sample. a) for the sample as a whole, and b)-e) for different Bjorken-$x$ regions. The background from conventional DIS is subtracted using CDM.

### 5.3.1 Vector Meson Production in the $\eta_{\max}$ Sample

It has been reported elsewhere that between 4 and 5% of the large rapidity gap events in the H1 data are candidates for the exclusive production of light vector mesons $(\rho, \omega, \phi)$ [64]. Such events are characterised by a scattered electron, and only two oppositely signed charged tracks with less than 1.5 GeV of energy in the LAC not spatially associated with those tracks. The two tracks are assumed to be the result of the decay of neutral vector mesons. Such an event is shown in figure 5.6. The distribution of these events in $Q^2$ was found to be similar to that of the LRG sample as a whole. The efficiency for selecting exclusive vector meson production was estimated to be $\sim 50\%$ suggesting that the proportion of exclusive $\rho(770)$, $\omega(783)$ and $\phi(1020)$ in the LRG sample is $\sim 10\%$. No evidence

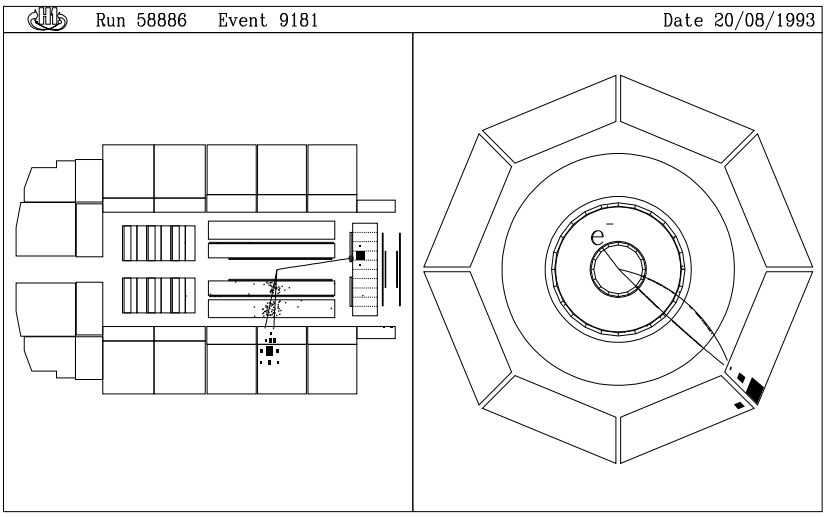


Figure 5.6: An example of a candidate for the diffractive production of light vector mesons. The detector is empty apart from the electromagnetic cluster in the BEMC and the associated BPC "hit", and two oppositely signed charged tracks in the CTD with associated energy in the LAC.

was found for a similar proportion of exclusive $\rho(770)$ production in the DIS events with only two oppositely charged tracks and $\eta_{\max} > 1.8$.

### 5.3.2 Comparison with Deep–Inelastic Electron-Pomeron Scattering

A possible mechanism for the production of large rapidity gaps in DIS is diffractive scattering, in which the exchange of a colourless component of the proton, the pomeron ($\mathbb{P}$), in the scattering process naturally leads to the production of large rapidity gaps (see section 2.7). To study whether such processes can account for the observed LRG events, the data is compared with the RAPGAP Monte Carlo [40], described in section 2.11.2. Figure 5.7 shows the distribution of $\eta_{\max}$ in the data, along with the expectation from RAPGAP assuming a hard quark structure function for the pomeron (HQ). The normalisation of the RAPGAP component is obtained from the number of events with $\eta_{\max} < 1.8$ unaccounted for by the conventional DIS Monte Carlo, here CDM. The shape of the tail of the $\eta_{\max}$ distribution is well described by RAPGAP, and the sum of the RAPGAP and

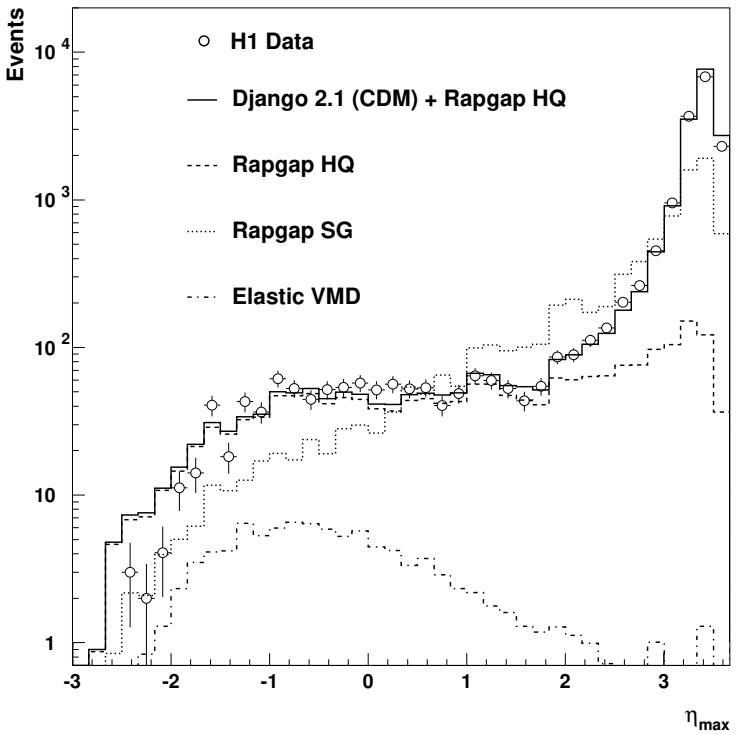


Figure 5.7: Distributions of $\eta_{\max}$ for low $Q^2$ DIS data along with expectation from the CDM, RAPGAP HQ, RAPGAP SG, and the VMD Monte Carlos. The VMD Monte Carlo is normalised to reproduce the observed yield of two–prong events, whilst the HQ and SG components are normalised to reproduce the excess of Large Rapidity Gap Events.

CDM components well reproduces the entire distribution. As the contribution from RAPGAP extends to values of $\eta_{\max}$ above 1.8, it is possible that the $\eta_{\max}$ criterion selects only a fraction of any diffractive component to DIS, such that if the LRG events can be correctly interpreted as a manifestation of diffraction, then the total contribution of diffraction may be significantly larger than the fraction of observed LRG events. The prediction from RAPGAP HQ, normalised to the LRG events, is also shown for $R(Q^2)$ in figure 5.5. The contribution of RAPGAP HQ with $\eta_{\max} < 1.8$ is in good agreement with the data. If RAPGAP HQ is used to predict the total contribution from diffraction, then a component of $\approx 12\%$, independent of $Q^2$, is expected (figure 5.5a). The SG model cannot, by itself, describe the observed form of the $\eta_{\max}$.

Diffractive scattering is expected to result in lower values for the mass of the total hadronic final state, $M_X$, than standard–DIS. In figure 5.8 it can be

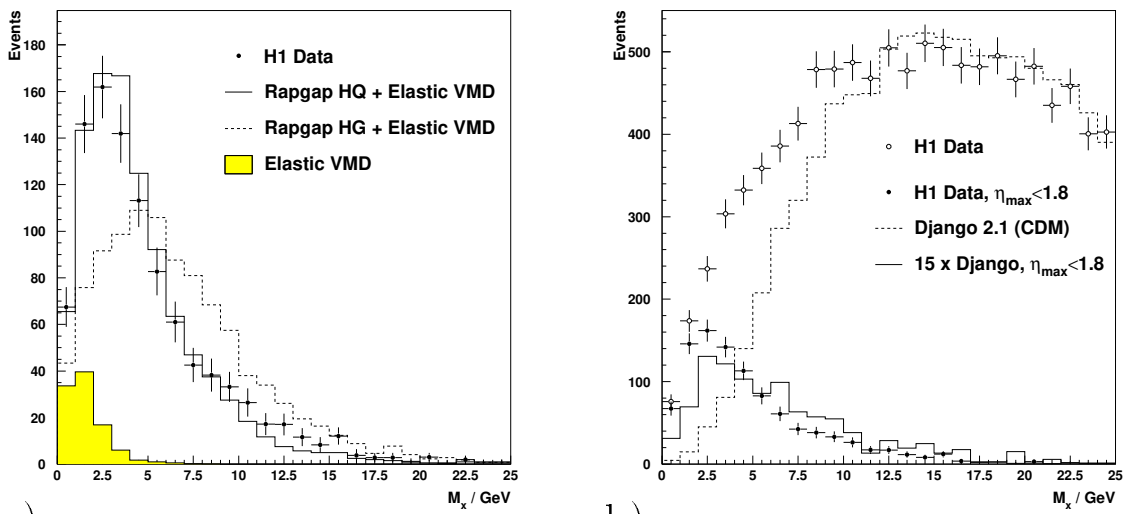


Figure 5.8: a) The $M_X$ distribution of the data with $\eta_{\max} < 1.8$, after the subtraction of background from standard–DIS. The VMD contribution (shaded) is normalised to reproduce the observed yield, and the HQ and HG Monte Carlos such that the sum of RAPGAP and VMD matches the data. b) The $M_X$ distribution of all the DIS data (open points) and with $\eta_{\max} < 1.8$ (closed points) compared to all CDM data (dotted line), and those CDM data with $\eta_{\max} < 1.8$ (solid line) $\times 15$.

seen that the sample selected by the criterion $\eta_{\max} < 1.8$ does, indeed, have an $M_X$ distribution peaked at lower values of $M_X$ than the total DIS sample. It is also evident, however, that the remaining background from standard–DIS in the $\eta_{\max} < 1.8$ sample also has a similarly lower characteristic $M_X$ scale. The lower masses are therefore likely to be a direct result of the bias in $M_X$ inherent in the $\eta_{\max}$ selection: large masses will be spread over a greater region in phase space, and will be inhibited by the requirement that the forward region is essentially devoid of energy. Thus, although the $\eta_{\max} < 1.8$ criterion selects events with lower masses, in good agreement with the expectations of a diffractive Monte Carlo, the strong possibility of selection bias means that the $M_X$ spectrum cannot be interpreted as evidence for diffraction.

The total failure of models of conventional DIS to describe the rate of large

rapidity gaps in the data, along with the excellent description of these data by models of diffraction is highly suggestive of diffraction in DIS. The attempt to describe these data with a partonic picture of a deep–inelastic electron pomeron interaction is successful, with the data strongly favouring a hard rather than a soft partonic structure for the pomeron, although given the uncertainties in the unmeasured flux factor and possible acceptance effects, this preference does not constitute a precise determination. In particular, some small additional soft component arising from QCD evolution in the pomeron is not excluded.

This agreement between Large Rapidity Gap data and diffractive–DIS Monte Carlos does not, however, demonstrate without ambiguity that the mechanism responsible for the production of these events is diffractive.

## 5.4 Beyond the $\eta_{\max}$ Selection

The partonic model of pomeron physics with which the data are compared in the previous section suggests that the $\eta_{\max}$ selection only identifies a part of the total contribution from diffraction, as a large number of events are predicted to have a rapidity gap too small to extend sufficiently far into the LAC to allow discrimination between diffraction and normal DIS on the basis of $\eta_{\max}$ alone. Moreover, it suggests that the $\eta_{\max}$ selection introduces significant biases into the sample, such that the underlying characteristics of the diffractive contribution are distorted in the sample retained. For these reasons it is natural to attempt to extend the search for a signal in the data characteristic of diffraction by looking for rapidity gaps closer to the forward proton beam direction, beyond the acceptance limit of the liquid argon calorimeter, $\eta_{\rm LAC} \approx 3.65$.

The motivation for identifying rapidity gaps closer to the proton beam direction is immediately apparent from figure 5.9, which shows the distribution of $\eta^{\rm gen}_{\rm max}$, defined as the rapidity of the most forward generated particle with an $E_T$ above 400 MeV, (excluding the scattered proton for the diffractive Monte Carlos), for three diffractive Monte Carlos, and for a standard–DIS model, CDM. For standard–DIS, the $\eta^{\rm gen}_{\rm max}$ is always close to the proton beam direction: this is a simple statement of the presence of a proton remnant. For the diffractive

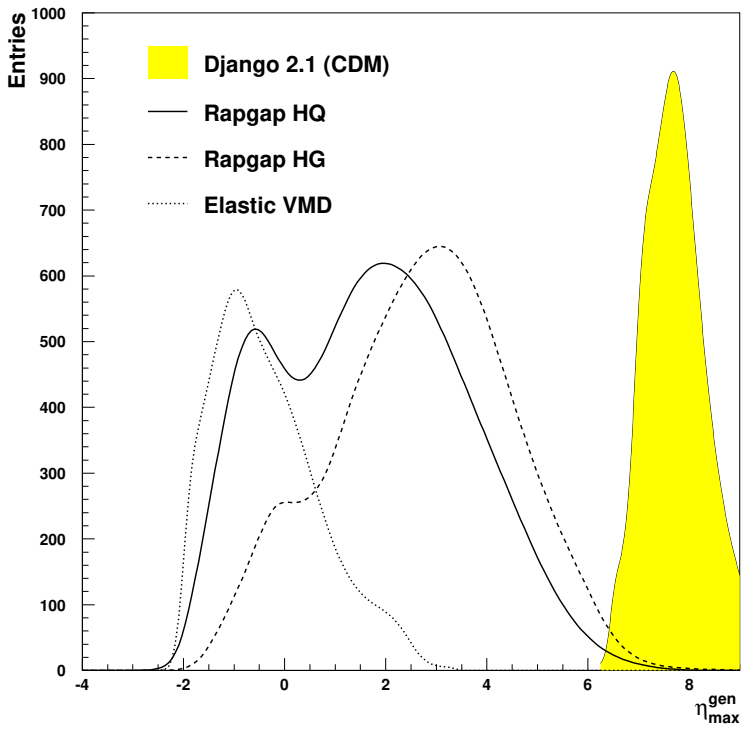


Figure 5.9: Distribution of $\eta_{\rm max}^{\rm gen}$ for diffractive and non-diffractive Monte Carlos. The distributions contain Monte Carlo data integrated over the kinematic range $7.5 \leq Q^2 \leq 80\,{\rm GeV}^2$ and $10^{-4} \leq x \leq 10^{-1}$.

Monte Carlos, a significant proportion of the events have values of $\eta_{\rm max}^{\rm gen} > 3.6$, that is outside of the LAC. For an event with $\eta_{\rm max}^{\rm gen} = 3.6$, there is a rapidity gap extending from the scattered proton to the edge of the LAC, a gap of almost 5 units in rapidity. Despite the presence of such a large rapidity gap, such an event could not be identified as a candidate for diffraction by any $\eta_{\rm max}$ selection based on the LAC.

### 5.4.1 The Forward Detectors

An alternative method of identifying diffractive events has been developed using detectors in the forward region of H1 [68, 69]. The essential idea is that particles at very high values of $\eta$, which are beyond the geometric acceptance of the LAC, can collide with dead material in the forward region, for example, collimators in the beam pipe or the beam pipe itself, and scatter at large angles depositing energy

in the forward region of H1. This effect can be discerned on close re-examination of figure 5.1. For the standard–DIS event (top) there is significant activity in the forward region outside of the LAC: "hits" are reconstructed in the Forward Muon Detector (section 3.5.2), energy is observed in the Plug calorimeter (section 3.3.3), and some energy deposition is also seen in the Instrumented Iron (section 3.5.1). This activity is in stark contrast to the large rapidity gap event (bottom), in which all of the forward detectors mentioned above are conspicuously absent of any signal inconsistent with electronic noise. A similar correlation between large rapidity gaps in the LAC and a lack of forward activity is found in the proton remnant tagger ($P_{TAG}$).

Studies have shown that the $P_{TAG}$, FMD and PLUG calorimeter are sensitive to secondary scatters of particles originating from the event vertex with values of $\eta$ between 3.5 and 8 [69]. The effective coverage in $\eta$ of each of the forward detectors is illustrated in figure 5.10c, where the probability of a particle from the interaction point being detected in each of the forward detectors is shown as a function of the rapidity of the particle. There is considerable overlap in the ranges of $\eta$ covered, allowing the efficiencies of each detector to be extracted directly from the data [69]. The significance of the ability to use these detectors to measure activity in the $\eta$ range $3.6 < \eta < 8$ can be seen in figures 5.10a and 5.10b, which show the energy flow and particle multiplicities as a function of $\eta$ for diffractive and non-diffractive DIS Monte Carlos. It is precisely in the range covered by the forward detectors that the difference between the diffractive events and the non-diffractive background is most pronounced. While CDM produces substantial energy flow in this region, RAPGAP produces almost none. In addition, the effect of proton dissociation in diffraction, as implemented in RAPGAP, is manifest as a slight increase in activity in the region of the proton remnant tagger, and at the edge of the region covered by the forward muon detector. This suggests that use of these forward detectors may allow an estimate of the level of such dissociation in the sample to be made.

Before any detector component can be used for quantitative physics analysis, evidence is necessary that the behavior of the component is adequately described by the detector simulation, otherwise corrections for inefficiencies and acceptance effects are impossible. This requirement is particularly appropriate for these

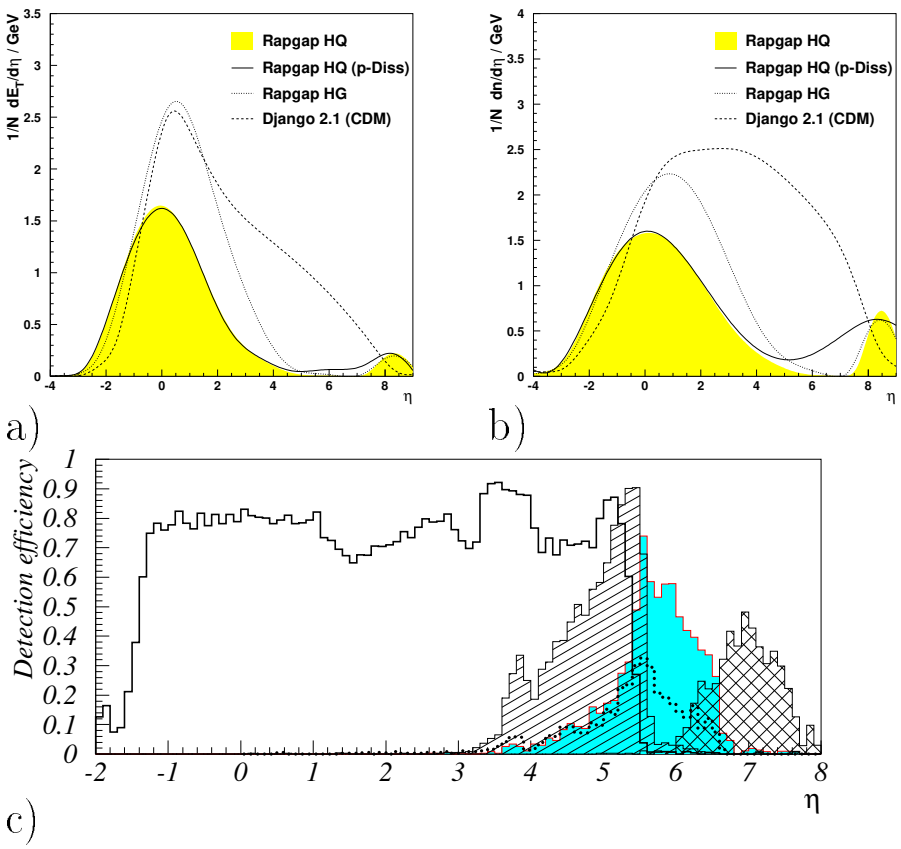


Figure 5.10: a) Particle multiplicities for diffractive and non-diffractive Monte Carlo events as a function of $\eta$. b) Energy flow per unit rapidity for diffractive and non-diffractive Monte Carlo events as a function of $\eta$. c) Single particle detection efficiency for the different detectors used to select LRG events. Solid line: LAC, shaded: FMD, hatched: PLUG, cross-hatched: $P_{TAG}$, dotted: Iron (not used).

forward detectors, for which sensitivity to secondary scatters from the beam pipe was not a primary design constraint. To establish that the responses of the detectors in the data are well reproduced by the simulation, it is necessary to address the problem that the data comprise an unknown admixture of diffraction and standard–DIS, and so in general the response of the detectors will only be reproduced by a mixture of diffractive and standard–DIS Monte Carlo events. This problem can be countered by using the LAC $\eta_{\max}$ selection to anti–select diffractive events. Figure 5.11 shows the activity in the plug, forward muon detector and proton remnant tagger for DIS data and Monte Carlo after the selection $\eta_{\max} > 3.2$ is applied. The $\eta_{\max}$ distribution (figure 5.7) suggests that

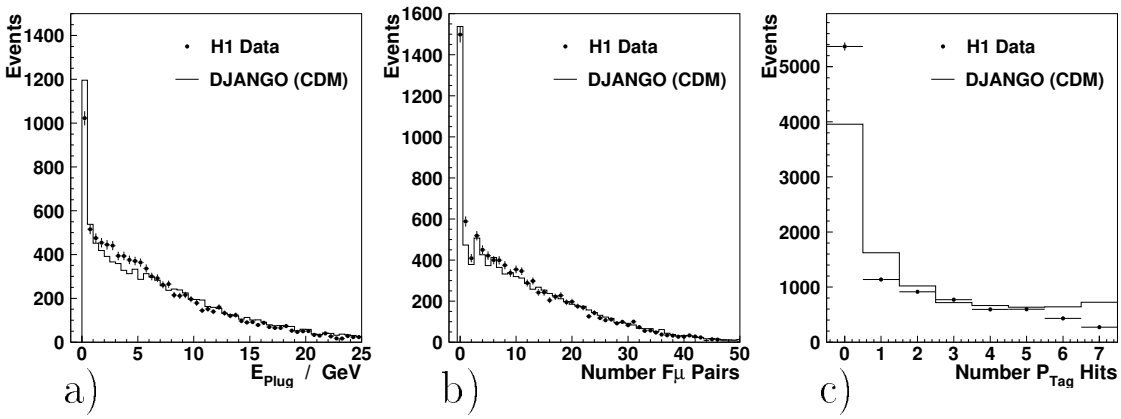


Figure 5.11: The signals in the forward detectors for data with $\eta_{\max} > 3.2$ compared with CDM Monte Carlo simulation. a) PLUG, b) FMD, c) $P_{TAG}$.

any contribution from diffraction should be reduced to $1-2\%$. The data are seen to be in excellent agreement with the Monte Carlo[1], except for the $P_{TAG}$ where some discrepancy is observed.

### 5.4.2 Using of the Forward Detector to Select Diffraction

The potential power of these detectors to select diffractive events can be seen graphically in 5.10: diffractive Monte Carlos predict essentially no activity in any of these detectors[2] whilst the activity predicted by the standard–DIS Monte Carlos is large. A powerful selection for diffraction is possible by using these detectors to veto normal DIS events. The way in which the forward detectors may be used, alone or in combination with an $\eta_{\max}$ cut, is discussed in the remainder of this chapter. Several alternative prescriptions are presented, and the relative merits of each discussed in terms of the efficiency for selecting diffraction, and

[1] Agreement for the Plug calorimeter is only achieved after a rescaling of the Monte Carlo energy by a factor 0.6. It is not surprising that a scale factor is needed for the plug, as no test beam calibration was performed. Indeed, this rescaling constitutes the first calibration of this device. An identical scale factor is found after the analysis of photoproduction data in a similar manner [67].

[2] This is not quite true. Diffractive events with a sufficiently high mass may produce no rapidity gap at all, and will always remain indistinguishable from DIS. In addition, diffractive events with proton dissociation may produce activity in the proton remnant tagger and the forward muon detectors.

the efficiency for rejecting conventional DIS.

Finally some results of the use of these selections to isolate diffractive events for analysis are presented.

### 5.4.3 Alternative Selection Prescriptions

A more detailed analysis of the forward detectors, and the degree of systematic uncertainty associated with their use in diffractive event selection is presented elsewhere [69]. In this section the performance of the forward detectors, used in isolation and in conjunction with an $\eta_{\max}$ selection to select diffractive events, is compared with other selections. The primary consideration in constructing a selection using the forward detectors is to maximise the efficiency for rejecting conventional DIS, whilst minimising the loss of diffractive candidates due to detector noise.

Four different selection methods are discussed, all of which centre on the basic requirement of a large rapidity gap, albeit in different parts of the detector.

#### The $\eta_{\max}$ Selection

As described in section 5.2 a requirement of $\eta_{\max} < 1.8$ is used.

#### The FA Selection

A selection based entirely upon the forward detectors, a coincidence of no activity in the Plug Calorimeter, the Forward Muon Detector, and the Proton Remnant Tagger is required such that:

1. the number of reconstructed track segments in the forward muon detector is less than 2
2. the total energy in the PLUG is less than 1 GeV

3. the total number of hits in the proton tagger is 0 for data, or less than 2 for Monte Carlo

The different requirement for Monte Carlo and data for the Proton Remnant Tagger is introduced to account for the small discrepancy between the efficiency observed in the data and Monte Carlo, visible as the difference in figure 5.11c. Some difference is expected here as the beam pipe and local dead material are not fully included in the detector simulation as yet. For discussion of this point the reader is referred to [69].

### The FB Selection

The forward detectors, excluding the Proton Remnant Tagger, are used in conjunction with a less strict $\eta_{\max}$ requirement such that:

1. the number of reconstructed track segment in the FMD is less than 2
2. the total energy in the PLUG is less than 1 GeV
3. $\eta_{\max} < 3.2$

### The ZEUS Selection

A different approach to the limitations of a strict $\eta_{\max}$ selection has been investigated by the ZEUS Collaboration [70]. They argue that the lack of colour connection between the diffractive mass and the scattered proton in diffractive events should be manifest in a different energy flow profile for the diffractive contribution, such that hadronic activity is more concentrated around the current jet direction. An event shape variable, $\alpha_{had}$ is formed from the momentum vector of the hadronic final state, such that

$$\alpha_{had} = \frac{P_z}{|\mathbf{P}|} \tag{5.2}$$

where $\mathbf{P}$ is the momentum vector of the hadronic final state, and $P_Z$ the component of $\mathbf{P}$ parallel to the $z$ axis. For DIS events, $\alpha_{had}$ is observed to be peaked at

1, with the diffractive Monte Carlos producing events predominantly in the tail of the distribution. They define a diffractive candidate by requiring:

1. $\alpha_{had} < 0.75$
2. $\eta_{\max} < 3$

### 5.4.4 Performance of the Diffractive Selections

The efficiency for selecting diffractive events of each of the four selections is shown in figure 5.12 as a function of $x$, $M_X$, $x_{I\!P}$ and $Q^2$. The efficiencies were evaluated using RAPGAP with a hard quark structure function (HQ). All of the selections are efficient at low $x$. This is because the direction of the current jet moves towards the backward direction of H1 as $x$ decreases, away from the region in which the rapidity gap is requested. The interaction of the dynamics of the diffractive events with the different selections is most apparent when studied in terms of $x_{I\!P}$. The efficiency of the $\eta_{\max}$ selection is seen to fall rapidly to near zero for $x_{I\!P} > 10^{-2}$. This is a manifestation of the strong correlation between $x_{I\!P}$ and the minimum size of the rapidity gap between the scattered proton and diffractive mass (section 2.9.2). As $x_{I\!P}$ increases, the rapidity gap no longer extends beyond $\eta_{\max} = 1.8$, and so the efficiency drops to zero. The **FA** and **FB** selections retain a high efficiency for for $x_{I\!P} > 10^{-2}$. This is because a rapidity gap is required at higher $\eta$, such that the diffractive mass remains outside the region required to be free of energy deposition until higher values of $x_{I\!P}$. The ZEUS selection ($\alpha$) represents a slight improvement over an $\eta_{\max}$ selection in terms of efficiency.

The efficiency of all of the selections decreases as $M_X$ increases. This is because higher values of $M_X$ are correlated with higher values of $x_{I\!P}$, and the size of the rapidity gap decreases as $x_{I\!P}$ increases (equation 2.29). This can also be understood in simple dynamical terms: larger masses are spread over a larger region of the detector, and will thus be less likely to be associated with a large rapidity gap. The $Q^2$ dependences of the selection efficiencies are less pronounced as a wide range of $x_{I\!P}$ and $M_X$ are accessible for each $Q^2$.

In addition to considering the efficiencies of each selection, the degree to which

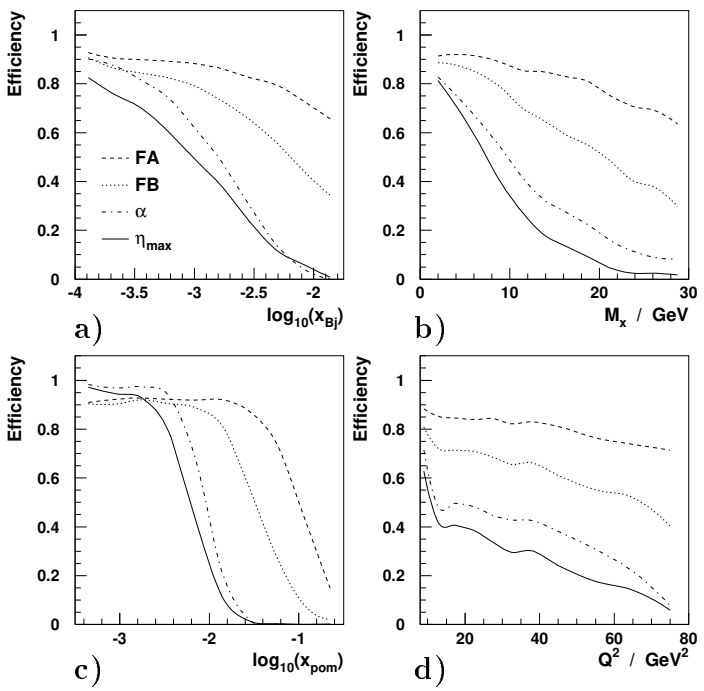


Figure 5.12: The efficiencies for selectind diffractive events of the four selection techniques. The efficiency is defined to be the fraction of RAPGAP HQ events selected from the low $Q^2$ DIS selection described in the previous chapter. This efficiency is plotted as a function of the generated values of $x$, $M_X$, $x_{I\!P}$ and $Q^2$ to avoid the introduction of additional effects due to finite resolution. Refer to the text for explanation of the selections.

background from normal DIS is controlled must be considered vital. Figure 5.13 shows the $x_{I\!P}$ distribution obtained from applying each of the four selections to the low $Q^2$ data, and the estimated backgrounds from the Colour Dipole and Matrix Element + Parton Shower models. The Monte Carlo background is normalised to the data in the region $\eta_{\max} > 3.3$, where the relative contribution from diffraction is negligible. Table 5.1 shows the predicted background for each sample as a percentage of the selected data. The $\eta_{\max}$ selection (figure 5.13a) is not strongly sensitive to the background; the $x_{I\!P}$ range is limited to $x_{I\!P} < 10^{-2}$. The selections using the forward detectors (figures 5.13b and 5.13c) reach higher values of $x_{I\!P}$, and although this is achieved only at the expense of higher background, the

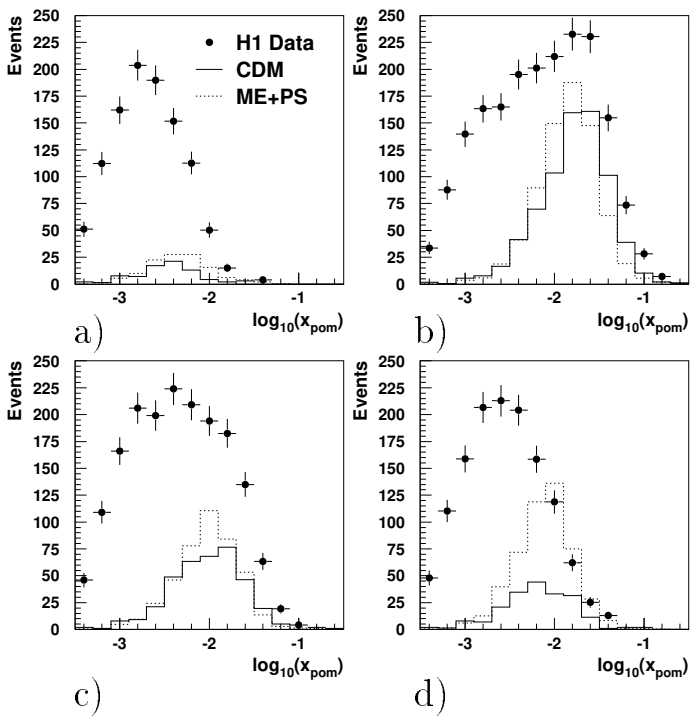


Figure 5.13: The amount of background from normal DIS allowed by the different selections: a) $\eta_{\max}$, b) **FA**, c) **FB**, d) $\alpha$. The colour dipole model and MEPS hadronisation models are used to estimate the degree of uncertainty in the level of background. The DIS Monte Carlos are normalised to the data in the region $\eta_{\max} > 3.3$, in which the contribution from normal DIS dominates.

sensitivity to different models of hadronisation is not strong (table 5.1). The $\alpha$ selection is seen to be more sensitive to different hadronisation models (figure 5.13d), with the background for MEPS more than twice that for CDM.

The different selection methods have different properties, linked to the different regions in which a rapidity gap is required. One conclusion that can be drawn is that the requirement of a rapidity gap is relatively insensitive to the choice of hadronisation model, where as a selection using information on the detailed profile of the energy flow, such as the $\alpha$ selection is. In addition to the problem of uncertainty in the remaining DIS background, such a selection also forces the selected data to resemble a preconception of what the diffractive data

| Selection | Model | |
|---|---|---|
| | **CDM** | **ME+PS** |
| $\eta_{\max}$ | 7% | 12% |
| FA | 37% | 38% |
| FB | 21% | 24% |
| $\alpha$ | 15% | 38% |

Table 5.1: The background (% of sample selected) from standard–DIS for each selection

should look like, in that events will only be selected if the energy flow is more concentrated around the current jet direction than for standard–DIS.

No single selection can satisfy the requirements of all types of physics analysis: where diffractive data are required with minimal background, then in the absence of tagging the scattered proton a severe rapidity gap selection is unavoidable. If the analysis is to consider as much of the kinematic phase space as possible, then a statistical subtraction of a significant background from standard–DIS is inevitable. In the remainder of this chapter we examine the H1 diffractive data using the **FA**, **FB** and $\eta_{\max}$ selections and compare the data with partonic models of electron–pomeron scattering.

### 5.4.5 Kinematic Comparisons

The data obtained with the $\eta_{\max}$, **FB** and **FA** selections are compared in terms of $\beta$, $M_X$, $\eta_{\max}$ and $x$ in figures 5.14 to 5.16. In each figure the left hand plots show the distributions of selected events along with the estimated background from conventional DIS. The right hand plots show the same distributions after subtraction of the background, along with the estimated systematic uncertainty introduced by this subtraction.

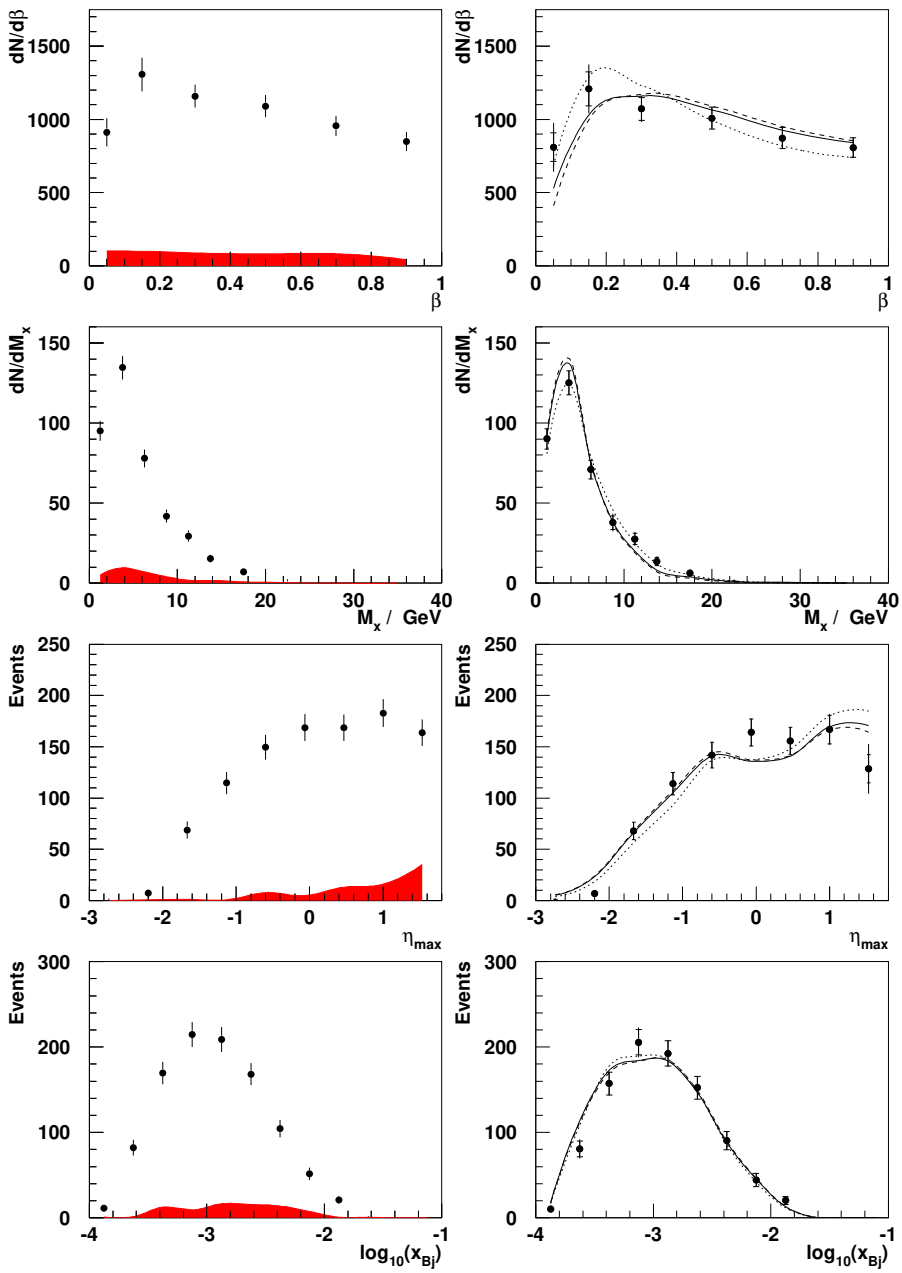


Figure 5.14: Comparison of those data obtained with the $\eta_{\max}$ selection (see text) with Monte Carlo. Left: selected data with predicted standard–DIS background from the CDM model. Right: selected data after the subtraction of the aforementioned background, compared to the following different diffractive Monte Carlo mixtures: HQ (dashed line), HQ+HG (dotted line), HQ+SG (solid line). The data are shown as a function of (top to bottom) $\beta$, $M_X$, $\eta_{max}$, and Bjorken–$x$.

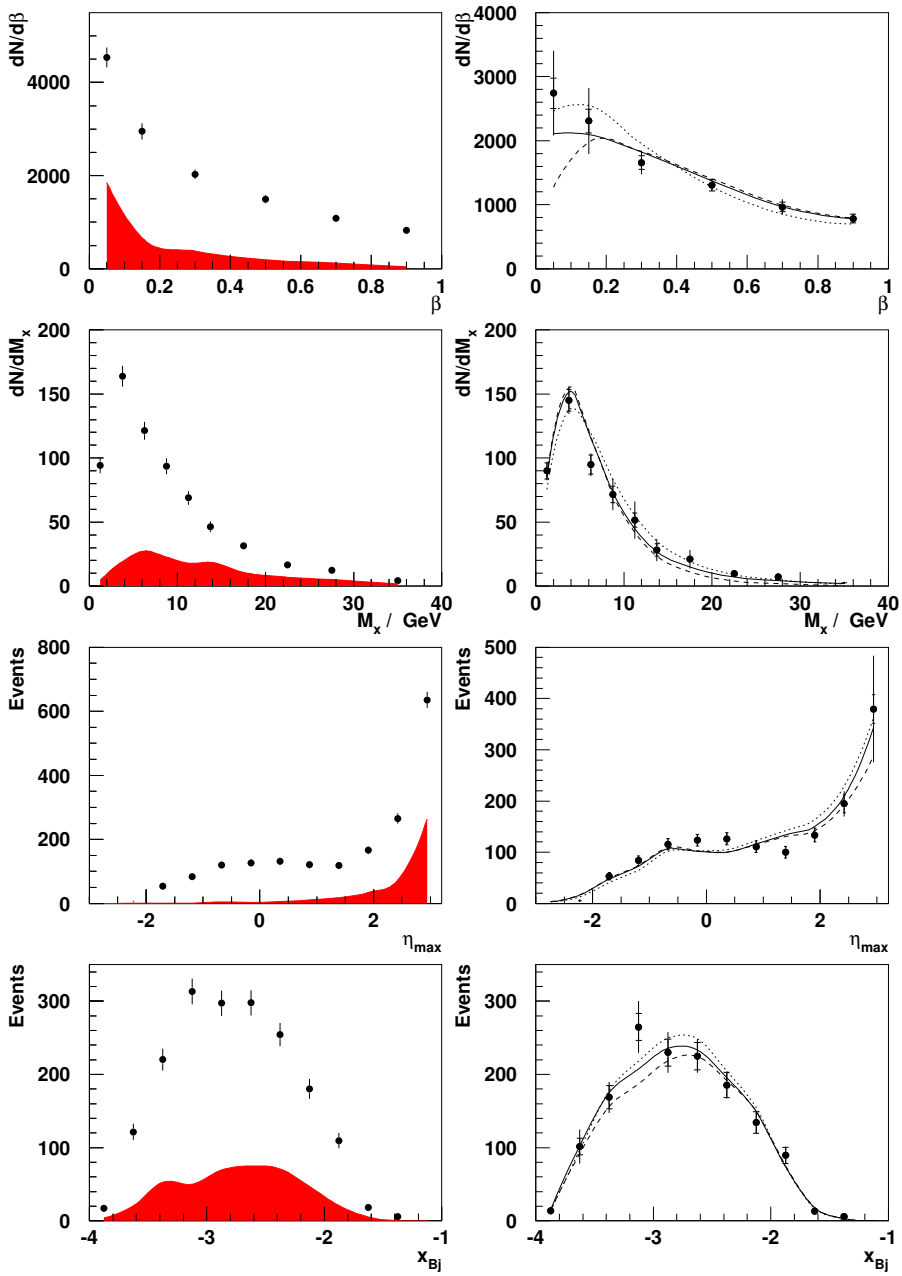


Figure 5.15: Comparison of those data obtained with the **FB** selection (see text) with Monte Carlo. Left: selected data with predicted standard–DIS background from the CDM model. Right: selected data after the subtraction of the aforementioned background, compared to the following different diffractive Monte Carlo mixtures: HQ (dashed line), HQ+HG (dotted line), HQ+SG (solid line). The data are shown as a function of (top to bottom) $\beta$, $M_X$, $\eta_{max}$, and Bjorken–$x$.

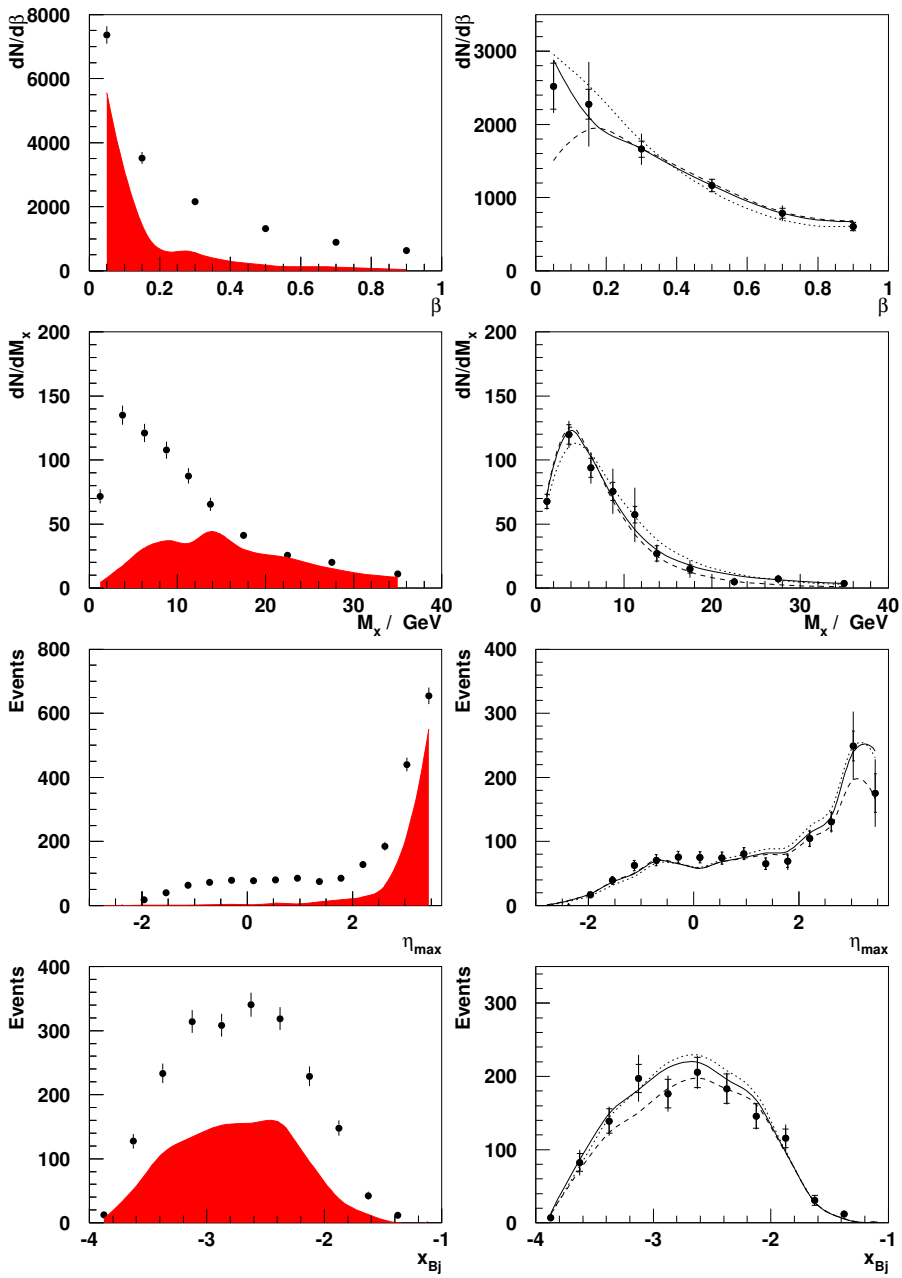


Figure 5.16: Comparison of those data obtained with the **FA** selection (see text) with Monte Carlo. Left: selected data with predicted standard–DIS background from the CDM model. Right: selected data after the subtraction of the aforementioned background, compared to the following different diffractive Monte Carlo mixtures: HQ (dashed line), HQ+HG (dotted line), HQ+SG (solid line). The data are shown as a function of (top to bottom) $\beta$, $M_X$, $\eta_{max}$, and Bjorken–$x$.

| MC Mixture | HQ | HQ+HG | HQ+SG |
|---|---|---|---|
| % Elastic VMD ($\eta_{\max} < 1.8$) | 10 | 10 | 10 |
| % Hard Quark ($\eta_{\max} < 1.8$) | 90 | 63 | 87.3 |
| % Hard Gluon ($\eta_{\max} < 1.8$) | 0 | 27 | 0 |
| % Soft Gluon ($\eta_{\max} < 1.8$) | 0 | 0 | 2.7 |
| % Elastic VMD (Kin. Reg.) | 6.5 | 5.6 | 5.3 |
| % Hard Quark (Kin. Reg.) | 93.5 | 55.3 | 72.8 |
| % Hard Gluon (Kin. Reg.) | 0 | 39.1 | 0 |
| % Soft Gluon (Kin. Reg.) | 0 | 0 | 21.9 |
| Fraction of Total (Kin. Reg.) | 11.3 | 13.2 | 14.0 |

Table 5.2: The Monte Carlo mixtures used to describe the data. The mixtures are specified in terms of the contribution to the $\eta_{\max}$ sample, and the resulting contributions to the kinematic regime $Q^2 > 7.5$, $y < 0.6$ and $x < 10^{-2}$ are also displayed. The predictions from each mixture for the total contribution of diffraction are also given for this region (see text.)

The data are compared with three diffractive Monte Carlo mixtures, referred to as HQ, HQ+HG, and HQ+SG. These are specified in table 5.2. The mixtures are specified in terms of the fraction of events from each process contributing to the $\eta_{\max} < 1.8$ sample, and the normalisation is taken from the requirement that the Monte Carlo reproduce the excess of events with $\eta_{\max} < 1.8$ (figure 5.14). The same normalisation is then used in comparisons with the data in the samples obtained with the **FB** and **FA** selections (figures 5.15 and 5.16 respectively).

The data in the $\eta_{\max}$ sample are well described by a hard parton density, $\beta q_0 \propto \beta(1-\beta)$. Some small discrepancy at very low values of $\beta$ is visible, and the description may be improved by the addition of a softer component, here modelled with a gluonic component to the pomeron, although there is no strong justification for such a component.

The same Monte Carlo models also describe well the distributions obtained with the **FB** and **FA** selections, after corrections for proton dissociation are applied, giving confidence that the larger level of background from standard–DIS in these sample is controlled. The evidence for an excess in the data over the expectations of a hard pomeron parton distribution is stronger for these sample

due to the enhanced efficiencies of these selections for low values of $\beta$. The effect on the total contribution from diffraction of a possible soft component is shown in table 5.2, where the prediction from each Monte Carlo mixture for kinematic region $Q^2 > 7.5\,\mathrm{GeV}^2$, $y < 0.6$ and $x < 10^{-2}$ is given. Whilst the hard component alone predicts that $\approx 11\%$ of all DIS in this region is diffractive, the inclusion of a softer component increases this estimate to $\approx 13 - 14\%$.

### 5.4.6 Energy Flow Comparisons

Further information about the structure of the pomeron may be provided by analysis of the energy flow in diffractive events. Figure 5.17 shows the transverse energy flow ($E_T$) per unit rapidity in the lab system, for two bins in $x$. The **FB** selection is used, allowing the LAC to be used up to $\eta = 3$ whilst minimising the background from standard–DIS. The RAPGAP Hard Quark Monte Carlo describes both the level and shape of the energy flow distributions well, although for $x < 10^{-3}$ the energy flow in the data is somewhat above this prediction. Both of the two gluon models predict a significantly higher energy flow than is observed in the data. By adding varying mixtures of the gluon components to the Hard Quark Monte Carlo, it is found that components larger than those described in table 5.2 are inconsistent with the data, and that these phenomenological mixtures developed to describe the kinematic distributions also describe the energy flow data. It is worth remarking that the RAPGAP Monte Carlo has not been tuned to describe the data in any way.

## 5.5 Summary

In this chapter it has been shown that the Large Rapidity Gap events observed in deep–inelastic scattering at HERA by the ZEUS and H1 experiment cannot be attributed to either non $ep$ backgrounds, or fluctuations in the hadronisation in standard models of DIS. It is found that they may be explained by a partonic model of electron-pomeron physics: that is deep inelastic hard diffractive scattering, in which the scattering off a colourless component of the proton leads naturally to large rapidity gaps. Such a picture can explain all of the charac-

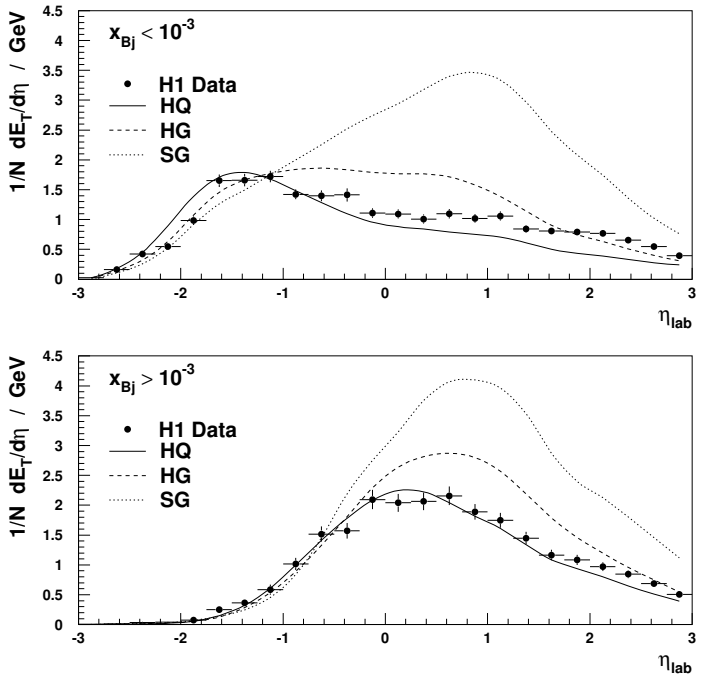


Figure 5.17: Transverse energy flow per event per unit rapidity for data obtained with the **FB** selection for two regions of $x$, uncorrected for acceptance. The predictions from the three different RAPGAP components are shown: Hard Quark (HQ), Hard Gluon (HG), and Soft Gluon (SG), where in each case the estimated contribution from standard–DIS background is added.

teristics of the LRG events studied, and if the ansätze of this model are correct, then some conclusions can be drawn about the partonic nature of the pomeron. A hard parton density is strongly favoured, although there is some suggestion of a softer component. Given the limited freedom to include softer components into a model that can describe the data, estimates have been made of the likely total contribution from diffraction to DIS, and found to vary between 11 and 14%.

These estimates do not constitute a precise determination of the total contribution from diffraction, nor does the good agreement with diffractive Monte Carlos confirm that the origin of the Large Rapidity Gap events is diffractive in nature.

The fact that a hard parton density of quarks can well describe most aspects

of the data does not imply that the pomeron is primarily composed of quarks. If the pomeron were composed of gluons at some initial scale, $Q_0^2$, then evolution to some higher scale, $Q^2 > Q_0^2$ would result inevitably in some quark component. Furthermore, the lowest order process in DIS is scattering from a quark and the scattering can only involve a gluon through a boson-gluon fusion loop, a second order process.

The phenomenological models developed in this chapter to describe the data may be used to correct for the acceptances of the different selections such that fully corrected cross sections may be determined. The determination of the cross sections for diffraction in DIS is the subject of the remainder of this work, where it is shown that the characteristics of these cross sections demonstrate unambiguously that the Large Rapidity Gap events are produced by deep–inelastic diffractive scattering.

# Chapter 6

# The Diffractive Structure Function $F_2^D(x, Q^2)$ for $x_{I\!P} \leq 0.01$

## 6.1 Introduction

In the previous chapter it is argued that the Large Rapidity Gap events observed in the H1 data from HERA may be explained by a diffractive component to the deep–inelastic scattering cross section. It is shown that, under the assumption that these events are of a diffractive origin, a sample of diffractive events may be selected with a high efficiency, and with a low background remaining from non–diffractive processes, by the criterion $\eta_{\max} < 1.8$. This selection, however, restricts the sample to those events with $x_{I\!P} < 0.01$.

The subject of this chapter is the extraction of the cross section for diffraction in deep–inelastic $e$–$p$ scattering in the kinematic region $x_{I\!P} < 0.01$. Following Ingelman and Schlein [17], this cross section is expressed as a "diffractive structure function", $F_2^D(x, Q^2)$. Aside from the aesthetic attraction of removing the steep dependence on $Q^2$ associated with the photon flux terms (equation 2.18), this transformation of the cross section facilitates direct comparison with the inclusive proton structure function, such that the contribution of diffraction to $F_2(x, Q^2)$ may be seen directly, and the extent to which it plays a role in the new physics at low $x$ evaluated.

In section 6.2 the diffractive structure function to be measured is defined,

and in section 6.3 an overview of the components of the analysis necessary to arrive at $F_2^D(x,Q^2)$ is given. Discussions of the event selection, subtraction of backgrounds, and the evaluation of the systematic uncertainties follow before the results are presented in section 6.5. The measurements are compared with theoretical calculations in section 6.6, and the chapter closes with a summary.

## 6.2 The Definition of $F_2^D(x,Q^2)$

The diffractive structure function, $\mathbf{F}_2^D(x,Q^2,x_{I\!P},t)$ is defined in section 2.9.3. In the absence of any apparatus to measure the momentum of the colourless remnant, that is the scattered proton or its decay products in the case in which the proton dissociates, the measured cross section $\frac{d^3\sigma(ep\to epX)}{dxdQ^2dx_{I\!P}}$ amounts to the determination of $\int_t \mathbf{F}_2^D(x,Q^2,x_{I\!P},t)\,dt$.

To evaluate the contribution of diffraction in the region $x_{I\!P} \leq 0.01$ to the proton structure function at a given $(x,Q^2)$ requires the calculation of

$$F_2^D(x,Q^2)\Big|_{x_{I\!P}\leq 0.01} = \int_x^{0.01}\int_{t_{min}}^{t_{max}} \mathbf{F_2^D}(x,Q^2,x_{I\!P},t)\,dt\,dx_{I\!P} \tag{6.1}$$

Note that the lower limit for the integration over $x_{I\!P}$ is $x$ since $x = \beta \cdot x_{I\!P}$ and $0 \leq \beta \leq 1$ and so $x_{I\!P} \geq x$. The relationship between the exclusive diffractive cross section $\frac{d^2\sigma^D(ep\to epX)}{dxdQ^2}$ and $F_2^D(x,Q^2)$ is identical to that between inclusive cross section $\frac{d^2\sigma(ep\to eX)}{dxdQ^2}$ and $F_2(x,Q^2)$:

$$\frac{d^2\sigma^D(ep\to epX)}{dxdQ^2} = \kappa(x,Q^2)\cdot F_2^D(x,Q^2) \tag{6.2}$$

where

$$\kappa(x,Q^2) = \frac{2\pi\alpha^2}{xQ^4}\left[2(1-y)+y^2\right] \tag{6.3}$$

and so the results obtained may be translated directly into a cross section if so desired.

The limit $x_{I\!P} < 0.01$ enforced by the selection $\eta_{\max} < 1.8$ is associated with the kinematic relationship between the $x_{I\!P}$ and the minimum size of the rapidity gap between the colourless remnant and the rest of the hadronic final state (equation 2.29). That this limit, expected at the parton level, is retained after

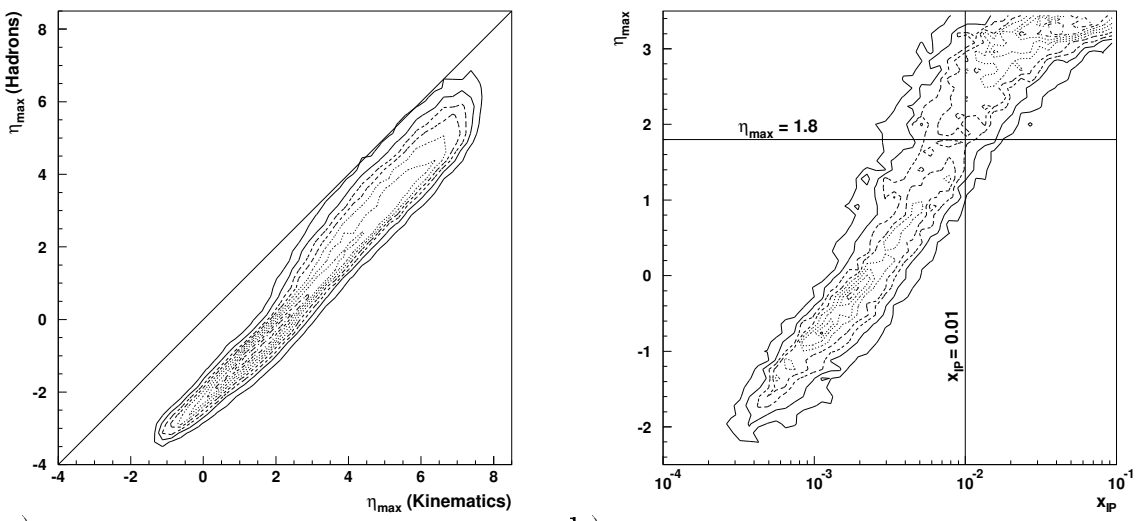


a) b)

Figure 6.1: a) The relationship between the kinematic expectation for the minimum size of the rapidity gap, $\eta_{\max}$(Kinematics), and the size of the $\eta_{\max}$(Hadrons). b) The correlation between the observed $\eta_{\max}$ in the H1 detector and the generated value of $x_{I\!P}$.

hadronisation is demonstrated in figure 6.1a), where the correlation between the $\eta$ of the particle closing the rapidity gap, $\eta_{\max}$(Hadrons), and the value expected from the value of $x_{I\!P}$ based on equation 2.29, $\eta_{\max}$(Kinematics) is shown. This correlation is observed, independent of the particular choice of model. The consequent correlation between the $\eta_{\max}$ as measured in the H1 detector (where $\eta_{\max}$ is defined in section 5.4.3) and $x_{I\!P}$ is shown in figure 6.1b).

To evaluate $F_2^D(x,Q^2)\Big|_{x_{I\!P} \leq 0.01}$, two different selections are used:

1. $\eta_{\max} \leq 1.8$
2. **FB** + $(x_{I\!P}^{rec} \leq 0.01)$

where the **FB** selection is defined in section 5.4.3, and $x_{I\!P}^{rec}$ is calculated from

$$x_{I\!P} = \frac{x}{\beta} = x \cdot \left(1 + \frac{M_X^2}{Q^2}\right) \tag{6.4}$$

The calculation using the first selection involves a correction, based on Monte Carlo, for those events that have $x_{I\!P} < 0.01$, but which have $\eta_{\max} > 1.8$ (those in the top left region of figure 6.1b.). The range in $x_{I\!P}$ accessible with the **FB** selection extends well above 0.01 (figure 5.15), and so the requirement on $x_{I\!P}^{rec}$ is introduced. When the second selection is employed, these events are retained, and so a quite different correction is involved, which is dominated by the finite resolution of $x_{I\!P}^{rec}$. The complementary nature of the two selections allow, therefore, an independent cross check of the former by the latter.

## 6.3 The Determination of $F_2^D(x,Q^2)$

DIS events are selected according to the prescription described in chapter 4. Two samples of diffractive candidates are identified in this sample using the two complementary selections described in the previous section above. The extraction of $F_2^D(x,Q^2)\Big|_{x_{I\!P}\leq 0.01}$ from these events then follows a bin–by–bin approach in which the events are assigned to bins according to their position in the $(x,Q^2)$ plane, and an estimate made of the number of diffractive events with true values of $(x,Q^2)$ within the boundaries of each bin with the aid of Monte Carlo simulation.

In order that the largest possible kinematic range may be covered, and to facilitate the study of systematics, both the electron–only and $\Sigma$ reconstruction methods described in section 4.3 are used. The binning used for each reconstruction method is shown in figure 6.2. The calculation of $F_2^D(x,Q^2)\Big|_{x_{I\!P}\leq 0.01}$ for each bin used in the analysis may be summarised by the following equation:

$$\tilde{F}_2^D \simeq \overbrace{\frac{N}{A_s \cdot \epsilon \cdot \mathcal{L}}}^{\mathbf{A}} \cdot \overbrace{\frac{\int_{bin} \sigma_0 \, dx dQ^2}{\int_{bin} \sigma \, dx dQ^2}}^{\mathbf{B}} \cdot \overbrace{\frac{\sigma_0}{\int_{bin} \sigma_0 \, dx dQ^2}}^{\mathbf{C}} \cdot \overbrace{\frac{1}{\kappa(x,Q^2;R)}}^{\mathbf{D}} \qquad (6.5)$$

where the four components of this equation, labelled **A**-**D** are outlined below:

**A** Conversion of the observed rate of events to an estimate of the true rate of events in the bin, corrected for all systematic effects. $N$ is the observed number of events in the bin after the subtraction of all backgrounds. $A_s$ is the acceptance determined from the Monte Carlo, and $\epsilon$ is a correction to account for additional

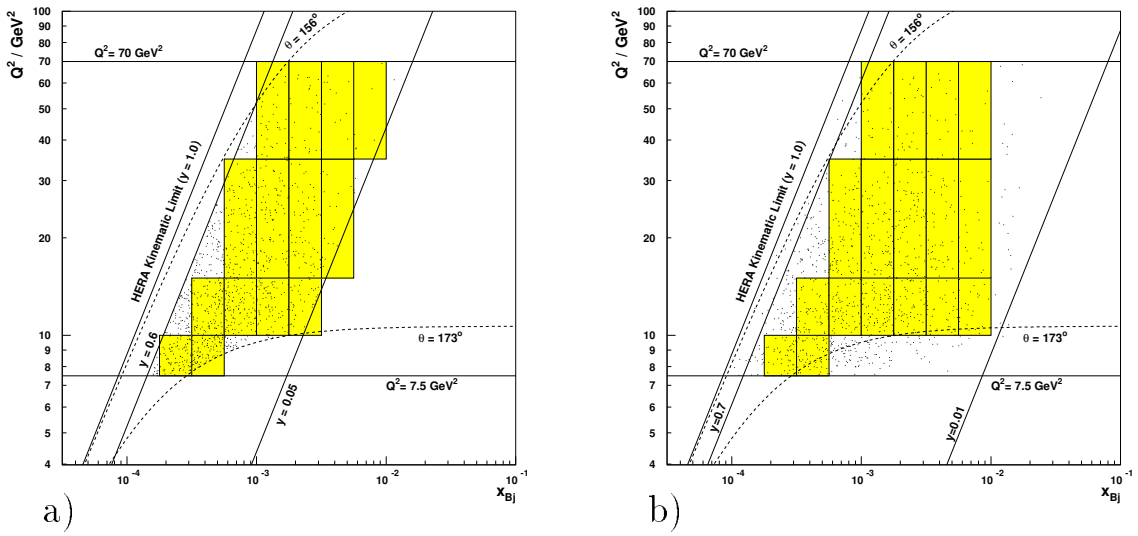


Figure 6.2: The selected Events and binning used for the electron (a) and $\Sigma$ (b) reconstruction methods. The $\eta_{\max}$ selection is used (see text).

inefficiencies observed in the data which are not described by the Monte Carlo. $\mathcal{L}$ is the luminosity.

**B** Higher order corrections to the single-photon exchange cross section, or "radiative corrections".

**C** Transformation of the bin orientated measurement to a value for the differential cross section at a prescribed value of $x$ and $Q^2$, "bin corrections".

**D** Kinematic factors to transform the measurement of the cross section into $F_2^D$ (equation 6.3).

The following sections describe these components in more detail.

### 6.3.1 Subtraction of Background

The number of events reconstructed in each bin must be corrected for the expected number of background events which survive all of the selection criteria.

Conventional backgrounds due to standard DIS physics are discussed in chapter 5. For diffractive DIS two additional backgrounds must be considered, namely background from conventional DIS and background from diffractive photoproduction. The background from conventional DIS is discussed in the previous chapter, and the same method of statistical subtraction is used here. The poten-

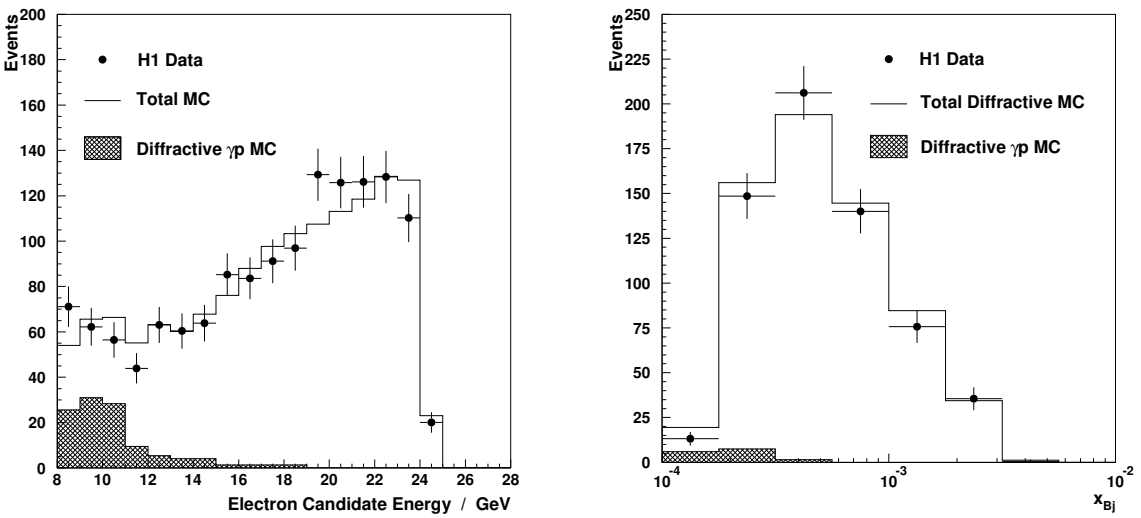


Figure 6.3: Distributions of a) electron candidate energy, and b) Bjorken–x for those data obtained with a DIS selection modified to study the background from photoproduction interactions (see text) together with the $\eta_{\max}$ selection. The data are compared with the predictions from a Monte Carlo (solid line) including both DIS and photoproduction processes (see text). The expected contribution from hard diffractive photoproduction alone is also shown (shaded).

tial background from diffractive photoproduction may be split into soft and hard components (section 2.10). Soft diffractive photoproduction was simulated with the RAYVDM code [41], and the remaining background found to be insignificant.

The background from hard diffractive photoproduction is studied using a sample of over 350000[1] events produced with the POMPYT [42] generator (section 2.11.3). The requirements in the data selection specifically designed to eliminate fake electron candidates are relaxed by making the modifications to the electron

[1]The cross section for hard diffractive photoproduction is not well known, but from the estimated cross section, this corresponds to approximately five times the data luminosity.

| Standard Selection | Photoproduction Selection |
|---|---|
| **ECRA** $\leq 4\,cm$ | **ECRA** $\leq 6\,cm$ |
| **DCLBP** $\leq 4\,cm$ | **DCLBP** $\leq 6\,cm$ |
| $Q^2 > 7.5\,\mathrm{GeV}^2$ | $Q^2 > 6\,\mathrm{GeV}^2$ |
| $E'_e > 10.6\,\mathrm{GeV}$ | $E'_e > 7.5\,\mathrm{GeV}$ |
| $\theta_e < 173^o$ | $\theta_e < 173.5^o$ |

Table 6.1: Modifications to the selection for photoproduction background studies

data selection detailed in table 6.1. Normalising the diffractive photoproduction Monte Carlo to the excess observed in the data with this modified selection over the prediction of the deep–inelastic diffractive Monte Carlos (normalisation as before in chapter 5) yields a good description of the rise in the energy spectrum of the electron candidates, shown in figure 6.3a). This method relies on the assumption that the kinematic distribution of both the DIS and $\gamma p$ diffractive components are well described by the Monte Carlos such that the normalisation of both may be fixed in this way.

This normalisation can be verified using those events in which an electron is found in the electron tagger. Genuine deep–inelastic events may also have an electron in this tagger if they are in coincidence with a Bethe-Heitler event, for which the rate is very high, and so the probability of overlap may not be neglected. Such events should also have a photon in the photon tagger, and so a total $E - P_Z$ consistent with two $ep$ collisions, not one. Following [60] these events are removed by selecting tagged events with the following criterion:

1. $\Sigma(E - P_Z) < 60\,\mathrm{GeV}$
2. $E_{etag} > 8\,\mathrm{GeV}$
3. $E_{\gamma tag} < 2\,\mathrm{GeV}$

in addition to the photoproduction selection described above. With this selection, 10 events are found in the data, and $11 \pm 3$ events are predicted by the diffractive photoproduction Monte Carlo, giving confidence that the normalisation is reasonable. With this normalisation, a contribution to the $\eta_{\max}$ sample of

1.2% is predicted. This background is confined entirely to $Q^2 \leq 16\,\mathrm{GeV}^2$, and to the lowest $x$ bins, rising to at most 4% in the lowest $x$ bins used in the analysis (figure 6.3b). A similar contribution is observed for the alternative selection using **FB**+($x_{I\!P}^{rec} < 0.01$).

### 6.3.2 Acceptance and Efficiency Corrections

The extraction of the true rate from the measured rate of events necessitates corrections for two effects:

- **Finite acceptance.** Geometrical acceptance, that is an incomplete geometrical coverage of the active detector components, will result in an incomplete coverage of phase space, and so a loss of events. In addition, the selection procedure may not identify all events due to limiting hardware efficiencies, or selections against background processes.
- **Finite resolution.** The resolution of the kinematic variables is limited by the finite resolution of the detector components involved. For example, the energy resolution of the BEMC and the angular resolution of the BPC will result in differences between the reconstructed $(x, Q^2)$ and the true values.

Corrections for geometrical acceptance effects are straightforward given precise knowledge of the physical structure of the detector, and the limited efficiencies of individual detector components may often be determined directly from the data. The evaluation of the efficiencies of composite selections used to isolate the signal and reject backgrounds usually requires detailed Monte Carlo studies such that correlations are correctly accounted for. For these evaluations to be trusted, the data must be well described by the Monte Carlo simulation.

The effects of finite resolution are more complicated. Deviations of the measured kinematic variables from the true values will result in 'migrations': if the data are binned, for example in bins of $x$, then some events will be assigned to the wrong bin. The net effect of events migrating in and out of each bin must be corrected for; the corrections must be done with care as the migrations will depend on the assumed form of the distribution of events across the bins. The

resolution in the measurement of $(x, Q^2)$ impose limits on the minimum bin size: if the bins are too small, the measurement in each bin becomes dominated by contributions from outside the bin, and the results become unstable. Typically, the determination of each variable in which the data are binned must be achieved with a resolution better than $\approx 70\%$ of the size of the bin. The resolution in $x$ and $Q^2$ as a function of the bin size is shown for the adopted binning in figure 6.4.

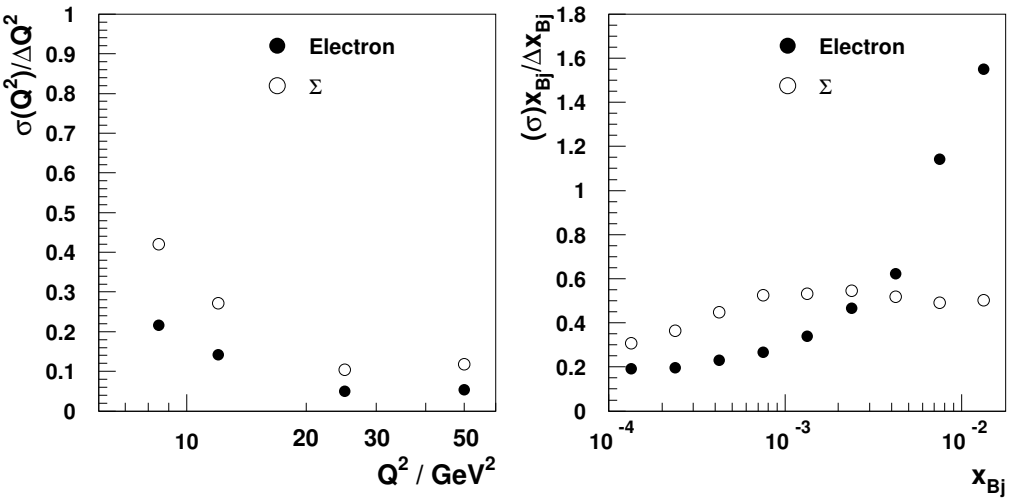


Figure 6.4: The resolution of the two kinematic methods use in the chosen binning. Note that not all of these bins are used in the analysis: for those that are used, the resolution in both $Q^2$ and $x$ is always less than 60% of the bin size.

The true number of events in each bin is estimated using the "smeared acceptance", $A_s$, determined from Monte Carlo, and defined

$$A_s = \frac{N^r}{N^g} \tag{6.6}$$

where $N^g$ is the number of events generated and $N^r$ the number of reconstructed events in that bin. To estimate the error on $A_s$, the contributions to $N^r$ from events that originated in that bin, $N^s$, must be separated from events that migrated into the bin from outside, $N^i$, where $N^r = N^s + N^i$. The error on $A_s$, $\sigma(A_s)$, can then be estimated by

$$\sigma(A_s) = \sqrt{\left(\frac{N^i}{N^g}\right)^2 \cdot \left(\frac{1}{N^g} + \frac{1}{N^i}\right) + \frac{1}{(N^g - 1)} \cdot \frac{N^s}{N^g} \cdot \left(1 - \frac{N^s}{N^g}\right)} \tag{6.7}$$

Confidence in the structure function extracted from the data in this way rests upon a good understanding of the aspects of the data used in the calculation. The excellent descriptions of the putative diffractive data selected with the $\eta_{\max} < 1.8$ and **FB** criteria by the Monte Carlo are shown in figures 5.14 and 5.15 respectively. That the former data are also well described in terms of the basic quantities measured by the detector, namely the energy and polar angle of the scattered electron, $y_\Sigma$, and $\eta_{\max}$ is shown in figure 6.5.

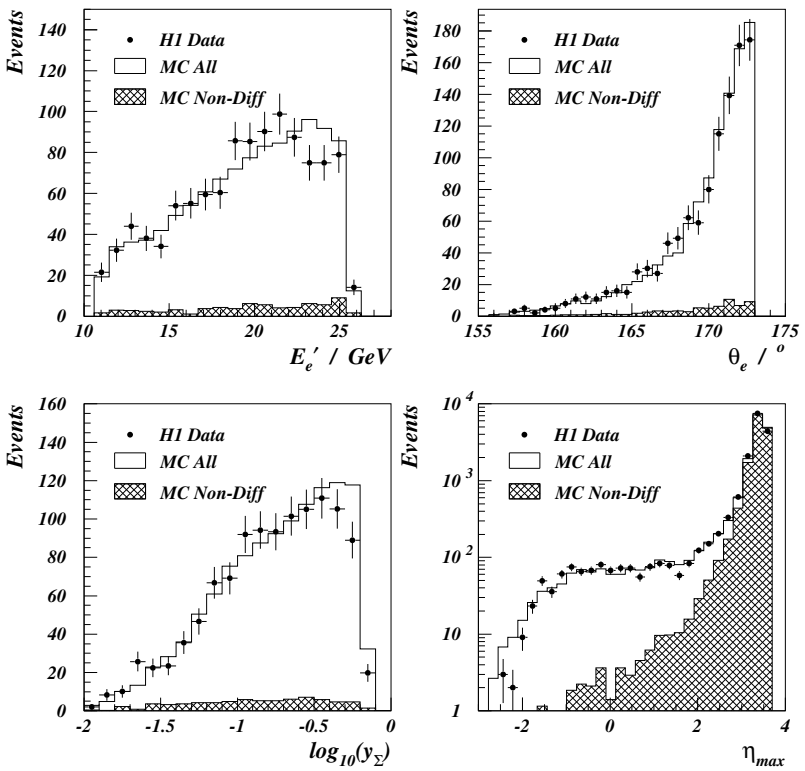


Figure 6.5: Distributions of quantities measured in H1 used for the extraction of the cross section. a) Electron energy, $E'$, b) electron scattering angle, $\theta$, c) y determined with the $\Sigma$ reconstruction method, d) $\eta_{\max}$. For a)-c) the requirement $\eta_{\max} < 1.8$ is imposed. The shaded histogram is the sum of the CDM and POMPYT Monte Carlos, the solid line is the sum of the former and the HQ, SG and VMD contributions.

### 6.3.3 Bin Corrections

To calculate the differential cross section at the specified bin centres, a correction factor is determined for each bin from the Monte Carlo. For a bin fully contained within the kinematic boundaries of all of the selection criteria, across which events are uniformly distributed, this correction amounts to the inverse of the bin area. Large deviations from this value only occur if the event population varies non–linearly across the bin, or if a large part of the bin is kinematically excluded.

### 6.3.4 Radiative Corrections

The higher order QED radiative corrections necessary to arrive at the Born cross section (term **B** in equation 6.5) were calculated using the RAPGAP generator which was interfaced using a recent version of ARIADNE [34] to the HERACLES package.

### 6.3.5 Remaining Factors

The value of $\kappa(x,Q^2)$ at each bin centre is calculated assuming $R^D = 0$. While $R^D$ is not known, if it is of the same magnitude as the value calculated using perturbative QCD for the proton, then the uncertainty introduced by this assumption only exceeds 1% at the lowest $x$ (highest $y$), rising to $\sim 5\%$ for $y = 0.5$. Furthermore, it is trivial to recalculate $F_2^D(x,Q^2)\Big|_{x_{I\!P} \leq 0.01}$ as soon as information on $R^D$ becomes available.

## 6.4 Systematic Errors

The potential sources of systematic uncertainty considered are summarised below, and the average contribution of these individual sources of uncertainty given as a percentage in parentheses where appropriate[2]

[2]The average contributions from each error refer to the final values for the structure function, that is the combination of the electron and $\Sigma$ methods.

- A potential mis–calibration of the BEMC by up to 1.7%, evaluated using the Monte Carlo mixture used to calculate the acceptances corrections. (5%)

- A shift of up to 2 mrad in the determination of the polar angle of the electron. (3%)

- A potential mis–calibration of up to 10% for the hadronic energy in the Liquid Argon Calorimeter. This only enters the calculation for the $\Sigma$ reconstruction method with the $\eta_{\max} < 1.8$ selection, but for both electron–only and $\Sigma$ methods for the **FB**+$x_{I\!P}^{rec}$ selection as $M_X$ is used to determine $x_{I\!P}^{rec}$ (12%).

- Uncertainties in the radiative corrections. For the $\Sigma$ method, the corrections are zero to within 3% [6]. For the electron method, an uncertainty of the full value of the correction applied is ascribed due to the uncertainties from the extrapolation to $Q^2 = 0$, the absence of second order corrections and soft photon exponentiation in the HERACLES Monte Carlo, and the dependence of the corrections on the assumed form of the structure function. A minimum uncertainty of 3% is allowed (10%).

- The Monte Carlos used for the acceptance calculation do not include higher order radiative corrections. To evaluate the likely error in the acceptance calculation thus introduced, the difference between the acceptances calculated for the standard DIS selection (chapter 4) using the LEPTO Monte Carlo with and without the inclusion of radiative corrections using HERACLES is taken (7%).

- An overall uncertainty of 5% to account for the limited accuracy in the determination of the individual efficiencies of the sub–detectors used in the selection.

- The uncertainty due to the subtraction of photoproduction background is conservatively estimated to be equal to the full value of the correction applied ($< 1\%$).

- For the **FB**+$x_{I\!P}^{rec}$ selection, the overall normalisation is affected by the fraction of events in which the proton dissociates. Based upon studies using the RAPGAP Monte Carlo, including proton dissociation, such dissociation is

estimated to be present in $30 \pm 15\%$ [69], which is reflected in a 5% uncertainty in the overall normalisation of the structure function determined in this way. This is due to the limited sensitivity of the Forward Muon Detector and Plug calorimeter to proton dissociation. The $\eta_{\max} < 1.8$ selection is not sensitive to proton dissociation.

- The effect of "noise" in the detectors used in the **FB**+$x_{I\!P}^{rec}$ selection. The combination of electronic noise, remaining activity from previous bunch collisions, and synchrotron radiation produces spurious signals in the FMD and PLUG. The effect may be seen in figure 5.12c). While the efficiency for the $\eta_{\max}$ selection for diffractive events rises to 100% at low $x_{I\!P}$, the efficiency of all the selections using the PLUG and FMD never exceeds $\approx 90\%$ due to this effect. An uncertainty of 3% is estimated [69] for the correction due to these noise effects.

- The effect of the energy threshold used in the definition of $\eta_{\max}$ is estimated by taking the difference between the structure function obtained with the threshold set to 300 MeV and 500 MeV instead of the nominal value of 400 MeV (5%).

- The dependence of the bin corrections on the assumed structure function is estimated by taking the full difference between the corrections calculated with dependences on $\beta$ that are flat, or $\propto \beta(1-\beta)$. The effect is always less than 2%, and usually significantly so ($< 1\%$).

- The error introduced by the subtraction of background is estimated by the difference between the backgrounds obtained from the CDM and MEPS models, as discussed in section 5.2.1 (6%).

- The error in the acceptance calculation due to the assumed form of the $\beta$ dependence in the input Monte Carlo. This is calculated by re–weighting the $\beta$ dependence of the input Monte Carlo mixture with the function

$$f(\beta; g) = \left(\frac{1}{g} - g\right)\beta + g \tag{6.8}$$

to form two extreme distributions with $g$ set to 0.5 and 2 (the nominal distribution is obtained with $g = 1$.) These values are chosen such that the two extreme Monte Carlo samples formed are just compatible with the

data. The error is then calculated by taking half the difference between two calculated structure functions (5%).

- The error on the acceptance calculation due to the assumed dependence on $x_{I\!P}$ of the input structure function is estimated by re–weighting the input Monte Carlo with the function

$$f(x_{I\!P}) = x_{I\!P}^{\pm 0.2} \tag{6.9}$$

and taking half the difference between the two structure functions so calculated (6%).

- The efficiency of both diffractive selections depends upon the identity of the hard subprocess in the Monte Carlo, which leads to different characteristics for the hadronic final state. This model dependency is estimated by calculating the difference between the structure functions obtained assuming that all the events are either quark initiated or gluon initiated. Specifically, the error, $\Delta$, is defined

$$\Delta = \left| \frac{N_D^q}{N^q} - \frac{N_D^g}{N^g} \right| \cdot F_2 \tag{6.10}$$

where $N^q(N^g)$ are the number of quark(gluon) initiated Monte Carlo events reconstructed in each bin selected by the DIS criteria, and $N_D^q(N_D^g)$ are the number after the additional Diffractive selection. This calculation avoids, by construction, the uncertainty associated with different migrations arising from different structure function parameterisations, which are dealt with elsewhere (10%).

- The error on the luminosity is estimated to be 5%.

- Finally, the statistical errors of the Monte Carlo acceptance and efficiency calculations were considered. The statistics of the Monte Carlo data set were about 5 times larger than those of the data.

## 6.5 The Diffractive Contribution to the Proton Structure Function

The contribution of diffraction in the region $x_{I\!P} < 0.01$ to the proton structure function calculated using the $\eta_{\max} < 1.8$ selection is shown in figure 6.6 as a function of $x$ for four values of $Q^2$. In the region of overlap, good agreement is observed between the $\Sigma$ and electron reconstruction methods. The data are combined by taking the electron method for values of $y$ above 0.15, and the $\Sigma$ method below, which results in the smallest overall error. This combined evaluation of the $F_2^D(x,Q^2)\Big|_{x_{I\!P}\leq 0.01}$ is shown in table 6.2. Only the combined data are considered further.

| $Q^2$ | $x$ | y | $F_2$ | $\delta F_2^D(stat)$ | $\delta F_2^D(syst)$ | $\delta F_2^D$ |
|---|---|---|---|---|---|---|
| 8.5 | 0.000237 | 0.409 | 0.1386 | 0.0158 | 0.0196 | 0.0252 |
| 8.5 | 0.000422 | 0.230 | 0.1724 | 0.0177 | 0.0216 | 0.0280 |
| 12 | 0.000422 | 0.325 | 0.1288 | 0.0137 | 0.0174 | 0.0222 |
| 12 | 0.000750 | 0.183 | 0.1166 | 0.0119 | 0.0189 | 0.0223 |
| 12 | 0.00133 | 0.103 | 0.1211 | 0.0140 | 0.0126 | 0.0189 |
| 12 | 0.00237 | 0.058 | 0.0839 | 0.0119 | 0.0140 | 0.0184 |
| 12 | 0.00422 | 0.032 | 0.0510 | 0.0100 | 0.0186 | 0.0212 |
| 12 | 0.00750 | 0.018 | 0.0213 | 0.0047 | 0.0062 | 0.0078 |
| 25 | 0.000750 | 0.381 | 0.1441 | 0.0138 | 0.0165 | 0.0215 |
| 25 | 0.00133 | 0.214 | 0.0973 | 0.0107 | 0.0140 | 0.0177 |
| 25 | 0.00237 | 0.120 | 0.0845 | 0.0102 | 0.0138 | 0.0172 |
| 25 | 0.00422 | 0.068 | 0.0437 | 0.0069 | 0.0119 | 0.0138 |
| 25 | 0.00750 | 0.038 | 0.0069 | 0.0020 | 0.0013 | 0.0025 |
| 50 | 0.00133 | 0.428 | 0.1495 | 0.0263 | 0.0264 | 0.0373 |
| 50 | 0.00237 | 0.240 | 0.0973 | 0.0196 | 0.0230 | 0.0302 |
| 50 | 0.00422 | 0.135 | 0.0491 | 0.0124 | 0.0148 | 0.0193 |
| 50 | 0.00750 | 0.076 | 0.0056 | 0.0032 | 0.0019 | 0.0038 |

Table 6.2: *$F_2^D(x,Q^2)$ values of H1*

Figure 6.7 shows the good agreement between the structure functions obtained using the two different diffractive selections.

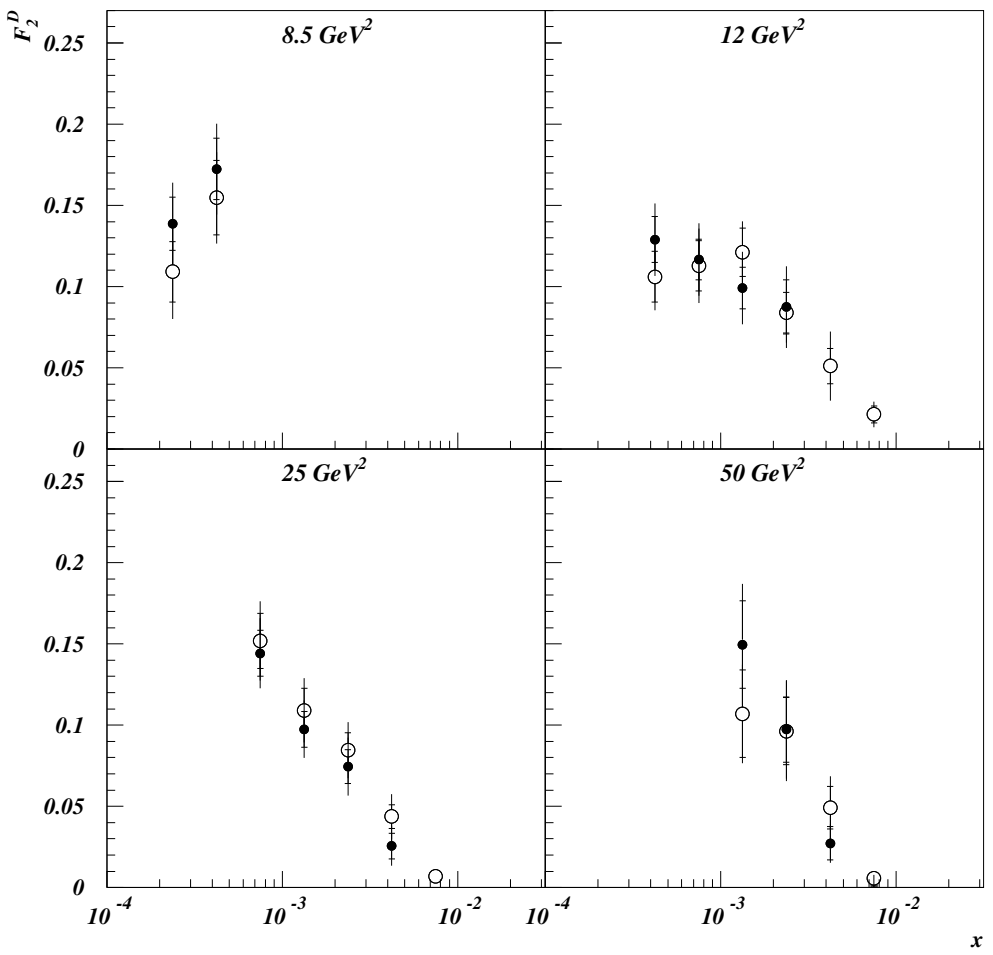


Figure 6.6: $F_2^D(x, Q^2)$ in four bins of $Q^2$; analysis with the $\eta_{\max}$ selection. The closed (open) circles show results from the electron ($\Sigma$) reconstruction method. An overall normalisation uncertainty of 5%, attributed to the luminosity measurement, is not included in the errors.

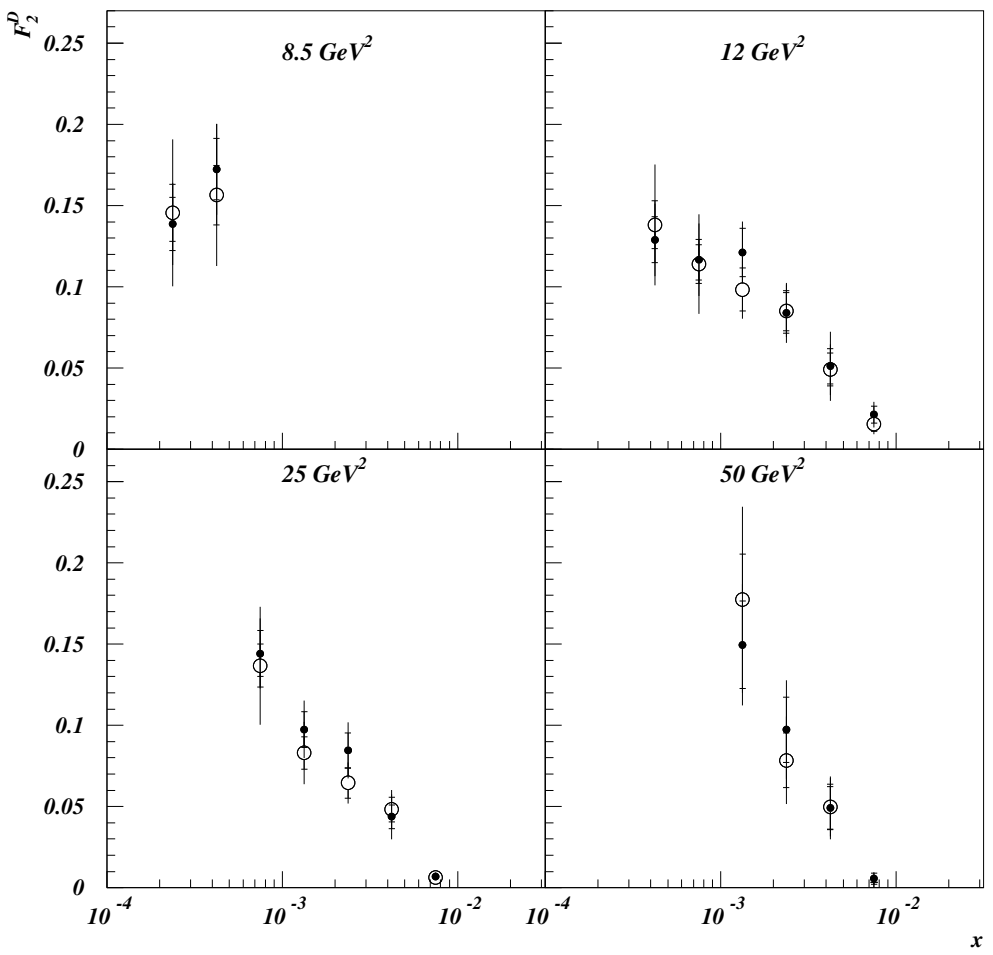


Figure 6.7: $F_2^D(x,Q^2)$ in four bins of $Q^2$; combined data from the $\eta_{\max}$ (close circles) and forward selection (open circles) analysis are compared. An overall normalisation uncertainty of 5% for the former and 8% for the latter is not included.

## 6.6 Discussion

The contribution to the proton structure function $F_2^D(x,Q^2)\Big|_{x_{I\!P}\leq 0.01}$ decreases monotonically to zero at $x = 0.01$ since diffraction with $x_{I\!P} < 0.01$ cannot contribute in the region $x > 0.01$. The $Q^2$ dependence of $F_2^D(x,Q^2)\Big|_{x_{I\!P}\leq 0.01}$ is shown in figure 6.8. Away from the kinematic limit at $x = 0.01$, there is no evidence for a variation of $F_2^D(x,Q^2)\Big|_{x_{I\!P}\leq 0.01}$ with $Q^2$: a good fit to the hypothesis of scale invariance, excluding the measurements at $x = 0.0075$, is obtained ($\frac{\chi^2}{d.f.} = \frac{10.3}{8}$, 24% C. L. assuming only statistical errors[3]). This is consistent with a mechanism that is partonic in origin.

Comparison with the inclusive proton structure $F_2(x,Q^2)$ indicates that this contribution rises to $\approx 10\%$ at $x = 2.4 \times 10^{-4}$.

The measurement of $F_2^D(x,Q^2)\Big|_{x_{I\!P}\leq 0.01}$ is compared with the theoretical predictions (see Chapter 2) of Capella et al. [71, 72] (CKMT), Donnachie and Landshoff [15, 27] (DL), Genovese, Nikolaev and Zakharov [28] (GNZ) in figure 6.9. Since all three predictions are for the single diffractive cross section, they are scaled up by a factor $\frac{1}{0.7}$ to account for the estimated level of 30% proton dissociation in the data.

All three models agree well in overall normalisation: although the data favour the prediction of Donnachie and Landshoff, the uncertainty in the level of proton dissociation does not allow any of the models to be excluded. The $(x,Q^2)$ dependence is also best reproduced by Donnachie and Landshoff; there is no evidence in the data for the scaling violations predicted by Capella et al. , and the very steep rise of $F_2^D(x,Q^2)\Big|_{x_{I\!P}\leq 0.01}$ with decreasing $x$ characteristic of the GNZ model is not preferred by the data.

[3] A similar fit, using statistical and systematic errors gives $\frac{\chi^2}{d.f.} = \frac{4.4}{8}$, 82% C. L.

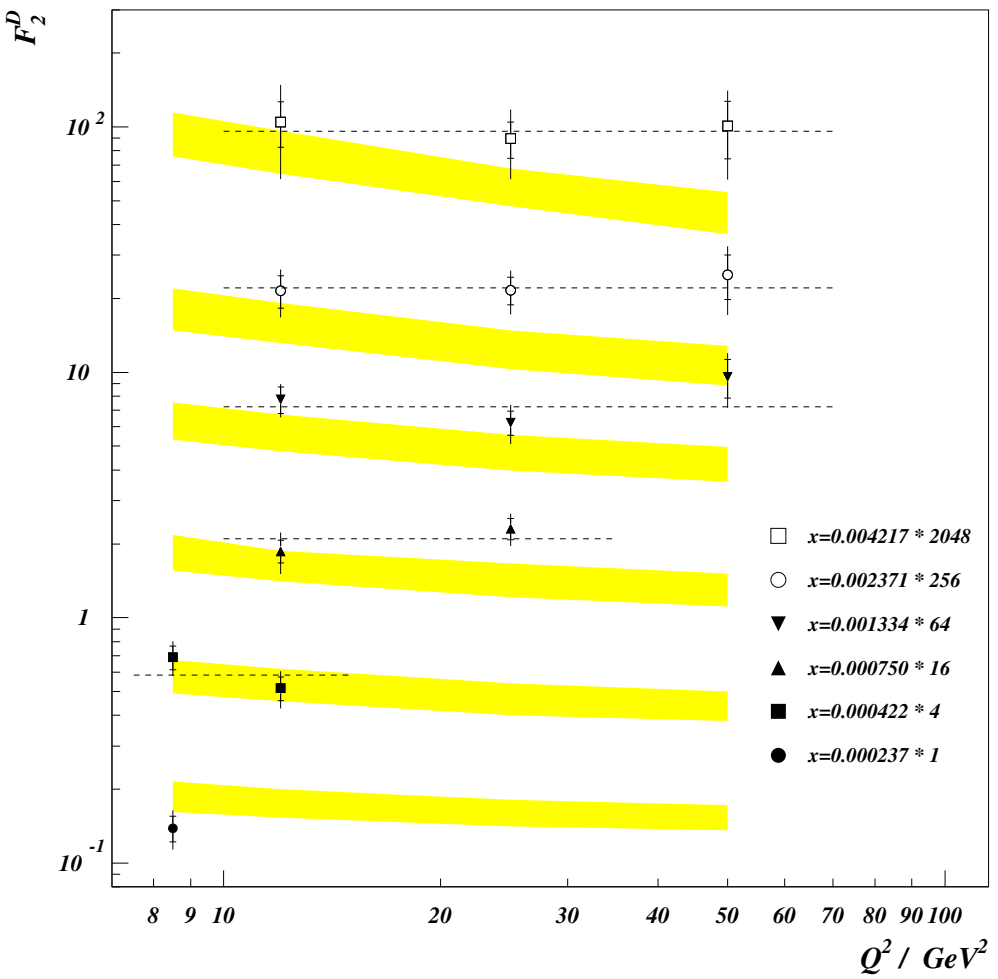


Figure 6.8: $F_2^D(x, Q^2)$ at fixed $x$ as a function of $Q^2$. The dashed lines show the result of a global fit, considering only statistical errors, assuming scale invariance for which the $\frac{\chi^2}{\text{d.f.}}$ is $\frac{10.3}{8}$. The shaded bands show the prediction of Capella et al. (see text).

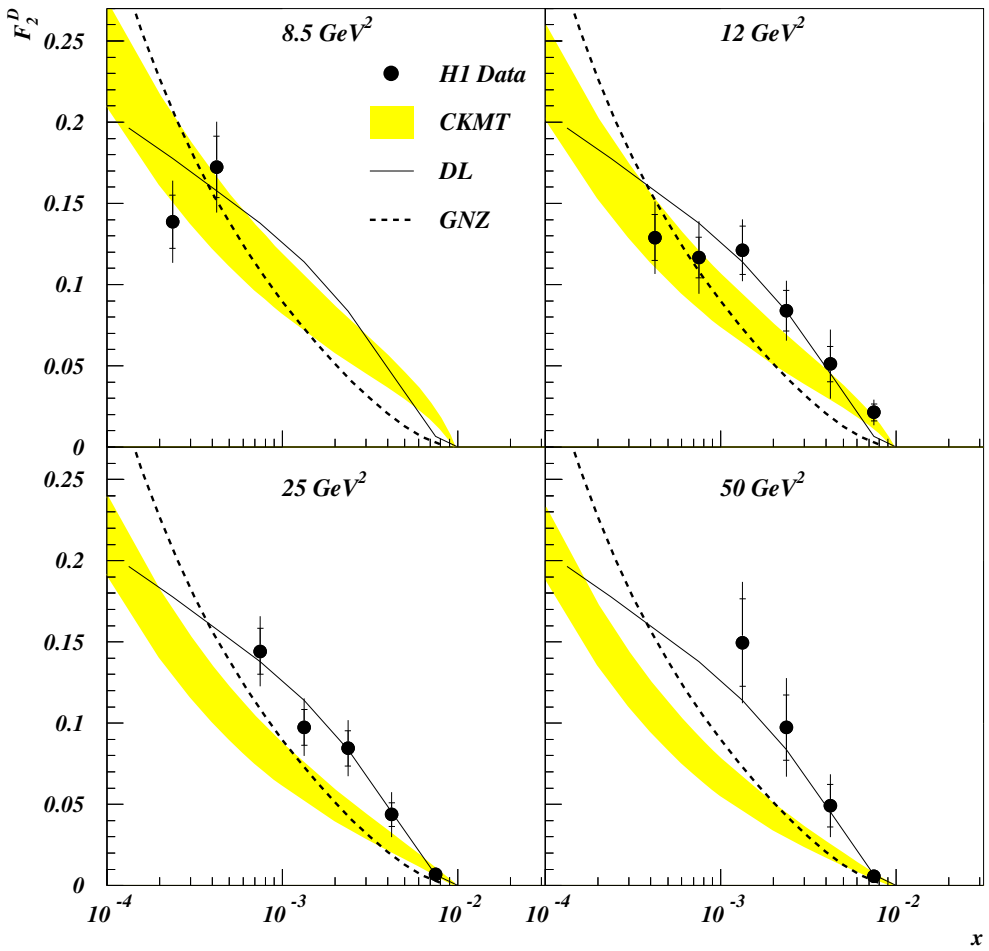


Figure 6.9: The $F_2^D(x,Q^2)\Big|_{x_{I\!P} \leq 0.01}$ values of H1 compared with the predictions of Capella et al. (CKMT), Donnachie and Landshoff (DL), and Genovese, Nikolaev and Zakharov.

## 6.7 Summary

Under the assumption that the Large Rapidity Gap events may be attributed to a diffractive component in the deep–inelastic scattering $ep$, the contribution of diffraction in the kinematic region $x_{I\!P} < 0.01$ to the inclusive proton structure function $F_2(x,Q^2)$ has been measured for the first time. This contribution exhibits no significant $Q^2$ dependence, which is consistent with a mechanism that is leading twist in QCD, and is partonic in origin. Since this contribution amounts to only $\approx 10\%$ of the proton structure function at the lowest $x$ where data exist, it cannot account for the steep rise observed in the proton structure function.

The data are well described in both overall normalisation, and $(x,Q^2)$ dependence, by the prediction of Donnachie and Landshoff, and are thus consistent with the exchange of the "soft" $I\!P$ found in high energy hadron–hadron interactions.

# Chapter 7

# The Diffractive Structure Function $\mathcal{F}_2^D(\beta, Q^2, x_{I\!P})$

## 7.1 Introduction

The analysis presented in this chapter seeks to extract the maximum information about the differential cross section for the Large Rapidity Gap events $\frac{d^4\sigma(ep\to epX)}{dx\,dQ^2\,dx_{I\!P}\,dt}$. As mentioned in the previous chapter, no meaningful determination of $t$ is currently possible. Therefore the most that may be extracted is

$$\frac{d^3\sigma(ep\to epX)}{dx\,dQ^2\,dx_{I\!P}} = \int \frac{d^4\sigma(ep\to epX)}{dx\,dQ^2\,dx_{I\!P}\,dt} dt \tag{7.1}$$

and so the full diffractive structure function $\mathbf{F_2^D}(x, Q^2, x_{I\!P}, t)$ may not be evaluated, but rather

$$\mathcal{F}_2^D(\beta, Q^2, x_{I\!P}) = \int \mathbf{F_2^D}(x, Q^2, x_{I\!P}, t)\, dt \tag{7.2}$$

where $\beta = \frac{x}{x_{I\!P}}$, such that $\mathcal{F}_2^D(\beta, Q^2, x_{I\!P})$ is related to the differential cross section as a function of $(x, Q^2, x_{I\!P})$ by

$$\frac{d^3\sigma(ep\to epX)}{dx\,dQ^2\,dx_{I\!P}} = \frac{2\pi\alpha^2}{xQ^4}\left[2(1-y)+y^2\right]\cdot\mathcal{F}_2^D(\beta, Q^2, x_{I\!P}) \tag{7.3}$$

## 7.2 The Determination of $\mathcal{F}_2^D(\beta, Q^2, x_{I\!P})$

In order to access as large a range in $x_{I\!P}$ as possible with an acceptable residual background from non–diffractive processes, the **FB** selection (section 5.4.3) is used. The structure function $\mathcal{F}_2^D(\beta, Q^2, x_{I\!P})$ is then determined from the resultant data in a similar manner to that used in the previous chapter: a bin–by–bin approach is adopted, and the same binning in $(x, Q^2)$ chosen, except that here the data are divided additionally in $\beta$.

### 7.2.1 Data and Bin Selection

Since $\beta$ is calculated from $M_X$ and $Q^2$, the reconstruction of which are specified in section 4.3, according to

$$\beta = \frac{Q^2}{Q^2 + M_X^2} \tag{7.4}$$

and the resolution in $Q^2$ is very good across the whole range considered, $7.5 < Q^2 < 70\,\mathrm{GeV}$, then the choice of the bin boundaries in $\beta$ is governed by the resolution in $M_X$. The systematic bias and resolution in the determination of $M_X$, calculated from the diffractive Monte Carlo, are shown in figures 7.1a) and 7.1b) respectively. For values of $M_X$ above 5 GeV, a small underestimate of $M_X$ of about 8% is seen, which may be attributable to very low momentum tracks with small radii of curvature which do not reach the calorimeter, and the inadequate response of the calorimeter at very low energies due to the aggressive noise suppression algorithm and the imperfect response of the energy re–weighting procedure [49]. As $M_X$ decreases below 5 GeV, a systematic overestimate of $M_X$ develops, associated with the fact that for very low values of $M_X$ small contributions from calorimeter noise may contribute greatly to $M_X$ if they are spatially distant from other energy depositions. The resolution of $M_X$ degrades from $\sim 20\%$ at $M_X = 25\,\mathrm{GeV}$ to above 100% for $M_X < 1\,\mathrm{GeV}$ due to the finite energy resolution of the calorimeter.

To reflect the accuracy with which $M_X$ may be reconstructed and the limited statistics in the data sample, four bins in $\beta$ were chosen with the boundary and centre values specified in table 7.1. The lower limit of $\beta > 0.065$ is introduced

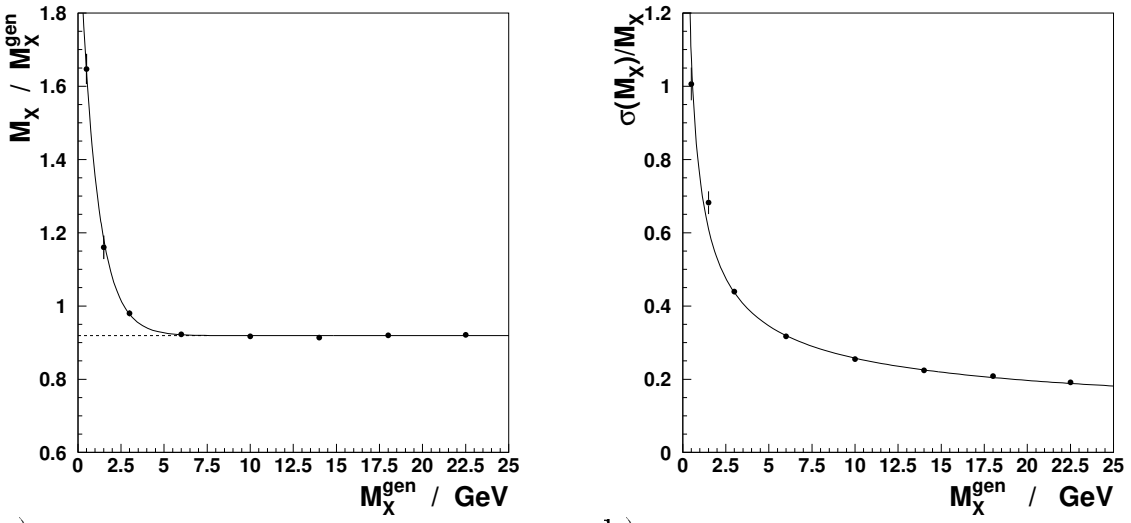


a) b)

Figure 7.1: The systematic bias (a) and resolution (b) of the reconstruction of $M_X$, calculated using diffractive Monte Carlo.

| $\beta_{centre}$ | $\beta_{low}$ | $\beta_{high}$ |
|---|---|---|
| 0.065 | 0.03 | 0.1 |
| 0.175 | 0.1 | 0.25 |
| 0.375 | 0.25 | 0.5 |
| 0.65 | 0.5 | 0.8 |

Table 7.1: The bins in $\beta$ used in the analysis

to exclude the region of very large masses, because the efficiency of the **FB** selection is very low for such low values of $\beta$ (figure 5.15). The upper limit of $\beta < 0.8$ is introduced to exclude the resonance region of light vector meson production where although the data are very well described by the Monte Carlo [64], and so the integrated cross section may be measured, the sharply peaked $M_X$ distribution precludes the reliable calculation of the bin corrections necessary for the extraction of a differential cross section or structure function. For the range in $Q^2$ adopted, diffractive light vector meson production may only contribute in the region $\beta < 0.8$ through smearing, that is where the reconstructed value of $M_X$ is much larger than the true value. Such smearing effects may be corrected

for with the Monte Carlo[1].

The deviations from the true values of $\beta$ for each of these four bins are shown in figure 7.2. Also shown is the effect of correcting for the systematic bias in $M_X$

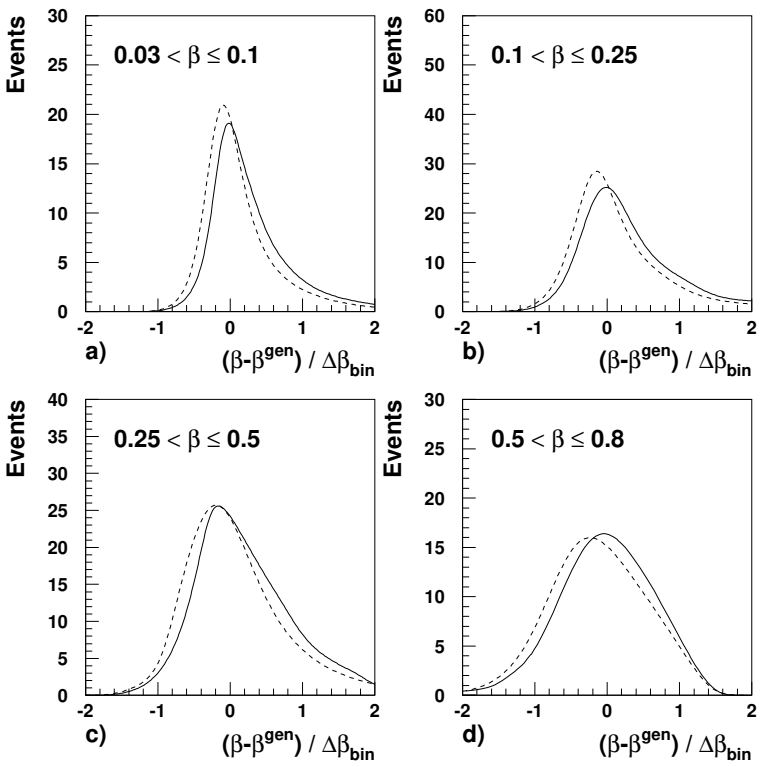


Figure 7.2: Deviations of the measured values of $\beta$ from the true values in units of bin width for the four chosen bins in $\beta$. Solid line: no rescaling of $M_X$, dashed line: constant rescaling (see text).

observed in figure 7.1a). No significant improvement in either the resolution or systematic shift are observed, indicating that limited resolution in $M_X$ dominates over the bias. The resolution in $\beta$ as a fraction of the bin width in $\beta$ is shown for the each of the four $Q^2$ bins used in the analysis in figure 7.3. The resolution becomes worse as $Q^2$ decreases, although the resolution remains significantly

[1]Note that this problem does not arise in the calculation of $F_2^D(x, Q^2)\big|_{x_{I\!P} \leq 0.01}$ in the previous chapter, as there the integration over $x \leq x_{I\!P} \leq 0.01$ amounts to an integration over $\beta$.

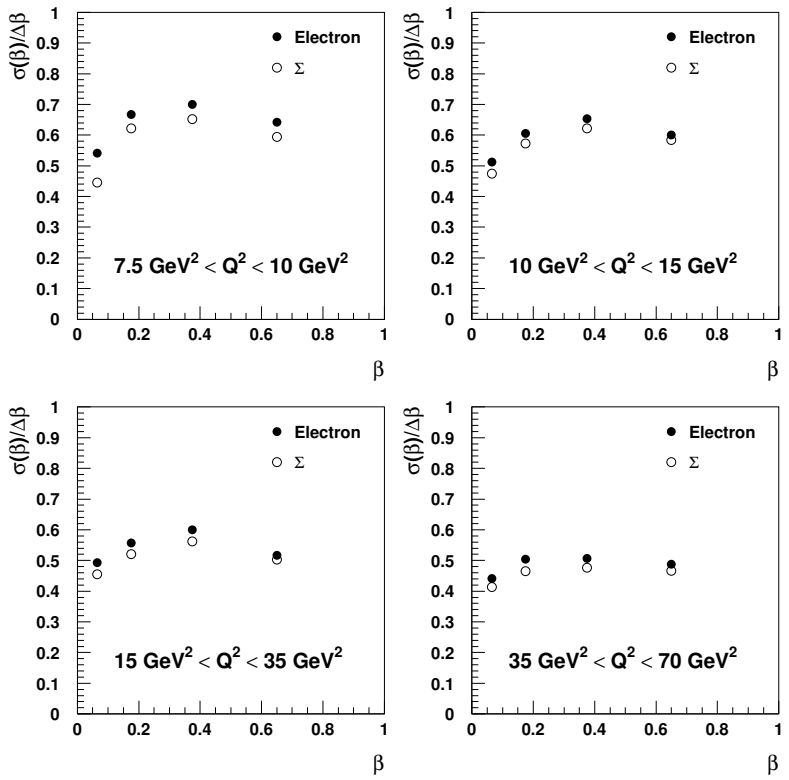


Figure 7.3: The resolution of the $\Sigma$ and electron reconstruction methods in $\beta$ for each of the $Q^2$ bins. The resolutions are averaged over the bins in $x$ used in the analysis, across which no significant variation is observed.

smaller than the bin size in the lowest $Q^2$ accessed.

With the **FB** selection, the analysis may be extended above 0.01 in $x_{I\!P}$, and diffractive data thus identified may have $x > 0.01$. The kinematic range accessible then becomes limited by the minimum $y$ that may be reached with adequate resolution. For the electron reconstruction method, this limit is $y > 0.05$, whilst for the $\Sigma$ method it is $y > 0.01$. However, because of a lower $y$ limit in the MEPS Monte Carlo, it is not possible to estimated the systematic uncertainty on the background from non–diffractive DIS below $y = 0.03$, and so this is the lower limit used with the $\Sigma$ method.

The resulting event samples obtained using the **FB** selection with the electron and $\Sigma$ reconstruction methods are shown in figure 7.4. Also shown are the $(x, Q^2)$ bins used.

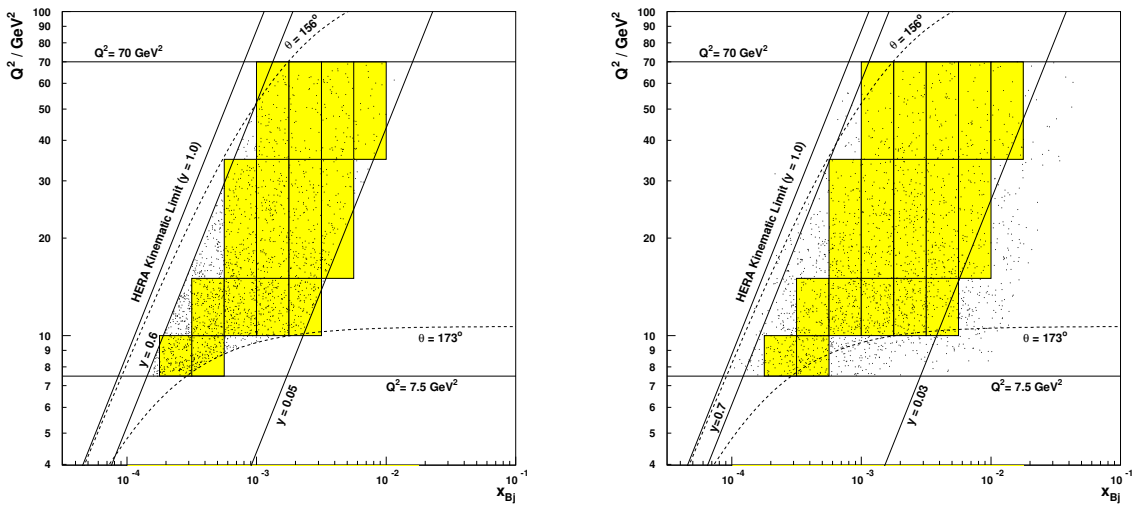


Figure 7.4: Selected Events and binning used for the electron (a) and $\Sigma$ (b) methods.

### 7.2.2 Systematic Uncertainties

The systematic errors considered are those discussed in section 6.4 in the previous chapter, and are calculated in an identical manner, and are summarised below as an average contribution to $\mathcal{F}_2^D(\beta, Q^2, x_{I\!P})$:

- radiative corrections: 8%;
- bin migration due to QED radiation: 8.1%;
- "standard DIS" background subtraction: 17%;
- uncertainties in the diffractive simulation for acceptance correction due to a priori ignorance of physics sub-processes: 10% ;
- 10% uncertainty in the LAr calorimeter hadronic energy scale: 11%;

- 1.7% uncertainty in the BEMC electromagnetic energy scale: 4%;
- 2 mrad uncertainty in electron scattering angle $\theta_e$: 3%;
- uncertainty in experimental acceptance due to a priori ignorance of $\mathrm{F}_2^D(\beta, Q^2, x)$: 8%.

## 7.3 The Diffractive Structure Function $\mathcal{F}_2^D(\beta, Q^2, x_{I\!P})$

The calculations of $\mathcal{F}_2^D(\beta, Q^2, x_{I\!P})$ using the electron and $\Sigma$ reconstruction methods are shown together in figure 7.5. In the regions of overlap, excellent agreement is observed between the two methods.

The data are combined, such that the overall error is minimised, by using the electron method data for $y$ greater than 0.25, and the $\Sigma$ method for $y$ less than this value. The data combined in this way are shown in figure 7.6 and in tables 7.2 and 7.3. Everywhere $\mathcal{F}_2^D(\beta, Q^2, x_{I\!P})$ is observed to decrease smoothly with increasing $x_{I\!P}$. To test the hypothesis of factorisation, the data are fitted with a universal dependence on $x_{I\!P}$ such that

$$\mathcal{F}_2^D(\beta, Q^2, x_{I\!P}) = a(\beta, Q^2) \cdot \frac{1}{x_{I\!P}^n} \tag{7.5}$$

An excellent fit to the data ($\chi^2 = 37.48/45$, C. L. 78%) is obtained with $n = 1.18 \pm 0.06(stat.) \pm 0.12(syst.)$ [2] including only statistical errors. A fit including statistical and systematic errors yields $\chi^2 = 17.9/45$ (C. L. 99.9%), with the same central value.

[2] As a consistency check, the fitting procedure is repeated using the electron data alone giving $n = 1.12 \pm 0.06$(stat.) $\pm$ 0.13(syst.) and with the $\Sigma$ data alone giving $n = 1.30 \pm 0.08$(stat.) $\pm$ 0.20(syst.), in good agreement.

| $Q^2$ | $\beta$ | $x_{I\!P}$ | $F_2^D$ | $\delta F_2^D(stat)$ | $\delta F_2^D(sys)$ | $N$ | $F_{back}$ | $Acc$ | $\delta$ |
|---|---|---|---|---|---|---|---|---|---|
| 8.5 | .065 | .00365 | 3.84 | 1.67 | 2.58 | 31 | .20 | .93 | .13 |
| 8.5 | .065 | .00649 | 4.49 | 1.59 | 2.35 | 23 | .31 | .76 | .42 |
| 8.5 | .175 | .00136 | 16.26 | 6.22 | 3.05 | 25 | .03 | .73 | .17 |
| 8.5 | .175 | .00241 | 15.40 | 4.73 | 3.61 | 21 | .13 | .85 | .35 |
| 8.5 | .375 | .00063 | 87.12 | 23.04 | 13.92 | 23 | .10 | .80 | .09 |
| 8.5 | .375 | .00112 | 58.86 | 14.81 | 15.76 | 27 | .02 | 1.01 | .34 |
| 8.5 | .650 | .00036 | 136.45 | 55.16 | 44.36 | 19 | .02 | .78 | .13 |
| 8.5 | .650 | .00065 | 61.07 | 23.27 | 23.79 | 17 | .01 | 1.11 | .52 |
| 12 | .065 | .00649 | 4.26 | 1.26 | 1.54 | 40 | .24 | .78 | .10 |
| 12 | .065 | .01154 | 3.28 | .84 | 1.93 | 34 | .36 | .63 | .14 |
| 12 | .065 | .02052 | .69 | .39 | .23 | 22 | .51 | .51 | .00 |
| 12 | .065 | .03648 | 1.07 | .35 | .42 | 18 | .23 | .29 | .00 |
| 12 | .175 | .00241 | 14.05 | 4.14 | 2.53 | 34 | .09 | .79 | .09 |
| 12 | .175 | .00429 | 7.42 | 1.88 | 2.72 | 27 | .24 | .93 | .11 |
| 12 | .175 | .00762 | 3.28 | 1.04 | 1.78 | 24 | .33 | .69 | .00 |
| 12 | .175 | .01355 | 2.31 | .69 | .53 | 29 | .40 | .65 | .00 |
| 12 | .175 | .02410 | .81 | .58 | .37 | 14 | .30 | .44 | .00 |
| 12 | .375 | .00112 | 35.71 | 9.37 | 5.91 | 24 | .02 | .97 | .12 |
| 12 | .375 | .00200 | 22.99 | 6.09 | 4.74 | 28 | .11 | .89 | .14 |
| 12 | .375 | .00356 | 9.98 | 2.60 | 1.61 | 19 | .08 | .66 | .00 |
| 12 | .375 | .00632 | 5.65 | 1.53 | .71 | 22 | .26 | .71 | .00 |
| 12 | .375 | .01125 | 3.53 | 1.15 | .98 | 19 | .20 | .72 | .00 |
| 12 | .650 | .00065 | 50.83 | 17.77 | 13.89 | 27 | .01 | 1.08 | .00 |
| 12 | .650 | .00115 | 37.37 | 10.23 | 10.39 | 40 | .04 | 1.25 | .10 |
| 12 | .650 | .00205 | 21.77 | 5.51 | 8.37 | 21 | .05 | .86 | .00 |
| 12 | .650 | .00365 | 21.17 | 4.66 | 6.39 | 28 | .06 | .67 | .00 |
| 12 | .650 | .00649 | 4.37 | 1.88 | 1.62 | 9 | .11 | .77 | .00 |

Table 7.2: The Diffractive Structure Function $\mathcal{F}_2^D(\beta, Q^2, x_{I\!P})$ for $Q^2 = 8.5\,\mathrm{GeV}^2$ and $Q^2 = 12\,\mathrm{GeV}^2$. The systematic and statistical errors are detailed separately, and must be added in quadrature to give the total error. An overall normalisation uncertainty of 8% is not included (see text).

| $Q^2$ | $\beta$ | $x_{I\!P}$ | $F_2^D$ | $\delta F_2^D(stat)$ | $\delta F_2^D(sys)$ | $N$ | $F_{back}$ | $Acc$ | $\delta$ |
|---|---|---|---|---|---|---|---|---|---|
| 25 | .065 | .01154 | 2.19 | .74 | .71 | 32 | .38 | .67 | .08 |
| 25 | .065 | .02052 | .84 | .37 | .22 | 21 | .51 | .49 | .08 |
| 25 | .065 | .03648 | .61 | .25 | .26 | 20 | .13 | .36 | .00 |
| 25 | .065 | .06488 | .01 | .12 | .02 | 2 | .54 | .19 | .00 |
| 25 | .175 | .00429 | 11.53 | 2.42 | 3.08 | 32 | .19 | .80 | .07 |
| 25 | .175 | .00762 | 3.29 | .93 | .90 | 33 | .32 | .76 | .11 |
| 25 | .175 | .01355 | 2.22 | .56 | 1.07 | 36 | .25 | .76 | .00 |
| 25 | .175 | .02410 | 1.71 | .45 | .41 | 37 | .19 | .51 | .00 |
| 25 | .175 | .04285 | .64 | .37 | .18 | 11 | .24 | .31 | .00 |
| 25 | .375 | .00200 | 30.39 | 6.62 | 6.01 | 32 | .07 | .79 | -.01 |
| 25 | .375 | .00356 | 10.08 | 2.74 | 1.06 | 28 | .16 | .84 | -.01 |
| 25 | .375 | .00632 | 4.65 | 1.24 | .79 | 25 | .28 | .81 | .00 |
| 25 | .375 | .01125 | 3.06 | .75 | .66 | 34 | .27 | .84 | .00 |
| 25 | .375 | .02000 | 1.50 | .65 | .31 | 20 | .35 | .70 | .00 |
| 25 | .650 | .00115 | 42.19 | 10.24 | 10.66 | 36 | .05 | 1.24 | -.03 |
| 25 | .650 | .00205 | 27.64 | 6.53 | 6.59 | 30 | .05 | .98 | .16 |
| 25 | .650 | .00365 | 13.05 | 2.92 | 2.92 | 26 | .12 | .89 | .00 |
| 25 | .650 | .00649 | 6.57 | 1.56 | 1.99 | 27 | .20 | .94 | .00 |
| 25 | .650 | .01154 | 2.94 | 1.02 | .97 | 14 | .12 | .90 | .00 |
| 50 | .175 | .00762 | 5.74 | 2.27 | 2.32 | 18 | .11 | .79 | .04 |
| 50 | .175 | .01355 | 2.61 | 1.17 | 1.28 | 5 | .84 | .67 | .12 |
| 50 | .175 | .02410 | 1.46 | .77 | .40 | 12 | .49 | .52 | .00 |
| 50 | .175 | .04285 | .49 | .39 | .15 | 5 | .21 | .33 | .00 |
| 50 | .175 | .07620 | .07 | .36 | .17 | 1 | .54 | .14 | .00 |
| 50 | .375 | .00356 | 13.40 | 5.79 | 3.05 | 20 | .03 | .81 | -.10 |
| 50 | .375 | .00632 | 10.14 | 3.05 | 2.99 | 10 | .19 | .85 | .17 |
| 50 | .375 | .01125 | 4.54 | 1.42 | .92 | 16 | .20 | .87 | .00 |
| 50 | .375 | .02000 | 2.04 | .81 | .53 | 16 | .27 | .80 | .00 |
| 50 | .375 | .03556 | 1.38 | .91 | .73 | 10 | .16 | .34 | .00 |
| 50 | .650 | .00205 | 28.29 | 14.98 | 6.94 | 11 | .00 | .84 | .49 |
| 50 | .650 | .00365 | 14.96 | 5.74 | 3.34 | 13 | .05 | .82 | .22 |
| 50 | .650 | .00649 | 9.56 | 3.35 | 3.09 | 12 | .22 | .83 | .00 |
| 50 | .650 | .01154 | 2.59 | 1.37 | 1.14 | 7 | .46 | .84 | .00 |
| 50 | .650 | .02052 | 1.49 | .90 | .33 | 8 | .40 | .83 | .00 |

Table 7.3: The Diffractive Structure Function $\mathcal{F}_2^D(\beta, Q^2, x_{I\!P})$ for $Q^2 = 25\,\mathrm{GeV}^2$ and $Q^2 = 50\,\mathrm{GeV}^2$. The systematic and statistical errors are detailed separately, and must be added in quadrature to give the total error. An overall normalisation uncertainty of 8% is not included (see text).

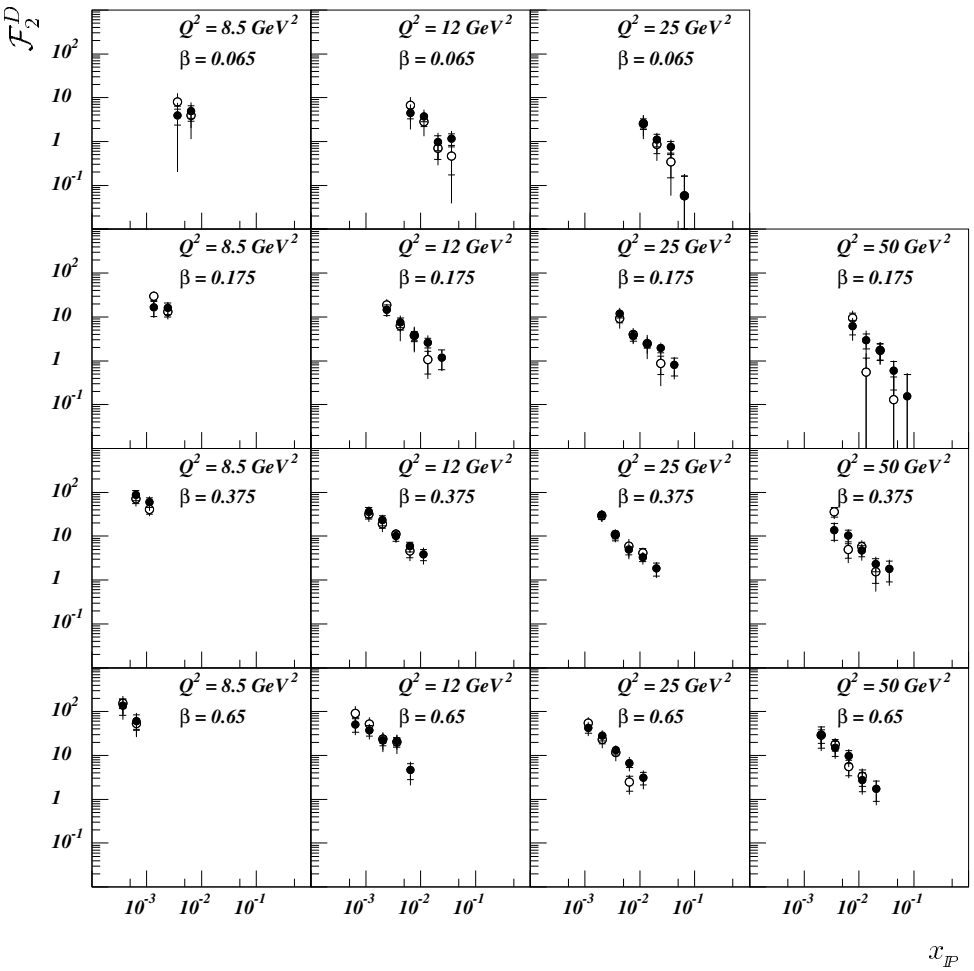


Figure 7.5: The diffractive contribution to the proton structure function $\mathcal{F}_2^D(\beta, Q^2, x_{I\!P})$ as a function of $x_{I\!P}$ for different values of $\beta$ and $Q^2$; the open (closed) circles represent the data from the electron ($\Sigma$) methods. Not included is an overall normalisation uncertainty of 8%.

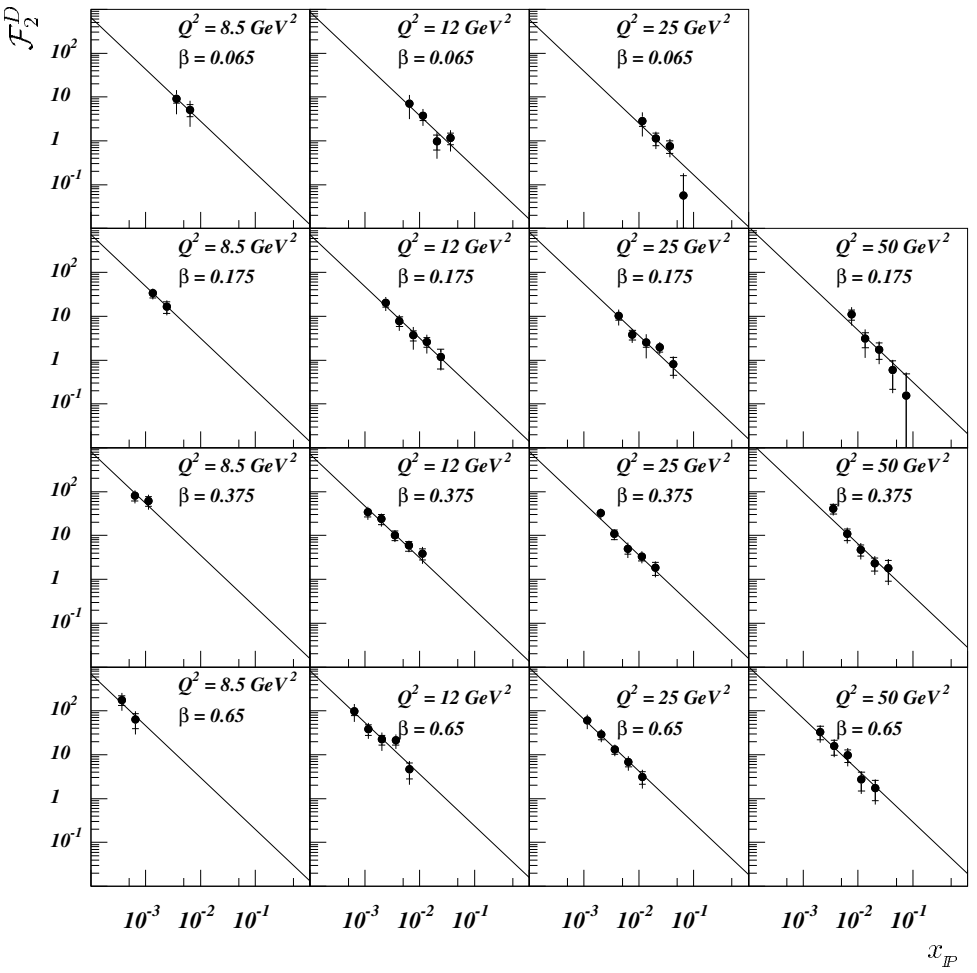


Figure 7.6: The diffractive contribution to the proton structure function $\mathcal{F}_2^D(\beta, Q^2, x_{I\!P})$ as a function of $x_{I\!P}$ for different values of $\beta$ and $Q^2$; the data from the electron and $\Sigma$ methods are combined as described in the text. Superimposed is the result of the fit establishing a factorisable dependence of the form $x_{I\!P}^{-n}$ (see text). Not included is an overall normalisation uncertainty of 8% (see text).

## 7.4 Discussion

The observed behaviour of $\mathcal{F}_2^D(\beta, Q^2, x_{I\!P})$ is expected naively if the mechanism responsible for the Large Rapidity Gap events involves deep–inelastic scattering off a colourless target carrying a fraction $x_{I\!P}$ of the proton's momentum, whose characteristics are independent of $x_{I\!P}$ and $t$. The cross section $\frac{d^3\sigma(ep\to epX)}{dx\,dQ^2\,dx_{I\!P}}$ then factorises into a universal term, $\propto x_{I\!P}^{-n}$, describing the flux of this target in the proton, and a further function, independent of $x_{I\!P}$ and $t$, that governs the deep–inelastic structure of this object. The electron scattering cross section for the process $ep \to eXp, N^*$ etc. can then be written

$$\frac{\mathrm{d}^3\sigma_{ep\to epX}}{\mathrm{d}\beta \mathrm{d}Q^2 dx_{I\!P}} = \frac{\mathrm{d}^2\sigma_{eT\to eX}}{\mathrm{d}\beta \mathrm{d}Q^2} \cdot f_{T/p}(x_{I\!P}) \tag{7.6}$$

where $\frac{\mathrm{d}^2\sigma_{eT\to eX}}{\mathrm{d}\beta \mathrm{d}Q^2}$ describes the deep–inelastic scattering of the electron off $T$.

If the colourless exchange is parameterised in terms of a Regge trajectory $\alpha(t)$, then the $x_{I\!P}$ dependence of this flux is expected to be $x_{I\!P}^{-(2\alpha(t)-1)}$. If the $t$ distribution of proton diffraction is here like that in soft $pp$ collisions, namely peripheral with a dependence $e^{bt}$ with $b > 1$, then the systematic error, which arises by ignoring any $t$ dependence of $\alpha(t)$ of size given by the slope $\alpha' = 0.25\,\mathrm{GeV}^{-2}$ of the $I\!P$ trajectory, is $< 4\%$. The observed universal dependence of $n = 1.18 \pm 0.06(stat.) \pm 0.12(syst.)$ is then consistent with a Regge trajectory of intercept $\alpha(0) = 1.09 \pm 0.03(\mathrm{stat.}) \pm 0.06(\mathrm{syst.})$, and so in excellent agreement with the leading trajectory which describes soft hadronic diffractive interactions, the pomeron, for which the trajectory is $\alpha(t) = \alpha(0) + 0.25t$ with $\alpha(0) = 1.085$ (section 2.9.5). Furthermore, this behaviour is inconsistent with both meson ($\rho, \omega$ *etc.*) exchange, for which a flat dependence on $x_{I\!P}$ is expected (corresponding to a Regge intercept $\alpha(0) = 0.5$), and also with pion exchange, any parameterisation of which leads inevitably to a rising dependence on $x_{I\!P}$ in the kinematic range of these measurements [73]. The Large Rapidity Gap events observed in low–$x$ deep–inelastic $ep$ scattering may therefore be identified unambiguously as predominantly diffractive in origin. The precision of the measurement does not exclude a contribution to deep–inelastic diffractive scattering from a "harder" BFKL motivated pomeron, associated with a component with a steeper dependence on $x_{I\!P}$, nor does it exclude small deviations from factorisation.

## 7.5 Summary

The measurement of the diffractive contribution to the proton structure function $\mathcal{F}_2^D(\beta, Q^2, x_{I\!P})$ identifies unambiguously the dominant mechanism for the production of rapidity gap events in deep–inelastic $ep$ collisions as diffractive, and entirely consistent with the exchange of a "soft" pomeron. To current experimental accuracy, no deviations from the simplest possible factorisable dependence on $x_{I\!P}$ are observed.

# Chapter 8

# The Pomeron Structure Function

## 8.1 Introduction

The observation of the simple factorisation in the measured structure function $\mathcal{F}_2^D(\beta, Q^2, x_{I\!P})$, independent of $\beta$ and $Q^2$, and the unambiguously diffractive nature of the dominant contribution to the large rapidity gap events lead naturally to the interpretation of the $\beta$ and $Q^2$ dependence of $\mathcal{F}_2^D(\beta, Q^2, x_{I\!P})$ as a measure of the deep–inelastic structure of diffraction.

## 8.2 The Determination of $\tilde{\mathcal{F}}_2^D(\beta, Q^2)$

The $\beta$ and $Q^2$ dependence of $\mathcal{F}_2^D(\beta, Q^2, x_{I\!P})$ may be extracted by unfolding the contribution from the measured $x_{I\!P}$ dependence over the range where data that are consistent with factorisation exist. Here, this is done by performing the integral

$$\tilde{\mathcal{F}}_2^D(\beta, Q^2) = \int_{x_{I\!P}^L}^{x_{I\!P}^H} \mathcal{F}_2^D(\beta, Q^2, x_{I\!P})\, dx_{I\!P} \tag{8.1}$$

where $x_{I\!P}^L = 3 \times 10^{-4}$ and $x_{I\!P}^H = 0.1$. The values of $\tilde{\mathcal{F}}_2^D(\beta, Q^2)$, along with the associated errors, are extracted from the data by fitting the measured $\mathcal{F}_2^D(\beta, Q^2, x_{I\!P})$ with

$$\mathcal{F}_2^D(\beta, Q^2, x_{I\!P}) = \frac{(n-1)\, \tilde{\mathcal{F}}_2^D(\beta, Q^2)}{\left\{ \frac{1}{x_{I\!P_L}^{n-1}} - \frac{1}{x_{I\!P_H}^{n-1}} \right\}} \cdot \frac{1}{x_{I\!P}^n} \tag{8.2}$$

where $n$ is the measured exponent, $n = 1.18 \pm 0.06(stat.) \pm 0.12(syst.)$, of the dependence on $x_{I\!P}$ of $x_{I\!P}^{-n}$. Under the factorisation hypothesis, where the diffractive structure function may be decomposed (equation 8.3) into a flux factor and a structure function for the pomeron

$$\mathbf{F_2^D}(x, Q^2, x_{I\!P}, t) = f_{\frac{I\!P}{p}}(x_{I\!P}, t) \cdot F_2^{I\!P}(\beta, Q^2) \tag{8.3}$$

then $\tilde{\mathcal{F}}_2^D(\beta, Q^2)$ differs from the pomeron structure function $F_2^{I\!P}$ only in overall normalisation. Since the precise value of this normalisation parameter depends on the choice of flux factor (section 2.9.5), the calculation is done in this experimentally motivated manner.

## 8.3 The Deep–Inelastic Structure of the Pomeron

The result of the fit of $\tilde{\mathcal{F}}_2^D(\beta, Q^2)$ to the data are shown in figure 8.1, in which the errors introduced by the uncertainty in the determination of the exponent $n$ are included, as a function of $Q^2$ for fixed $\beta$ (figure 8.1a)) and as a function of $\beta$ for fixed $Q^2$ (figure 8.1b)). The results are presented numerically in table 8.1.

There is no evidence for any significant $Q^2$ dependence of $\tilde{\mathcal{F}}_2^D(\beta, Q^2)$ (or equivalently of $\mathcal{F}_2^D(\beta, Q^2, x_{I\!P})$). That the diffractive component of the deep–inelastic $ep$ scattering exhibits approximate scale invariance is consistent with a partonic interpretation of the interaction mechanism. A fit to the hypothesis of a linear $\log_{10} Q^2$ dependence admits the possibility of scaling violations of $\sim \pm 0.3(\log_{10} \mathrm{GeV}^2)^{-1}$ for $\sim 1.5\sigma$. Furthermore, the current accuracy of the measurement means that any scaling violations may be $\beta$ dependent, as observed in the structure function of an extended object like the proton (section 2.4.2), or independent of $\beta$ as for the structure function of a point-like field quantum, like the photon, endowed with structure by vacuum fluctuations.

In figure 8.1b) it may be seen that $\tilde{\mathcal{F}}_2^D(\beta, Q^2)$ has little dependence on $\beta$ over the measured range ($0.065 \leq \beta \leq 0.65$). Therefore a substantial proportion of the diffractive interactions are inelastic, with $\beta \ll 1$. This $\beta$ dependence is in good agreement with a hard distribution $\propto \beta(1-\beta)$, consistent with the simplest $q\bar{q}$ interpretation of deep–inelastic diffraction. There is some evidence for an

additional component entering as $\beta \to 0$, which arises naturally in any partonic interpretation involving both quarks and gluons.

| $Q^2$ | $\beta$ | $\tilde{F}_2^{I\!P}$ | $\delta\tilde{F}_2^{I\!P}(stat)$ | $\delta\tilde{F}_2^{I\!P}(syst)$ |
|---|---|---|---|---|
| 8.5 | .065 | .152 | .037 | .078 |
| 8.5 | .175 | .174 | .044 | .028 |
| 8.5 | .375 | .339 | .064 | .066 |
| 8.5 | .650 | .238 | .066 | .074 |
| 12.0 | .065 | .274 | .040 | .102 |
| 12.0 | .175 | .259 | .032 | .055 |
| 12.0 | .375 | .286 | .034 | .029 |
| 12.0 | .650 | .255 | .036 | .040 |
| 25.0 | .065 | .184 | .039 | .093 |
| 25.0 | .175 | .318 | .035 | .089 |
| 25.0 | .375 | .310 | .034 | .061 |
| 25.0 | .650 | .343 | .037 | .048 |
| 50.0 | .175 | .340 | .074 | .150 |
| 50.0 | .375 | .460 | .072 | .119 |
| 50.0 | .650 | .371 | .072 | .093 |

Table 8.1: The pomeron structure function $\tilde{\mathcal{F}}_2^D(\beta, Q^2)$. The statistical and systematic errors combined in quadrature yield the overall error. Not included is an overall normalisation uncertainty of 8% (see text).

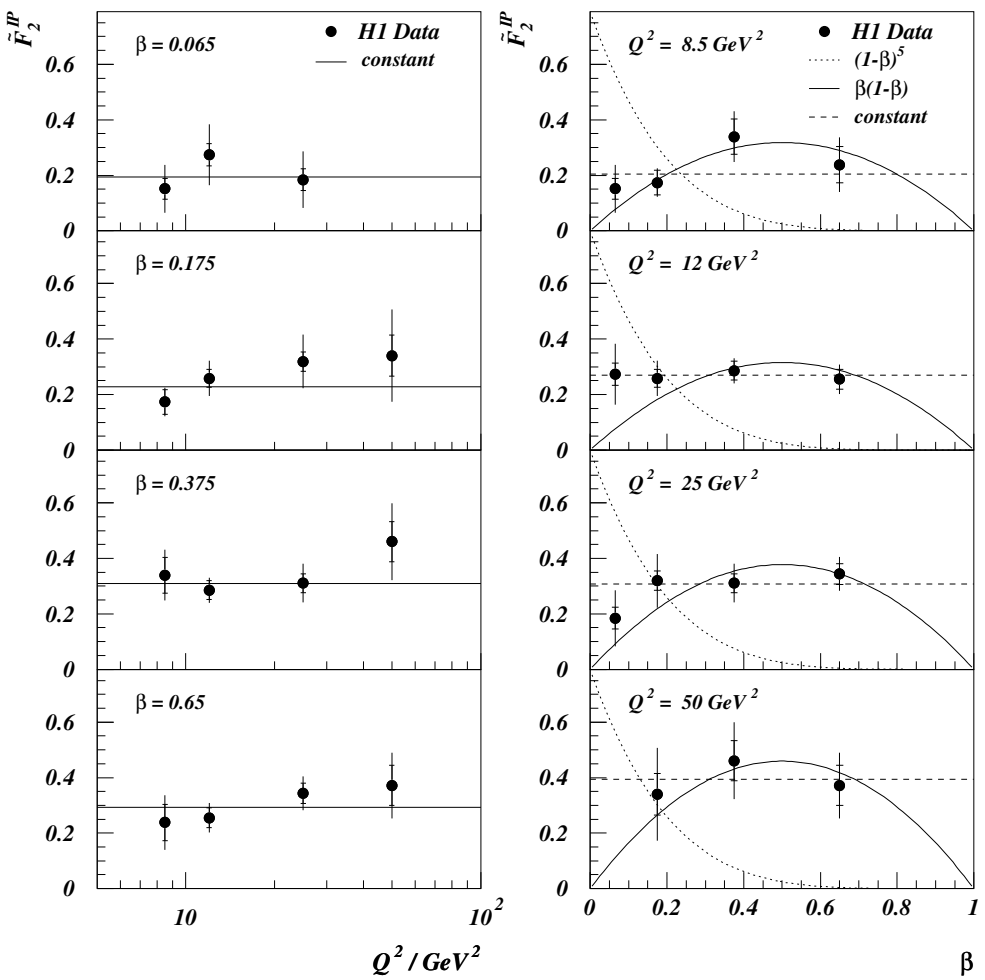


Figure 8.1: The structure function of the pomeron, $\tilde{\mathcal{F}}_2^D(\beta, Q^2)$. Left: as a function of $Q^2$ for different values of $\beta$, including a fit to all data points assuming scale invariance (see text). Right: as a function of $\beta$ for different values of $Q^2$, including a fit of a constant dependence on $\beta$ (dotted line) and of a $\beta(1-\beta)$ distribution (solid line). Also shown is a soft distribution ($\propto (1-\beta)^5$) with arbitrary normalisation.

## 8.4 Summary

A measurement of the deep–inelastic structure of diffraction, related to the structure function of the pomeron by a single normalisation factor, has been made for the first time. The dependence on $Q^2$ is broadly scale invariant for all values of the appropriate scaling variable, $\beta$. Both hard and soft components are seen in the $\beta$ dependence, such that a substantial proportion of the collisions are inelastic with $\beta \ll 1$. The characteristics of the pomeron are, therefore, likely to be attributable to partons.

# Chapter 9

# The Total Contribution of Diffraction to the Proton Structure Function

## 9.1 Introduction

The measurement of $\mathcal{F}_2^D(\beta, Q^2, x_{I\!P})$ presented earlier in this thesis can be transformed into a measurement of the contribution of diffraction to the proton structure $F_2(x, Q^2)$. This involves the integration of $\mathcal{F}_2^D(\beta, Q^2, x_{I\!P})$ over the range in $\beta$, or equivalently the range in $x_{I\!P}$, kinematically accessible at a particular $(x, Q^2)$.

It is commonly assumed that diffraction will no longer remain the dominant mechanism for the production of rapidity gap events for values of $x_{I\!P}$ greater than between 0.05 or 0.1 [14, 13]. As $x_{I\!P}$ increases, then the contribution from pion (and other meson) exchanges increases relative to that from pomeron exchange. Furthermore, the parameterisation, within the formalism of Regge theory, of the cross section for the production of final states with a rapidity gap (which *defines* the concept of the pomeron) assumes that $x_{I\!P}$ is small, typically $x_{I\!P} \lesssim 0.1$.

In addition, none of the diffractive selections studied here allow useful data to be extracted in this region. In this chapter an attempt is made to make the best estimate of the total contribution of diffraction to the proton structure function that is possible with the available data. This is done by evaluating the integral

of $\mathcal{F}_2^D(\beta, Q^2, x_{I\!P})$ over the range $x < x_{I\!P} < 0.1$.

The assumptions necessary about the $\beta$ and $x_{I\!P}$ dependence of the structure function $\mathbf{F_2^D}(x, Q^2, x_{I\!P}, t)$ are discussed, and the likely effects of the limitation that $x_{I\!P} < 0.1$ reviewed. It is shown that for values of $x$ below $x \sim 10^{-2}$, these effects are small enough such that conclusions may be made about the total contribution from diffraction in this region.

## 9.2 The Calculation of $F_2^D(x, Q^2)\Big|_{x_{I\!P} \leq 0.1}$

Many of the details of this calculation follow those of the previous chapter for the calculation of $\mathcal{F}_2^D(\beta, Q^2, x_{I\!P})$. The same selection and binning in $(x, Q^2)$ are adopted, and the measured cross section transformed into a structure function in the same manner. As radiative corrections were not available for the chosen binning, only results obtained with the $\Sigma$ reconstruction method are presented. The systematic uncertainties are treated in exactly the same manner as in chapters 6, 7 and 8. The consequence of the treatment of the systematic errors in this way is discussed below.

The calculation of $F_2^D(x, Q^2)\Big|_{x_{I\!P} \leq 0.1}$ requires an extrapolation of the $\beta$ dependence outside the region in which $\mathcal{F}_2^D(\beta, Q^2, x_{I\!P})$ has been measured, $0.065 < \beta < 0.65$. The extrapolation into the region $\beta >$ greater than 0.65 is not problematic: the inclusive properties of the light vector meson resonances are well described by the diffractive Monte Carlo. Rather, it is the extrapolation to values of $\beta$ lower than 0.065 that requires the most careful consideration. Since $x = \beta \cdot x_{I\!P}$, the extension of the analysis to higher values of $x_{I\!P}$ introduces a greater contribution from lower values of $\beta$ at fixed $x$. This effect is maximal for the lowest values of $x$ accessed as here the lowest values of $\beta$ are accessed.

In chapter 5 it is shown that, providing the density of gluons in the pomeron is no softer than that in the proton[1], that is the gluon density is not significantly

[1]There is strong theoretical justification for this in that the small momentum fraction of the proton taken by the pomeron is expected to result in a hardening of the parton density.

softer than

$$x f_g(x_{\frac{g}{\mathbb{P}}}) \propto (1 - x_{\frac{g}{\mathbb{P}}})^5 \tag{9.1}$$

then the magnitude of such a soft component is constrained by the data (figures 5.15 and 5.16)[2]. The systematic uncertainty in the acceptance that results from considering the difference between a pomeron composed entirely of quarks with density $\propto \beta(1-\beta)$ and one which in addition contains a gluon component $\propto (1 - x_{\frac{g}{\mathbb{P}}})^5$ is exceeded by the variations in the structure function considered in the evaluation of the systematic uncertainties as described in section 6.4.

## 9.3 The Diffractive Contribution to the Proton Structure Function

The structure function $F_2^D(x, Q^2)$ in the region $x_{\mathbb{P}} \leq 0.1$ is shown in figure 9.1. The largest systematic uncertainty is observed at the lowest values of $x$, as expected from the discussion above. This diffractive structure function is compared to that of the proton in figure 9.2. On the left hand side the two structure functions are shown together, with a logarithmic vertical scale to facilitate comparison. On the right, the ratio of the two structure functions are shown. An extrapolation of the measured dependency on $x_{\mathbb{P}}$ above 0.1 predicts that this measured diffractive structure function amounts to $> 98\%$ of the total. Thus, this ratio amounts to the fraction of the proton structure function, $F_2(x, Q^2)$, attributable to diffraction.

[2]The argument also holds for quarks. Since gluons from the pomeron may only couple to the virtual photon through a $q\bar{q}$ pair such that $\beta < x_{\frac{g}{\mathbb{P}}}$, while quarks may couple directly, then a quark component with a density softer $x f_q(x_{\frac{g}{\mathbb{P}}}) \propto (1 - x_{\frac{g}{\mathbb{P}}})^5$ is still constrained.

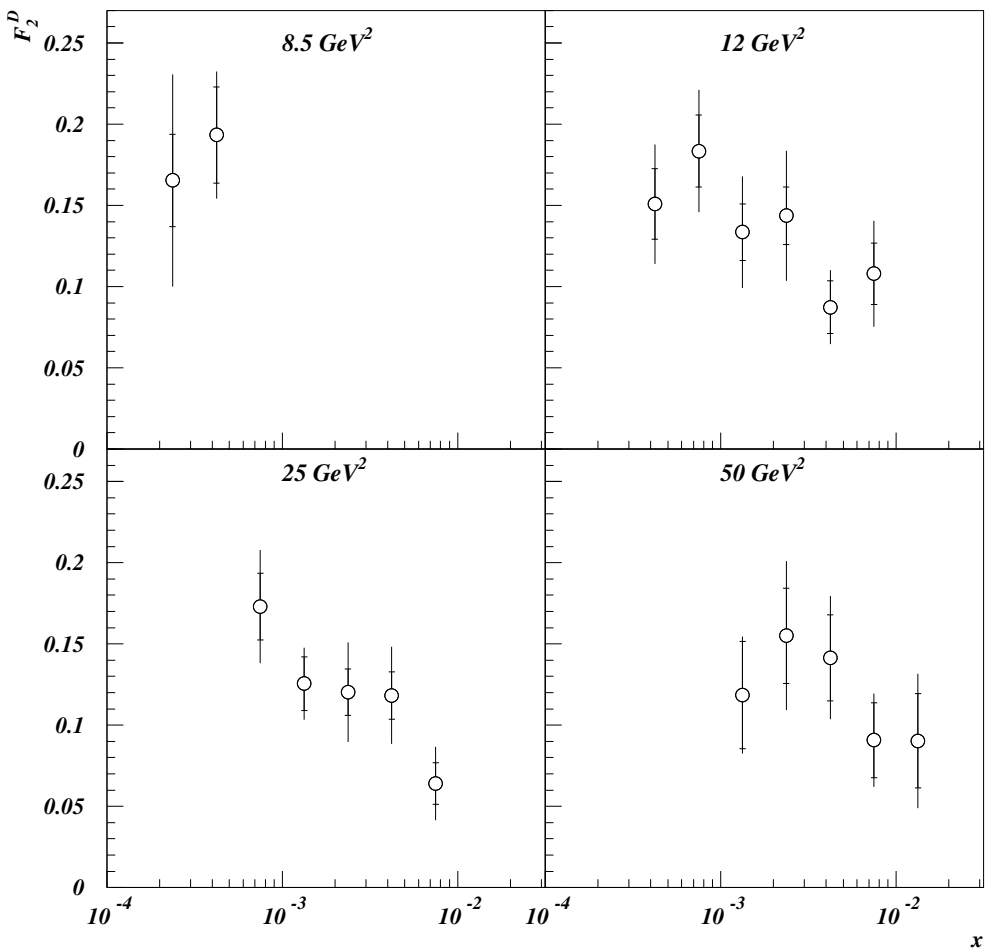


Figure 9.1: $F_2^D(x,Q^2)\Big|_{x_{I\!P}\leq 0.1}$ at different $Q^2$ as a function of $x$. An overall normalisation uncertainty of 8% is not included in the errors.

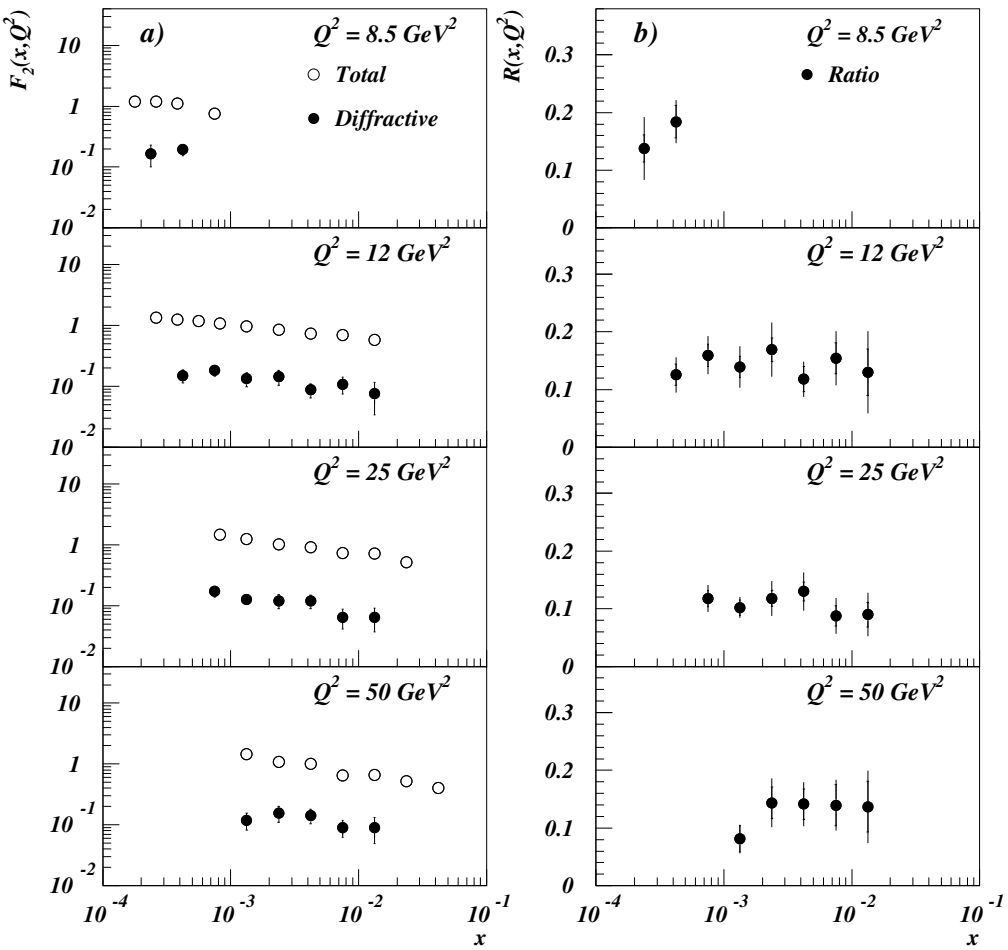


Figure 9.2: Left: The proton structure function (open circles) and the total contribution from diffraction to proton structure function (closed circles). Right: the fraction of the proton structure function attributable to diffractive processes.

## 9.4 Summary

Away from the kinematic limit, that is $x \ll 0.1$, there is no evidence that the total diffractive contribution evolves very differently in either $x$ or $Q^2$ from the proton structure function as a whole.

# Chapter 10

# Summary and Conclusions

It is demonstrated that the excess of events with a large rapidity gap may be attributed neither to conventional partonic models of deep–inelastic scattering, nor to unexpectedly high levels of background processes. A successful description of all of the observed properties of these events may be achieved by considering them to be the result of a diffractive contribution to deep–inelastic scattering.

With the assumption that these events are diffractive in nature, an interpretation in which the production of large rapidity gaps is a straightforward result of the exchange of a colourless component of the proton, the pomeron, then these events with a large rapidity gap may be used to calculate the cross section for diffractive deep–inelastic scattering. This cross section is calculated for the kinematic region $x_{I\!P} \leq 0.01$, where $x_{I\!P}$ is the fraction of the proton momentum carried by the putative colourless exchange, a region in which the kinematics ensure the production of a sufficiently large rapidity gap to facilitate the simple identification of these events. The cross section, expressed as a "diffractive contribution" to the proton structure function, $F_2^D(x,Q^2)\Big|_{x_{I\!P}\leq 0.01}$, constitutes no more than $\sim 10\%$ of the inclusive proton structure function $F_2$, such that these diffractive events may not, alone, account for the steep rise observed in $F_2$ as the Bjorken scaling variable, $x$, decreases. This contribution to the structure function is consistent with scale invariance.

Comparisons of $F_2^D(x,Q^2)\Big|_{x_{I\!P}\leq 0.01}$ with theoretical predictions demonstrate that the magnitude of this contribution is entirely consistent with expectations,

based on Regge phenomenology, derived from the observed characteristics of diffractive processes in high energy "soft" hadronic interactions.

The analysis is extended to search for rapidity gaps very close to the proton beam direction, such that the kinematic dependence of large rapidity gap production may be studied over as wide a range of the appropriate variables as possible. The diffractive contribution to the proton structure function is evaluated as a function of $x_{I\!P}$, $Q^2$ and $\beta$, the relevant scaling variable for deep–inelastic scattering on an object carrying a fraction $x_{I\!P}$ of the momentum of the proton. The dependence of $\mathcal{F}_2^D(\beta, Q^2, x_{I\!P})$ on $x_{I\!P}$ is found to be $x_{I\!P}^{-n}$ with $n = 1.18 \pm 0.06(stat.) \pm 0.12(syst.)$, independent of $Q^2$ and $\beta$, allowing decomposition into the product of cross sections describing the flux of a colourless component of the proton, and a cross section for the interaction of the colourless exchange with the electron.

In the framework of Regge theory, this behaviour on $x_{I\!P}$ may be interpreted as the result of a leading (dominant) Regge trajectory with intercept $\alpha(0) = 1.09 \pm 0.03(\text{stat.}) \pm 0.06(\text{syst.})$, in excellent agreement with the expectation from soft hadronic physics of $\alpha_{I\!P}(0) = 1.085$. Since this value is totally inconsistent with the intercepts expected from meson exchange ($\alpha(0) \sim 0.5$) or pion exchange ($\alpha(0) \sim 0$), the dominant mechanism for the production of these large rapidity gap events is, for the first time, identified unambiguously as diffractive. The nature and present precision of this measurement do not allow the possible contribution from a harder, BFKL motivated pomeron, with intercept $\alpha_{\text{BFKL}} \lesssim 1.5$, to be quantified.

By extracting the measured dependence on $x_{I\!P}$, the structure function of the colourless exchange, now unequivocally identified as the pomeron, may be measured for the first time. The deep–inelastic structure of the pomeron is observed to be consistent with scale invariance for all values of $\beta$, though the accuracy of the measurement admits the small logarithmic violations of scaling, symptomatic of QCD. Furthermore, the structure function of the pomeron is non–zero over a significant range in $\beta$, such that the substructure resolved carries only a fraction of the momentum of the pomeron, which, together with the observed scale invariance, is compelling evidence that this substructure is partonic in origin.

Finally, an estimate is made of the total contribution of diffraction to the pro-

ton structure function, $F_2$. This contribution is found to be broadly independent of both $x$ and $Q^2$, and to amount everywhere to about 13%.

# Appendix A

# Publication of this Analysis

The measurement of the "diffractive contribution" to the proton structure function $F_2^D(x,Q^2)\Big|_{x_{I\!P}\leq 0.01}$, presented in Chapter 6, appears in [6].

Together with the analysis of Mehta [69], the analysis of the diffractive structure function $\mathcal{F}_2^D(\beta,Q^2,x_{I\!P})$ presented in Chapters 7 and 8 developed into the published results of H1 [74]. This publication forms the remainder of this appendix.

# References


[1] J. D. Bjorken, Phys. Rev. **163** (1967) 1767.

[2] M. Breidenbach, J. I. Friedman, H. W. Kendall, E. D. Bloom, D. H. Coward, H. DeStaebler, J. Drees, L. W. Mo, and R. E. Taylor, Phys.Rev.Lett., 1969.

[3] Review of these data appear in Proc. of Conf. *6th International Symposium on Electron and Photon Interactions at High Energy*, pub. North Holland (1973): see C. Franzinetti on p. 353 for the electron–nucleon data, and E. Bloom on p. 227 for the neutrino–nucleon data.

[4] Y. L. Dokshitser, Sov. Phys. JETP **18**, (1977) 641;
V. N. Gribov, L. N. Lipatov, Sov. Journ. Nucl. Phys. **15** (1972) 438 and 675;
G. Altarelli, G. Parisi, Nucl.Phys. **B126** (1977) 298.

[5] E. A. Kuraev, L. N. Lipatov, and V. S. Fadin, Sov. Phys. JETP **45** (1977) 199
Ya. Balitsky and L. N. Lipatov, Sov. J. Nucl. Phys. **28** (1978) 822.

[6] H1 Collaboration, T. Ahmed et al., Nucl. Phys. **B439** (1993) 471.

[7] Zeus Collaboration, M. Derrick et al., Zeit. Phys. **C65** (1995) 379.

[8] T. Regge, Nuov. Cim. **14** (1959) 951, Nuov. Cim. **18** (1960) 947.

[9] G. Chew, S. Frautschi, S. Mandelstam, Phys. Rev. **126** (1962) 1202.

[10] J. D. Bjorken, Mini–School on "Diffraction at HERA", DESY (1994).

[11] J. Dainton, *Private Communication.*

[12] E. L. Berger et al. Nucl. Phys. **B286** (1987) 704.

[13] G. Ingelman, P. Schlein, Phys. Lett. **B152** (1985) 256.

[14] K. H. Streng, "Hard QCD Scatterings in Diffractive Reactions at HERA", in Proceedings of the HERA Workshop, p. 365, October 1987, ed. R. D. Pecci.

[15] A. Donnachie, P. V. Landshoff, Phys. Lett. **B191** (1987) 309.

[16] G. Ingelman, J .Bartels, Phys. Lett. **B235** (1990) 175.

[17] G. Ingelman and K. Janson–Prytz, "The Pomeron Structure Function and QCD at Small–$x$", in Proceedings of the Workshop "Physics at HERA", p. 233, October 1991, ed. W. Buchmueller and G. Ingelman;
G. Ingelman and K. Janson–Prytz, Phys. Lett. **B281** (1992) 325;
G. Ingelman and K. Janson–Prytz, Zeit. Phys. **C58** (1993) 285.

[18] For recent reviews see
G. Alberi, G. Goggi, Phys. Rep. **74** (1981) 1;
K. Goulianos, Phys. Rep. **101** (1983) 169.

[19] For a recent review, see P. V. Landshoff, *The Two Pomerons*, University of Cambridge Preprint, **HEP-PH-9410250**.

[20] L. N. Lipatov, Sov. Phys. JETP **63** (1986) 904, Zh. Eksp. Teor. Fiz. **90** (1986) 1536.

[21] R. Bonio et al., UA8 Collaboration, Phys. Lett. B211 (1988) 239.

[22] A. Brandt et al., UA8 Collaboration, Phys. Lett. B291 (1992) 417.

[23] H. Jung, *Private Communication.*

[24] F. E. Low, Phys. Rev. **D12** (1975) 163.

[25] S. Nussinov, Phys. Rev. Lett. **34** (1975) 1286, Phys. Rev. **D14** (1976) 246.

[26] P. V. Landshoff and O. Nachtmann, Zeit. Phys. **C35** (1987) 405.

[27] A. Donnachie, P. V. Landshoff, Phys. Lett. **B303** (1988) 634.

[28] M. Genovese, N. N. Nikolaev, B. G. Zakharov, "Diffractive DIS from the generalised BFKL pomeron. Predictions for HERA.", Institut für Kernphysik, KFA, Jülich preprint KFA–IKP(Th)–1994–37.

[29] G. Ingelman, *Partons and QCD Effects in the Pomeron*, DESY preprint, DESY 93–109, Hamburg (1993).

[30] J. J. Sakurai, Phys. Rev. Lett. **22** (1969) 981;
J. J. Sakurai and D. Schildknecht, Phys. Lett. **40B** (1972) 121;
For a review, see T. H. Bauer, R. D. Spital, D. R. Yennie, F. M. Pipkin, Rev. Mod. Phys. **50** (1978) 261.

[31] G. A. Schuler, H. Spiesberger, Proceedings of the HERA Workshop Vol.3 Hamburg, Oct 29–30, 1991 p.1419. ed. W. Buchmüller, G. Ingelman.

[32] A. Kwiatkowski, H. Spiesberger, H.-J. Möhring Proceedings of the HERA Workshop Vol.3 Hamburg, Oct 29–30, 1991 p.1294 ed. W. Buchmüller, G. Ingelman.

[33] G. Ingelman, Proceedings of the HERA Workshop Vol.3 Hamburg, Oct 29–30, 1991 p. 1366 ed. W. Buchmüller, G. Ingelman.

[34] L. Lönnblad, Comput. Phys. Commun. **71** (1992) 15.

[35] H1 Collaboration, I. Abt et al., Z. Phys. **C63** (1994) 377.

[36] H1 Collaboration, I. Abt et al., Z. Phys. **C61** (1994) 59.

[37] A. D. Martin, W. J. Stirling and R. G. Roberts, Phys. Lett. **B306** (1993) 145, ibid. **B309** (1993) 492.

[38] H1 Collaboration, I. Abt et al., Nucl. Phys. **B407** (1993) 515.

[39] Zeus Collaboration, M. Derrick et al., Phys. Lett. **B316** (1993) 412.

[40] H. Jung, Comp. Phys. Comm. **86** (1995) 147.

[41] N. H. Brook, A. De Roeck, A. T. Doyle, Proceedings of the HERA Workshop Vol.3 Hamburg, Oct 29–30, 1991 p. 1453 ed. W. Buchmüller, G. Ingelman.

[42] P. Bruni and G. Ingelman, "POMPYT", in Proc. of the Europhysics Conference, Marseilles, France, July 1993, ed. J. Carr and M. Perrottet, p.595, and unpublished program manual.

[43] H1 Calorimeter Group, NIM **A336** (1993) 460.

[44] V. Shekelyan *Simulation and Reconstruction in H1 Liquid Argon Calorimetry*, H1 note, DESY, Hamburg, H1–04/93–288 (1993).

[45] H. Wellisch, J. Kubenka, H. Oberlack, P. Schacht *Hadronic Calibration of the H1 LAr Calorimeter using Software Weighting Techniques* H1 note, DESY, Hamburg, H1–02/94–346 (1994).

[46] H1 Calorimeter Group, NIM **A336** (1993) 499.

[47] H1 Collaboration, *The H1 detector at HERA*, DESY preprint, DESY 93–103, Hamburg (1993).

[48] C. Brune, U. Hölzke, K. Meier, *BEMC Calibration 1993*, H1 note, DESY, Hamburg, H1–04/94–352 (1994).

[49] J. Phillips *A Comparison of Kinematic Fitting with Conventional Reconstruction Techniques*, H1 note, DESY, Hamburg, H1–09/93–314 (1993).

[50] T. Turča, *Private Communication.*

[51] The VMEbus specification, IEEE standard 1014.

[52] W. J. Haynes, *Bus-based architectures in the H1 data acquisition system*, VITA Int. Conf., *Open Bus Systems '92 in Research and Industry*, Zurich, Switzerland (1992), ISBN 90–72577–11–6 (1992) 27, Rutherford Appleton Laboratory report, RAL 92–048, (1992).

[53] J. Meyer (Ed.), *Guide to Simulation Program H1SIM*, H1 Internal Document, DESY, Hamburg (1991).

[54] F. Charles, J. F. Laporte, E. Perez, *Deep Inelastic Scattering low and medium $Q^2$ events selection for 1993 data* H1 note, DESY, Hamburg, H1–05/94–357 (1994).

[55] J. F. Laporte, DESY Silicon Graphics Dice2, ' laporte/run.lumi.info'.

[56] F. Jacquet, A. Blondel, *Proceedings of the Study of an ep Facility for Europe*, ed. U. Amaldi, DESY preprint, DESY 79–48, Hamburg (1979) 391.

[57] U. Bassler, G. Bernardi, *On the Kinematic Reconstruction of Deep Inelastic Scattering at HERA: the $\Sigma$ Method*, DESY preprint, DESY 94–231, Hamburg (1994).

[58] A. DeRoeck, M .Klein, T. Naumann, E. Peppel, U. Stoßlein, N. Wulff, *Analysis II of the 1992 Data of the Structure Function $F_2(x, Q^2)$*, H1 note, DESY, Hamburg, H1–12/93–332 (1993).

[59] G. Bernardi, Private Communication.

[60] F. Charles, S. Reinshagen, R. Roosen, P. Vanesch, *Photoproduction as background in Deep–Inelastic Scattering at low $x$*, H1 note, DESY, Hamburg, H1–9/94–380 (1994).

[61] S. Reinshagen, *The Backward Electromagnetic Calorimeter at H1, HERA, and Measurment of the Proton Structure Function*, Ph. D. Thesis (in German), University of Hamburg, *in litt.*.

[62] A. Panitch, *Vertex reconstruction and BPC efficiency determinations for the 1993 structure function analysis*, H1 note, DESY, Hamburg, H1–08/94–373 (1994).

[63] Zeus Collaboration, M. Derrick et al., Phys. Lett. **B 315** (1993) 481.

[64] H1 Collaboration, T. Ahmed et al., Nucl. Phys. **B 429** (1994) 477.

[65] T. Greenshaw, Private Communication.

[66] Pluto Collaboration, C. Berger et al., Z. Phys.**C 26** (1984) 353.

[67] F. Ferrarotto, Private Communication.

[68] P. Biddulph, Private Communication.

[69] A. Mehta, Ph. D. Thesis, University of Manchester (1994).

[70] H. Abramowicz, Private Communication.

[71] A. Capella, A. Kaidalov, C. Merino, J. Tran Thanh Van, *Structure Functions and Low $x$ Physics*, Laboratoire de Physique Théorique et Hautes Energies, Université de Paris Sud, **LPTHE Orsay 94-34** (1994).

[72] A. Capella, A. Kaidalov, C. Merino, J. Tran Thanh Van, *Diffractive Dissociation in Deep Inelastic Scattering at HERA*, Laboratoire de Physique Théorique et Hautes Energies, Université de Paris Sud, **LPTHE Orsay 94-42** (1994).

[73] G. Ingelman, Private Communication.

[74] H1 Collaboration, T. Ahmed et al., Phys. Lett. **B348** (1995) 681.

# Acknowledgements

I wish to thank all those who have helped me to produce this thesis.

My supervisor, Robin Marshall, I thank for much advice, and for allowing me the freedom I enjoyed pursuing this analysis.

I thank the many members of the Structure Functions working group, who provided vital technical support. In particular I thank Max Klein and Sebastian Reinshagen, without whose assistance the analysis may have been somewhat more straightforward, but probably quite wrong.

Those in the Diffractive working group offered continual support and encouragement. I am particularly indebted to John Dainton, Hannes Jung and Andrew Mehta for being outstanding physicists to work with.

Finally, I would like to thank my parents for all of their support during my time as a student in both Manchester and Hamburg.